NUMERICAL ANALYSIS OF GEOMATERIALS
Symposium dedicated to the memory of Prof. G.N. Pande
Assisi, Italy, 10-12 May, 2023

Numerical Analysis of Geomaterials
BOOK OF EXTENDED ABSTRACTS

Published by: NANGE Committee, Perugia, Italy
ISBN: 9791221033182

Organizers

Prof. S. Pietruszczak (Co-Chair)

McMaster University, Hamilton, Ontario, Canada

Prof. C. Tamagnini (Co-Chair)

University of Perugia, Italy

Conference Assistant

Kateryna Oliynyk
University of Perugia, Italy

Scientific Committee

J. Andrade (USA)
C. di Prisco (Italy)
I. Einav (Australia)
A. Gajo (Italy)
M. Hicks (Netherlands)
T. Hueckel (USA)
C. Jommi (Italy)
M. Karstunen (Sweden)
G. Meschke (Germany)
R. Michalowski (USA)
G. Milani (Italy)
M. Pastor (Spain)
W. Pula (Poland)
B. Schrefler (Italy)
H. Schweiger (Austria)
A.P.S. Selvadurai (Canada)
J.F. Shao (France)
A. Sulem (France)
J. Tejchman (Poland)
A. Truty (Poland)
C. Viggiani (France)
R. Wan (Canada)
J. Zhao (Hong Kong)

Table of Contents

1. Constitutive relations for geomaterials

2. Modelling of instabilities and localized deformation

3. Modelling of thermo-hydro-mechanical coupling and other transient problems

4. Discrete Element Method and its applications

5. Application of numerical techniques to practical problems

5.1 Embankments and dams

5.2. Piles and other foundations

5.3 Applications incorporating Material Point/Particle FE Method

5.4 Tunnels and other geotechnical structures

Preface

Over the last few decades, Computational Geomechanics has grown into a large discipline, encompassing both theoretical research on the formulation of balance laws and the governing constitutive equations, as well as the development of robust numerical methods that range from the classical Finite Element Method to more recent particle-based approaches. The scope of application of this research is broad and includes many areas of civil and environmental engineering, mining engineering, energy production, etc.

This symposium on *Numerical Analysis of Geomaterials* (NANGE) is dedicated to the memory of the late Dr. Gyan N. Pande, Professor of Civil Engineering at Swansea University (Wales, UK). Gyan made a lasting impact in the Computational Geomechanics community, not only through his numerous research achievements but also through his activities as the founding editor of the scientific journal *Computers and Geotechnics* and the co-organizer of a series of international symposia *Numerical Models in Geomechanics* (NUMOG) and *Computational Geomechanics* (ComGeo), which started in 1985 and covered a period of more than 30 years.

The NANGE symposium, organized in Assisi, follows the format of the 14 previous ComGeo and NUMOG international meetings. The event has a relatively limited number of participants and the focus is on preserving a high technical standard as well as an informal style.

This Book of Extended Abstracts of papers to be presented at NANGE contains 55 contributions, which are organized in five major sections:

1. *Constitutive relations for geomaterials*
2. *Modelling of instabilities and localized deformation*
3. *Modelling of thermo-hydro-mechanical coupling and other transient problems*
4. *Discrete Element Method and its applications*
5. *Application of numerical techniques to practical problems*

All abstracts included here will be archived in a downloadable form on the web site of the Symposium (http://www.nange.info) for wider dissemination.

We are grateful to the members of the Scientific Committee, for their co-operation and helpful suggestions.

S. Pietruszczak
C. Tamagnini

April 2023

1. Constitutive relations for geomaterials

A CONSTITUTIVE MODEL FOR LIGHTLY CEMENTED GRANULAR MATERIALS

C. Rossi, A. Tengattini , C. Viggiani and P. Besuelle
Univ. Grenoble Alpes, 3SR, F-38000 Grenoble, France

1. Introduction

Lightly cemented granular materials, both naturally occurring (e.g., sandstone) and artificial (e.g., grouted soil), are very common, yet there is a lack of mathematical models describing them in a consistent and unified manner.

In this work we develop a micro-mechanics inspired constitutive models for cemented granular materials whose internal variables have a clear physical interpretation. It builds on the work in [1] which is able to predict several aspects of the behaviours of bonded geomaterials (e.g. stress strain responses, localisation patterns) but does not predict dilation at low confinements.

2. Methodology and results

The model is developed, within the thermodynamics framework of Breakage Mechanics, by merging two constitutive models:

1. A thermomechanical constitutive model for cemented granular materials with quantifiable internal variables [2] (Fig 1a);
2. A constitutive modelling framework predicting critical state in sand undergoing crushing and dilation [1] (Fig 1b).

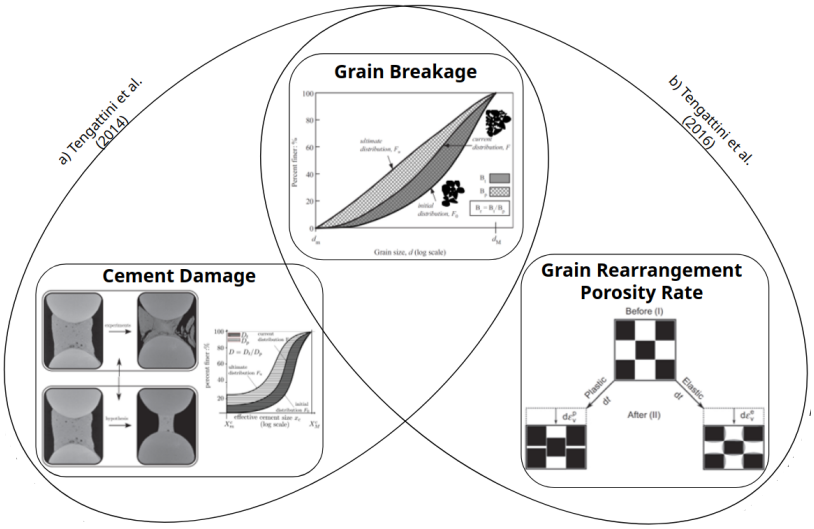

Figure 1. Outline of the origins of the model, focus on the three Micro-mechanisms of inelasticity

The model presented here requires a relative small number of constants (7) with a clear physical meaning. This family of models is based on the definition of the micro-mechanical processes governing the inelastic behaviour of the materials (schematised in Figure 1). Internal variables describing them are used in the formulation, cast within a thermo-mechanically sound framework from which the yield function and flow rules are derived.

The mechanical behaviour of these materials is controlled by the properties of the grains and their

(re)organisation, as with uncemented granular materials, plus the effect of cement, which, even in small quantities, can significantly alter the distribution of stresses within the grains and thus the mechanical response of the aggregate. The inelastic behaviour of this class of materials is therefore governed by three main processes: grain crushing, cement damage and fragment reorganisation.

Following the work in [3], the model is validated against the behaviour of a high porosity rock, Adamswiller sandstone ([4]). The constitutive model predictions under drained triaxial conditions are shown in Fig. 2. Stress–strain behavior is found to compare favorably with the experiments. In [3] the volumetric response at low pressures showed an unrealistic compaction, while, with this formulation, the model predicts a dilatant behaviour consistent with the experimental data.

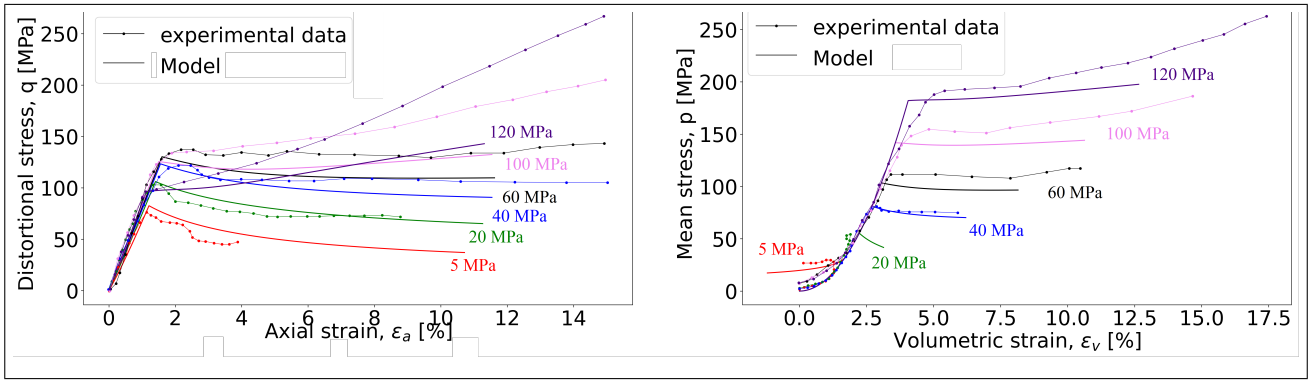

Figure 2. Drained triaxial compression tests on Adamswiller sandstone ([4]): experimental observation and model predictions.

3. Conclusions

The presented model builds on its predecessors. It improves their predictive capabilities, notably at low pressures, without losing performances elsewhere. This is without adding any mechanical parameters, thus maintaining its simplicity.

References

[1] Tengattini, A., Das, A., and Einav, I. (2016). A constitutive modelling framework predicting critical state in sand undergoing crushing and dilation. *Géotechnique*, **66**, 695–710.

[2] Tengattini, A., Das, A., Nguyen, G. D., Viggiani, G., Hall, S. A., and Einav, I. (2014). A thermomechanical constitutive model for cemented granular materials with quantifiable internal variables. part i—theory. *Journal of the Mechanics and Physics of Solids*, **70**, 281–296.

[3] Das, A., Tengattini, A., Nguyen, G. D., Viggiani, G., Hall, S. A., and Einav, I. (2014). A thermomechanical constitutive model for cemented granular materials with quantifiable internal variables. part ii–validation and localization analysis. *Journal of the Mechanics and Physics of Solids*, **70**, 382–405.

[4] Wong, T.-f. and Baud, P. (2012). The brittle-ductile transition in porous rock: A review. *Journal of Structural Geology*, **44**, 25–53.

A BOUNDING SURFACE VISCOPLASTIC MODEL FOR RATE-DEPENDENT BEHAVIOR OF SOILS INCLUDING PRIMARY AND TERTIARY CREEP

N. Khalili and B. Shahbodagh
School of Civil and Environmental Engineering, UNSW, Sydney, Australia

1. Introduction

The prediction of rate-dependent behavior of geomaterials, such as creep, stress relaxation, and strain rate dependency, is of great interest in geotechnical engineering. Creep and strain rate dependency is of particular concern in the analyses of the long-term settlement of infrastructures founded on soft soils, the stability of natural and excavated soil slopes, deformation and failure analysis of earth structures subject to cyclic and dynamic loading, construction of tunnels in squeezing ground, analysis of pavement structures, design of geological nuclear waste disposal facilities, and dynamic penetration and anchor installation problems to name a few.

2. Previous work

Many researchers have reported data for the rate/time dependent behavior of soils; e.g. see [1,2]. Leroueil et al. [2] showed that the time-dependent behavior of clays subjected to one-dimensional compression can be described by a unique stress–strain–strain rate relationship. This, known as the isotach approach, has extensively been used and validated for various clayey soils. In parallel with the experimental investigations, several approaches have been developed to capture the rate-dependent behavior of soils, including empirical models, rheological models, and elastic-viscoplastic constitutive models.

The elastic-viscoplastic models are the most comprehensive and widely adopted, and are typically developed based on either the overstress elastoplasticity theory or the theory of nonstationary flow surface. The overstress method is relatively straightforward but relies heavily on the accurate determination what is known as the overstress function which is often defined arbitrarily. The overstress approach differs from the classical plasticity theory in that it does not utilize the consistency condition to derive the hardening modulus. Strain hardening elastic-viscoplastic models developed based on the overstress theory are also unable to describe tertiary creep, unless an additional stress state dependent parameter is introduced with little or no physical meaning.

The deficiencies in the overstress models have been rectified in non-stationary type models that meet the consistency condition and can predict undrained tertiary creep in normally consolidated clays. However, the non-stationary models can only capture creep when the stress state lies on the yield surface, and therefore, they are not able to predict creep in over consolidated clays. In particular, there are currently no models of creep that can rigorously capture creep rupture in overconsolidated soils. This is of particular relevance to natural and excavated slopes where creep failure is most common. The creep-induced instability in slopes generally occurs at stress levels less than the peak strength, but above the critical state line. It develops as a result of the accumulation of plastic volumetric dilation with time, leading to gradual softening and reduction of the peak strength, and ultimately failure of the soil [3].

There are various techniques for capturing plasticity inside the yield surface: the two widely used theories are the theory of multi surface plasticity [4] and the theory of bounding surface plasticity [5]. In particular, the bounding surface plasticity theory has attracted great interest because of its simplicity and ease of use [6-10]. It is suitable for the analysis of soils subjected to complex loading paths and rectifies the inherent restriction in the conventional plasticity theory, that is, an abrupt change from elastic to elastoplastic behavior. Adopting a bounding surface plasticity framework, Kaliakin & Dafalias [6] developed an elasto-plastic–viscoplastic constitutive model for

time-dependent behavior of cohesive soils. However, their model was based on the overstress theory, and the constitutive relations were obtained by decomposing the inelastic strains into rate-dependent and rate-independent parts. This is questionable because only the combined effects of such plastic deformations might be measurable. In addition, in their model, the bounding surface acted as an upper bound on rate sensitivity, and beyond a certain limit on the strain rate, the predicted response became rate-independent. This is contradictory to the current experimental evidence [11] which clearly shows that soil behavior is strongly rate-dependent even at very high strain rates. The model was also unable to describe tertiary creep and consequently the creep failure of soils.

Following the theoretical approach proposed by Kaliakin & Dafalias [6], Liu & Ling [8] developed an elastoplastic–viscoplastic bounding surface model to simulate the time-dependent monotonic and cyclic behavior of geosynthetic reinforced soils. Higgins et al. [10] proposed a bounding surface viscoplasticity model based on the overstress theory but limited their analysis to sands under blast loading. Recently, Islam & Gnanendran [12] developed an overstress type of bounding surface model for the analysis of clayey soils. Similar to previous contributions, these models adopt arbitrary overstress functions and do not satisfy the consistency condition.

3. Proposed model

In this work, a rigorous viscoplastic constitutive model for the time-dependent behavior of soils is presented with particular reference to capturing drained and undrained behavior during primary and tertiary creep [13]. The model is formulated in the context of the viscoplastic framework and the bounding surface plasticity theory. It captures the accumulation of viscoplastic strains upon loading and unloading as well as creep rupture in normally and overconsolidated soils. Hardening and softening characteristics of the material are accounted for through the influence of viscoplastic volumetric strain as well as strain rate on the evolution of the bounding surface. Unlike the overstress models, the viscoplastic model meets the consistency condition and allows a smooth transition from rate-independent plasticity to rate-dependent viscoplasticity. A non-associated flow rule is defined to generalize the application of the model to a wide range of soils. The model requires a small number of material parameters determined using standard laboratory testing equipment. The model is validated through the comparison of the simulation results with experimental data from the literature highlighting the capabilities of the model.

4. References

[1] Šuklje, L. (1957). *Proc., 4th Int. Conf. on Soil Mech. and Foundation Engineering*, 200–206.
[2] Leroueil, S., Kabbaj, M., Tavenas, F. & Bouchard, R. (1985). Géotechnique **35**, 159–180.
[3] Hunter, G.J. & Khalili, N. (2000). *GeoEng 2000 Conf. Melbourne, Australia*.
[4] Mroz, Z. (1967). *J. Mech. Phys. Soids.* **15** (3): 163–175.
[5] Dafalias, Y. F. & Popov, E. P. (1975). *Acta Mech*.**21** (3), 173–192.
[6] Kaliakin, V. N. & Dafalias, Y.F. (1990). *Soils Found.* **30** (3): 11–24.
[7] Khalili, N., Habte, M.A. & Valliappan, S. (2005). *Int. J. Numer. Meth. Eng.* **63** (14): 1939–1960.
[8] Liu, H. & Ling, H.I. (2007). *J. Eng. Mech.* **133** (7): 801–815.
[9] Khalili, N., Habte, M.A. & Zargarbashi., S. (2008). *Comput. Geotech.* **35** (6): 872–889.
[10] Higgins, W., Chakraborty, T., & Basu, D. (2013). Int. J. Numer. Anal. Methods Geomech.**37** (15): 2590–2610.
[11] Whitman, R.V. (1970). *Report26.* Contract Rep. No. 3-26. Vicksburg, MS: U.S.Army Waterways Experiment Station, Corps of Engineers.
[12] Islam, M.N., & Gnanendran. C.T.. (2017). *J. Eng. Mech*. **143** (10):04017121.
[13] Shahbodagh, B., Thi, N.M., Esgandani, G.A. & Khalili, N. (2020). *Int. J. Geomech*. **20** (9): 04020143.

DATA-DRIVEN BREAKAGE MECHANICS

J. Ulloa, A. Gorgogianni, M. Ortiz, J.E. Andrade
California Institute of Technology, Pasadena, CA, USA

1. Introduction

Despite its importance, the crushing of granular media remained virtually untreated in continuum mechanics until the pioneering work of Einav [1], where a breakage internal variable was introduced in a constitutive model to track the evolution of grain-size distribution (GSD). This model has become well-established in the literature, where complex mechanisms, including plasticity, have been incorporated through phenomenological functions and parameters. The drawbacks of this modeling philosophy, shared by constitutive models in general, are the epistemic uncertainty and the limited physical meaning of the material functions and parameters. On the other hand, grain-scale models, e.g., the breakage-extended level-set discrete element method (LS-DEM), do not rely on phenomenological assumptions and provide a direct representation of granular materials. However, these models imply a high computational cost that scales with the number of particles.

These observations suggest the need for an efficient modeling framework with minimal phenomenology and, at the same time, the ability to describe complex material behavior. A paradigm shift in this context was set forth by Kirchdoerfer and Ortiz [2] through the concept of *data-driven mechanics*. This framework resolves the basic equations of continuum mechanics but relies on material behavior directly extracted from empirical data rather than from a constitutive model. Therefore, the method requires no phenomenological assumptions and allows us to employ and reuse material data from experiments and lower-scale simulations. In the present work, we extend these ideas to materials with evolving microstructures and develop a model-free data-driven framework for breakage mechanics. Numerical results indicate that the proposed methodology can capture the stress-strain response of crushable sand while accurately predicting the evolution of GSD. These results suggest that data-driven breakage mechanics provides a promising counterpart to continuum breakage mechanics [1], having the advantage of being parameter-free and presenting a notable accuracy furnished by the direct use of material data in the absence of constitutive functions.

2. Formulation

We consider a solid body discretized into N nodes and M material points and subjected to nodal forces $\boldsymbol{f} = \{\boldsymbol{f}_i \in \mathbb{R}^n\}_{i=1}^N$. The state of the system is given by the nodal displacements $\boldsymbol{u} = \{\boldsymbol{u}_i \in \mathbb{R}^n\}_{i=1}^N$ and the local stress-strain pairs $\mathbf{z}_e \coloneqq (\boldsymbol{\varepsilon}_e, \boldsymbol{\sigma}_e) \in \mathbb{R}^{2m}$. Assuming that the solid evolves in a finite number of time steps, the local states $\mathbf{z}_e^{k+1}$ at each material point e and time step $k+1$ are such that the collection $\mathbf{z}^{k+1} \coloneqq \{\mathbf{z}_e^{k+1}\}_{e=1}^M$ in the global phase-space $\mathrm{Z} = \mathbb{R}^{2m} \times \cdots \times \mathbb{R}^{2m}$ complies with the compatibility and equilibrium condition $\mathbf{z}^{k+1} \in \mathrm{E}^{k+1}$, where

$$\mathrm{E}^{k+1} \coloneqq \left\{ \mathbf{z} \in \mathrm{Z} \ : \ \boldsymbol{\varepsilon}_e^{k+1} = \mathbf{B}_e \boldsymbol{u}^{k+1} \ \forall e \in \{1, \dots, M\}, \quad \sum_{e=1}^{M} w_e \mathbf{B}_e^{\mathrm{T}} \boldsymbol{\sigma}_e^{k+1} = \boldsymbol{f}^{k+1} \right\}. \tag{1}$$

Conventional constitutive models find closure to this condition through functional stress-strain relations defined in incremental form. Conversely, data-driven mechanics assumes that such relations may not be known and instead, the material behavior is encoded in a *material data set* $\mathrm{D} = \mathrm{D}_1 \times \cdots \times \mathrm{D}_M$, where $\mathrm{D}_e \subset \mathbb{R}^{2m}$ is assigned to the material point e. Further, history-dependent material responses demand the definition of time-dependent data sets $\mathrm{D}^{k+1} \subset \mathrm{D}$ that contain, at

time t_{k+1}, stress-strain pairs compatible with certain evolution constraints and a given history $\{(\boldsymbol{\varepsilon}_e^s, \boldsymbol{\sigma}_e^s)\}_{s\leq k}$. The data-driven problem then reads

$$\inf_{\mathbf{y}\,\in\,\mathrm{D}^{k+1}} \inf_{\mathbf{z}\,\in\,\mathrm{E}^{k+1}} \|\mathbf{y}-\mathbf{z}\|^2 = \inf_{\mathbf{z}\,\in\,\mathrm{E}^{k+1}} \inf_{\mathbf{y}\,\in\,\mathrm{D}^{k+1}} \|\mathbf{y}-\mathbf{z}\|^2, \tag{2}$$

where $\|\square\|$ denotes a suitable metric. In order to consider materials with particle breakage, we further assume that the breakage variable $B \in [0,1]$ introduced in Einav [1] is available in the database. Then, we consider the time-dependent data set representation

$$\mathrm{D}_e^{k+1} := \left\{ \mathbf{z}_e \in \mathbb{R}^{2m} \;:\; \Phi\big(B_e^{k+1}, \{\boldsymbol{\varepsilon}_e^s\}_{s\leq k+1}, \{\boldsymbol{\sigma}_e^s\}_{s\leq k+1}\big) \right\}, \tag{3}$$

where Φ is a generic relation to be fulfilled by the local history of stress-strain pairs and the current breakage measure B_e^{k+1}. For instance, in this work, the irreversibility condition $B_e^{k+1} - B_e^k \geq 0$ is enforced. The key advantage of the definition (3) is that the breakage variable can be directly measured in experiments or lower-scale simulations, bypassing the need for phenomenological evolution laws.

3. Main results

Figure 1 shows the stress-strain response and the evolution of GSD resulting from an oedometer test on Ottawa sand. Data from experimental results and LS-DEM simulations are used to calibrate the constitutive model of Einav [1]. In contrast, the data is directly employed in the data-driven problem (2) through the data set representation (3). The data-driven computations properly extract the mechanical state and the evolution of GSD, highlighting the capabilities and possible advantages of the proposed methodology with respect to conventional constitutive modeling.

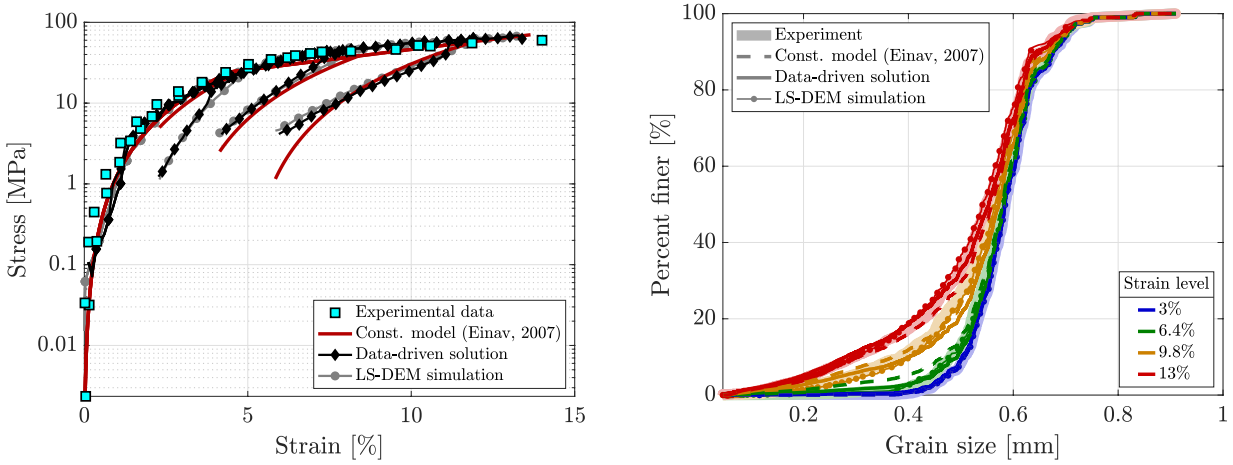

(a) Stress-strain response

(b) Evolution of GSD

Figure 1. Oedometer test: results from the data-driven computations and comparisons with experimental results, LS-DEM simulations, and Einav's continuum breakage model.

References

[1] Einav, I. (2007). Breakage mechanics—Part II: Modelling granular materials. *Journal of the Mechanics and Physics of Solids*, **55**, 1298–1320.

[2] Kirchdoerfer, T. and Ortiz, M. (2016). Data-driven computational mechanics. *Comp. Meth. Appl. Mech. Engng.*, **304**, 81–101.

A CYCLIC MULTILAMINATE CONSTITUTIVE MODEL FOR SANDS INCORPORATING ANISOTROPIC CRITICAL STATE THEORY

H. Bayraktaroglu, M.A. Hicks and M. Korff
Delft University of Technology, Delft, The Netherlands

Abstract

The microstructural anisotropy of soils which is associated with the distribution of voids and spatial orientation of particles is induced during the soil formation process in nature. Similar anisotropic formations are also observed in the laboratory environment as a result of different sample preparation methods. These granular level anisotropic characteristics can propagate and result in severe variations in field-scale predictions. In this study, the potential capability of the multilaminate (ML) framework to handle the effect of principal stress rotation and induced anisotropy has been further enhanced by incorporating anisotropic critical state theory (ACST). This new, state-dependent, semi-micromechanical bounding surface plasticity model is used to investigate the influence of fabric on the undrained response of sands.

Introduction

The anisotropic nature of soil results in direction dependent behaviour. Experimental studies carried out by varying stress paths and rotating principal stresses using simple and torsional shear tests show that soils with similar initial fabrics may show drastic differences in response. In the case of sands, the response can range from highly contractive flow liquefaction to dilative behaviour depending on the orientation of loading and fabric direction [1]. Similar fabric effects have also been observed in various types of boundary value problems.

Multilaminate framework and constitutive adaptation

Even though the history of the ML framework traces back to the slip theory proposed in ref. [2], its first application in soil mechanics was presented in ref. [3] for the investigation of cohesive soils. Since then the scope and performance of the framework have been continuously improved, and recently the authors of ref. [4] proposed a critical state based ML constitutive model for sands.

The application of the ML framework differs slightly from classical elastoplastic models. Unlike the classical constitutive modelling approach where the link between the stress and strain are defined in a tensorial field, in the ML framework, local stress and strain vectors are interconnected at so-called sampling planes which are by definition vectorial fields. The resistance against shearing/sliding and the resultant plasticity are calculated individually at each of these sampling planes using proper constitutive formulations and then transferred back to their global counterparts. A schematic of the framework is illustrated in Figure 1a.

In this study, the basics of the constitutive models employed at the sampling planes follow the work in ref. [5] where all the constitutive formulations are defined in a tensorial field. Hence, a multilaminate adaptation that downscales the tensorial formulations and terms into their vectorial counterparts is needed. Even though the detailed formulations are beyond the scope of this short abstract, the key terms used to define the constitutive formulations are illustrated in Figure 1b. The back-stress ratio vector $\boldsymbol{\alpha}$ and the stress ratio vector $\mathbf{r}$ generalise the slope of the yield surface and stress ratio, respectively, on the normalised shear plane. The loading direction vector $\mathbf{n} = (\mathbf{r} - \boldsymbol{\alpha}) / |\mathbf{r} - \boldsymbol{\alpha}|$ is used to define the direction of the image back-stress ratios. It is important to note that all these quantities are vectors whose components are defined in the n_s and n_t directions.

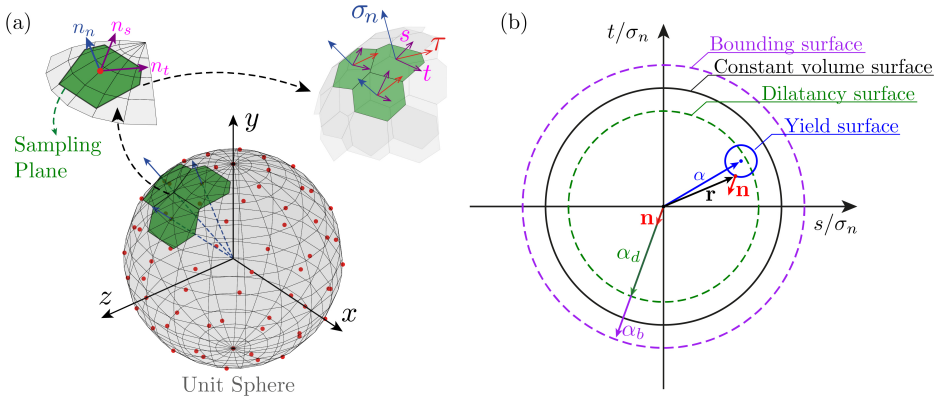

Figure 1. Schematic of multilaminate framework and local stresses (a) and characteristic surfaces (b)

Results

In Figure 2, undrained cyclic triaxial tests with three different initial fabric arrangements have been compared. The initially anisotropic configurations which are indicated with green and red lines result in lower liquefaction resistance than the initially isotropic case which is indicated by the blue line. Moreover, more plastic strains accumulate in both anisotropic cases compared to their isotropic counterpart. The difference between the two anisotropic cases arises from the different initial fabric orientations.

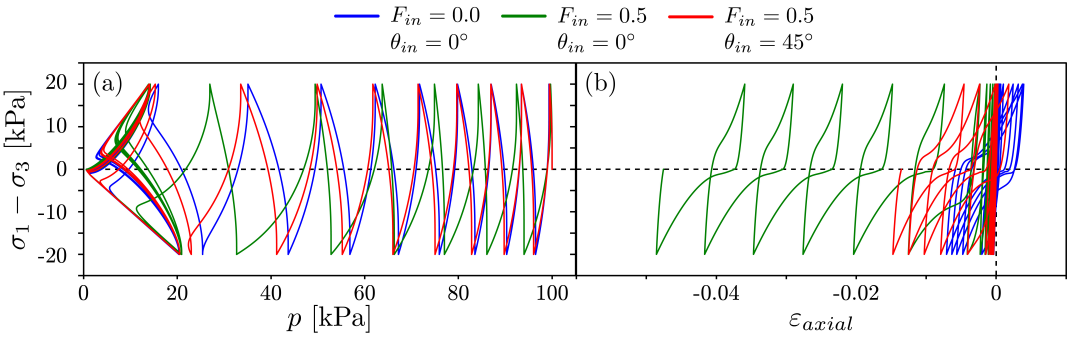

Figure 2. Influence of the fabric intensity F_{in} and orientation θ_{in} on sand behaviour in undrained triaxial test

Acknowledgements

The activity presented in the paper is part of the research programme DeepNL/SOFTTOP with project number DEEP.NL.2018.006, financed by the Netherlands Organisation for Scientific Research (NWO).

References

[1] Yoshimine, M., Ishihara, K., and Vargas, W. (1998). "Effects of principal stress direction and intermediate principal stress on undrained shear behavior of sand." *Soils and Foundations*, **38**(3), 179-188.

[2] Taylor, G. (1938). "Plastic strain in metals." *Journal of the Institute of Metals*, **62**, 307-324.

[3] Pande, G. N., and Sharma, K. G. (1983). "Multi-laminate model of clays—a numerical evaluation of the influence of rotation of the principal stress axes." *International Journal for Numerical and Analytical Methods in Geomechanics*, **7**(4), 397-418.

[4] Bayraktaroglu, H., Hicks, M. A., Korff, M. and Galavi, V. (2023). "A state-dependent multilaminate constitutive model for anisotropic sands." *Géotechnique*, in press.

[5] Li, X. S., and Dafalias, Y. F. (2012). "Anisotropic critical state theory: role of fabric." *Journal of Engineering Mechanics*, **138**(3), 263-275.

A SCALE-BRIDGING TECHNIQUE FOR GRANULAR MATERIALS UNDERGOING LARGE DEFORMATION

M. Wang, D.Z. Zhang
Los Alamos National Laboratory, Los Alamos, NM, USA

1. Introduction

The primary constituents of geomaterials, such as soil and rock, are granular particles. Constitutive models are essential in the modelling of material deformation, and their establishment is mainly based on the principle of objectivity. It has been reported that the principle of objectivity in classical mechanics is only an approximation that ignores the effect of inertial forces [1]. For solids undergoing infinitesimal deformation, the principle of objectivity works well. However, it is invalid for large deformation, especially for high-strain cases. It is known that developing proper constitutive models accounting for large deformation is extremely challenging. In such a case, the hierarchical multiscale modelling becomes an alternative way to solve the problem. In the existing framework of hierarchical multiscale techniques, the finite element method (FEM) and the material point method (MPM) are primarily used for continuum-level simulations, while the concept of a representative volume element (RVE) is employed to obtain the average stress at a Gauss point or material point. Currently, the discrete element method is the only tool used to carry out RVE simulations of granular materials at the grain level. Although a great progress has been made in the past twenty years, there are still certain challenges that need to be overcome so that the multiscale technique can better simulate the large deformation, especially those involving high strain rates, of granular materials. In this work, we will introduce a novel scale-bridging technique for hierarchical multiscale modelling.

2. An adaptive RVE model

In the hierarchical multiscale modelling, the primary difficulty is how to ensure the accuracy of stress calculated from RVE models. Particularly, when the RVE model experiences very large deformation, its computational domain may be distorted, resulting in not only computational difficulty but also loss of the representative property of a material point. To overcome these issues, we introduce our adaptive RVE model. Firstly, to better describe the deformation field of materials with a large strain rate, a uniform velocity gradient rather than uniform deformation/strain is applied to an RVE model. Using the conventional Lagrangian RVE model, the computational domain may be distorted when the RVE model has a large shearing deformation, though periodic boundary conditions are employed. Normally, in such a case reinitialization of the RVE model is required. However, reinitialization of the model leads to loss of history information, such as shear forces. To avoid reinitialization, an equivalent computational domain accounting for the deformation history of the material point can be selected to replace the deformed RVE model based on periodic boundary conditions at certain frequency, so that the computational domain is always a cuboid and thus avoiding reinitialization. Figure 1 a) shows a 2D case for illustration. The computational domain of this equivalent model can only stretch or shrink. To obtain such an adaptive model, it is found that the velocity gradient tensor should be upper-triangular, in other words entries below the main diagonal are zero. Usually, the velocity gradient passed from the continuum simulation is not upper-triangular. Fortunately, a velocity gradient can be uniquely decomposed into an upper-triangular strain-rate matrix and an antisymmetric spin tensor as follows,

$$\nabla \boldsymbol{v} = \begin{vmatrix} \frac{\partial v_x}{\partial x} & \frac{\partial v_x}{\partial y} & \frac{\partial v_x}{\partial z} \\ \frac{\partial v_y}{\partial x} & \frac{\partial v_y}{\partial y} & \frac{\partial v_y}{\partial z} \\ \frac{\partial v_z}{\partial x} & \frac{\partial v_z}{\partial y} & \frac{\partial v_z}{\partial z} \end{vmatrix} = \begin{vmatrix} \dot{\varepsilon}_{xx} & 2\dot{\varepsilon}_{xy} & 2\dot{\varepsilon}_{xz} \\ 0 & \dot{\varepsilon}_{yy} & 2\dot{\varepsilon}_{yz} \\ 0 & 0 & \dot{\varepsilon}_{zz} \end{vmatrix} + \begin{vmatrix} 0 & -w_z & w_y \\ w_z & 0 & -w_x \\ -w_y & w_x & 0 \end{vmatrix}, \tag{1}$$

where the angular velocity vector $\boldsymbol{\omega}_R$ of the rotating frame of reference is given below

$$\boldsymbol{\omega}_R = [\omega_x, \omega_y, \omega_z]^T = [\frac{\partial v_z}{\partial y}, -\frac{\partial v_z}{\partial x}, \frac{\partial v_y}{\partial x}]^T. \tag{2}$$

To account for the effect of spin tensor on the mechanical response of the RVE model, we introduce a rotating frame of reference to record the rotation of the RVE model (see Figure 1 a)); Meanwhile, inertia forces, such as the Euler force, the Coriolis force and the centrifuge force, caused by the rotating frame of reference will be applied to particles in the RVE model [2]. In such a way, the effect of velocity gradient, including geometric nonlinearity, is fully considered. The Cauchy stress in the RVE model can be expressed as a combination of Reynolds stress $\boldsymbol{\sigma}_R$ and contact stress $\boldsymbol{\sigma}_c$,

$$\boldsymbol{\sigma} = \boldsymbol{\sigma}_R + \boldsymbol{\sigma}_c; \boldsymbol{\sigma}_R = -\frac{1}{V}\sum_{i=1}^{n} m_i(\boldsymbol{v}_i - \overline{\boldsymbol{v}})(\boldsymbol{v}_i - \overline{\boldsymbol{v}}); \boldsymbol{\sigma}_c = \frac{1}{V}\sum_{i=1}^{n}\sum_{j=1}^{n_c^i} \boldsymbol{R}_i \boldsymbol{f}_{ij}, \tag{3}$$

where V is the volume of a particle packing; n is the total number of particles; m_i and $\boldsymbol{v}_i$ are, respectively, the mass and velocity of particle i; n_c^i is the total contact number of particle i with surrounding particles; R_i is the radius of particle i and $\boldsymbol{f}_{ij}$ is the contact force between particles i and j.

To explore the effect of spin tensor, in other words the inertia forces, on the mechanical response of the RVE model, the following numerical experiments with the shear rate $\dot{\gamma}_{xz} = 2\dot{\varepsilon}_{xz} = 0.1\ s^{-1}$ for all tests and different angular velocities $\omega_y = 0.0, 0.05, 0.15$ and $0.2\ s^{-1}$ are carried out, respectively. Other loading components in velocity gradient in (1) are zero. Fig. 1 b) shows the variation of first stress invariant of the RVE models under different rotation rates. It is known the first stress invariant is independent of spin tensor according to the principle of objectivity in classical mechanics. As shown in Fig. 1 b) the inertia forces have a significant effect on the stress when the rotation/shearing rate is greater than $0.15\ s^{-1}$, and should be considered in the deformation of granular materials.

In this work, we introduced an adaptive RVE model to overcome difficulties encountered in large deformation of granular materials. It is proved that our adaptive model can avoid the domain distortion of conventional RVE models. In addition, the effect of inertia forces caused by the rotating frame of reference is also investigated.

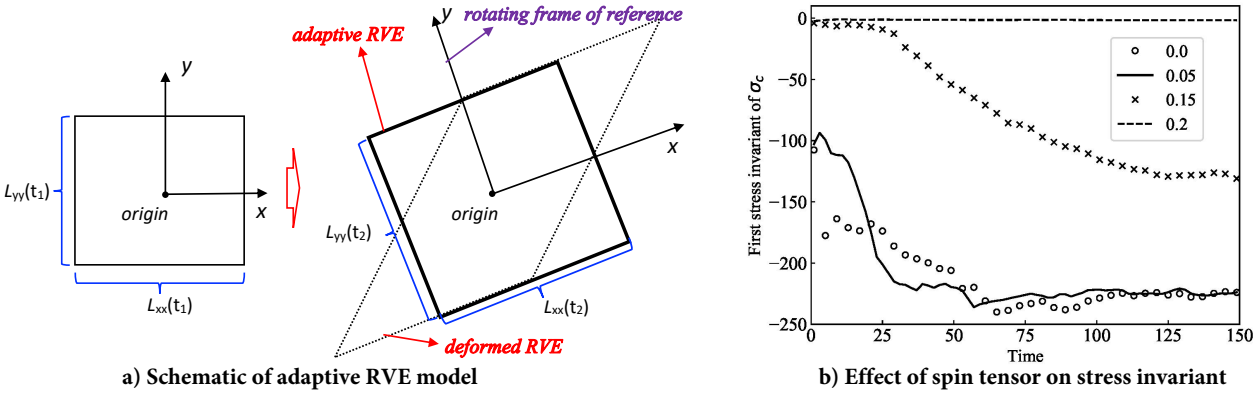

a) Schematic of adaptive RVE model **b) Effect of spin tensor on stress invariant**

Figure 1. a) Schematic of adaptive RVE model & b) Effect of spin tensor on first stress invariant

References

[1] Bird, R. and De Gennes, P. (1983). Discussion about the principle of objectivity. *Physica A*, **118**, 43–47.

[2] Wang, M. and Zhang, D. Z. (2021). Deformation accommodating periodic computational domain for a uniform velocity gradient. *Computer Methods in Applied Mechanics and Engineering*, **374**, 113607.

DEVELOPMENT OF AN EXTENDED STZ MODEL FOR GRANULAR SOILS SUBJECTED TO COMBINED STATIC LOADING AND VIBRATION

P. Guo, T. Xie and D.F.E. Stolle
McMaster University, Hamilton, Ont., Canada

1. Introduction

During the deformation process of granular materials, particles participate in the deformation process in clusters (or particle groups) instead of individually. These particle clusters form different types of meso-structures (on the scale of particle clusters), such as force chain segments and grain loops in the particle contact network. The motion and evolution of particle clusters have significant influence of the macroscopic deformation, such as deformation instability, localized deformation and failure modes. It is expected that both the microscale (on the scale of individual particles) and mesoscale information can help understand the underlying mechanisms behind macroscopic observations and incorporate more physics in constitutive modeling. A weak domain formed by a particle cluster, which can be referred to as the "shear-transformation zone" (STZ), is the main source of plastic deformations [1, 2]. In this work, an STZ model is developed to investigate the behaviour of granular soil when subjected to combined monotonic shearing and high-frequency, low-intensity (in terms of displacement amplitude) vibration. The theoretical analysis for this problem involves different spatial scales (micro-meso-macro) and temporal scales (slow monotonic shearing process and fast vibration process). The focus is on the shear resistance reduction (ViSRR) induced by vibration.

2. Formulation of the extended STZ model

The extended STZ model consists of three components: (1) the motion of STZs, including the transition, creation and destruction of STZs (as illustrated in Figure 1); (2) the relation between the motion of STZ number *n* and the observable, macroscopic plastic strain $\dot{\gamma}^{pl}$; and (3) the evolution of a "configurational temperature" T_{eff} that reflects the energy that drives the motion of the STZs:

$$\tau_0 \dot{n}_{\pm} = R_{\mp} n_{\mp} - R_{\pm} n_{\pm} + R_c\left(\sigma_s \dot{\varepsilon}_s^{pl}\right) - R_a\left(\sigma_s \dot{\varepsilon}_s^{pl}\right) n_{\pm} \tag{1}$$

$$\tau_0 \dot{\gamma}^{pl} = v_0 \xi \left(R_+ n_+ - R_- n_-\right) \tag{1}$$

$$C_V^{eff} \dot{T}_{eff} = T_{eff} \dot{S}_c = \dot{\mathcal{W}}_C\left(s_C, p, \{\Lambda_\alpha\}\right) + \eta D^{dev} : D^{dev} + \mathcal{K}\left(T_{eff}, \theta_k\right)\left(1 - T_{eff} / \theta_k\right) \tag{2}$$

In the above equations, $R_{\mp}(\sigma_s, \Psi, \chi)$ is the rate at which the STZ's are making forward and backward transitions, $R_c - R_a n_{\pm}$ describes the creation and destruction of STZs induced by mean plastic flow, R_a and R_c characterize the rate of STZ destruction and creation, respectively. Moreover, Ψ stands for the internal barrier for STZ motion at a configurational temperature χ that is chosen as the Edward compactivity, and T_{eff} is the effective temperature of the material. The directional dependency of STZ transition rate is determined by the Eshelby stress tensor in the following form:

$$\mathcal{R}(\alpha)=\nu_0\exp\left[-\frac{\Psi-\nu_0\Delta P(\alpha)}{\rho T_{eff}}\right]=R_0\exp\left[\frac{\nu_0(\sigma_{ik}\dot{u}_{j,k})e_i^{\alpha}e_j^{\alpha}}{\rho T_{eff}}\right] \tag{3}$$

with $R_0=\nu_0\exp\left(-\Psi/\rho T_{eff}\right)$ The rates of STZ creation R_a and collapse R_c are made proportional to the rate of plastic work $\dot{w}^p=s_{ij}D_{ij}^p$ such that

$$\mathcal{R}_a=\mathcal{A}_a\dot{w}^p,\quad \mathcal{R}_c=\mathcal{A}_c\dot{w}^p,\quad 2\mathcal{A}_c/\mathcal{A}_a=2\mathcal{R}_c/\mathcal{R}_a=n_{eq} \tag{4}$$

The external quasistatic and vibrational excitations are characterized as $\Gamma_{ij}=\tau_0R_{ij}^a=\tau_0\dot{M}_{ij}/K$ and $\Gamma_{vib}(\alpha)=\tau_0\sigma_{ij}^k\alpha_i\alpha_j/K$ with $\sigma_{ij}^k=\rho\left\langle v_i'v_j'\right\rangle=\rho T_{ij}^k$ being termed as the kinetic stress.

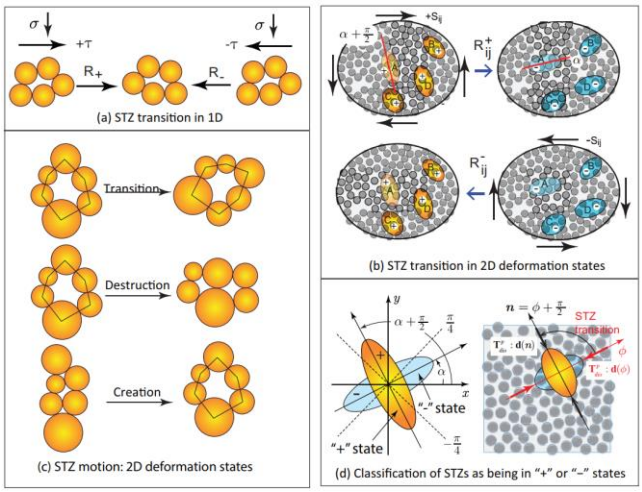

Figure 1. Illustration of STZ motion in granular materials.

3. Numerical examples and conclusions

Numerical examples are provided to demonstrate the performance of the extended STZ model, and the results are compared qualitatively with laboratory test results [3]. The laboratory tests reveal that high frequency, low-amplitude intensity vibration tends to induce shear resistance reduction and additional flow of dry granular materials originally subjected to quasi-static shearing. The extended STZ model can describe this phenomenon reasonably, at least qualitatively.

4. References

[1] Bouchbinder, E., & Langer, J. S. (2009). Nonequilibrium thermodynamics of driven amorphous materials. I. Internal degrees of freedom and volume deformation. *Phys. Rev. E*, **80** (3), 031131.

[2] Pechenik, L. (2005). Dynamics of shear-transformation zones in amorphous plasticity: Nonlinear theory at low temperatures. *Phys. Rev. E* , **72** (2), 021507.

[3] Xie, T., Guo, P. & Stolle, D. F. E. (2022). Experimental investigation of vibration-induced strength loss in sheared granular soil. *Can. Geotech. Journ.* https://doi.org/10.1139/cgj-2021-0662.

ON MODELING OF TIME-DEPENDENT BEHAVIOUR OF SOILS

T. Nakai[1], H.M. Shahin[2] and H. Takahashi[3]
[1] Geo-Research Institute, Nagoya, Japan
[2] Islamic University of Technology, Dhaka, Bangladesh
[3] JIP Techno Science, Osaka, Japan

A simple method to describe time-dependent behavior of various soils in 3D stress conditions is presented. In the previous model, the soil behavior was reliably captured using the t_{ij} concept [1], and the influence of density, confining pressure and structured behavior of naturally deposited soils was described using the subloading surface concept [2] and incorporating the effects of bonding [3, 4]. In the present model, the time-dependent properties are accounted for within the framework of subloading surface by considering the experimental fact that the normal consolidation line (NCL) shifts with strain rate. The approach does not use viscoplasticity, and only the coefficient of secondary consolidation is added as a parameter. In this work, the implicit formulation of the model is presented and the numerical examples involving undrained tests are provided.

1. Formulation of the model and numerical simulations of undrained shear tests

Figure 1 shows the yield function (f=0) and two kinds of plastic strain increments (*i.e.*, a component shown in red which satisfies the associated flow rule in t_{ij} space, and the one shown in blue arrow which is an isotropic component). To consider 3D effect appropriately, the yield function is formulated using stress invariants (t_N and t_S) based on the t_{ij} concept instead of usual (p and q), and the flow rule is assumed not in σ_{ij} space but in t_{ij} space. To account for the stress path dependency of strain increments, the plastic strain increments are expressed by the summation of the component satisfying the associated flow rule and the isotropic component.

Figure 2 shows the NCL line and the actual void ratio in the e – ln t_{N1} relation (t_{N1}: the value on t_N axis of the yield surface) at the initial state (denoted by subscript 0) and the current state. Here, NCL shifts with strain rate, and the amount of shift (ψ - ψ_0) is determined from the well-known secondary consolidation coefficient (λ_α) as shown in the interpolation diagram. The variable ρ implies difference between the actual void ratio and the void ratio on NCL for the same stress level. The variable ω is an imaginary increase in void ratio for describing the bonding effect of structured soil. Evolution rules of ρ and ω are defined by monotonically decreasing functions of plastic strain.

The return mapping equations of the model are expressed as

$$\begin{cases} \bullet\ \mathbf{b}_1 = \boldsymbol{\varepsilon}^e - \boldsymbol{\varepsilon}^{e(trial)} + \Delta\gamma\mathbf{N} - L^{(IC)} \ln\dfrac{t_N}{t_{N,n}}\left(\dfrac{\mathbf{N}}{\mathrm{tr}\mathbf{N}} - \mathbf{N}^{(IC)}\right) = 0 & (1) \\ \bullet\ b_2 = \rho - \rho_n - \Delta\gamma\left\{-(1+e_0)\sqrt{3}\,\dfrac{a\rho/(1+k_aX) + b\omega/(1+k_bX)}{t_N}\right\} + \psi - \psi_n - \Delta\psi = 0 & (2) \\ \bullet\ b_3 = \ln\dfrac{t_N}{t_{N0}} + \varsigma(X) - \dfrac{1+e_0}{\lambda-\kappa}\left\{\varepsilon^p_{v,n} + \Delta\gamma\mathrm{tr}\mathbf{N}\right\} - \dfrac{1}{\lambda-\kappa}\left\{(\rho_0-\rho) + (\psi_0-\psi)\right\} = 0 & (3) \end{cases}$$

where $\mathbf{N}$=$\partial f/\partial \mathbf{t}$, X=t_S/t_N. Superscripts (IC), e and p represent the isotropic component, and elastic and plastic components, respectively, while $\Delta\gamma$ is the plastic multiplier. The terms added to account for time-effect characteristics are enclosed in blue dashed lines in the above equations. The shift (ψ - ψ_0) is expressed as a function of the rate of equivalent plastic void ratio $(-\dot{e})^p_{(equ)}$

$$\psi - \psi_0 = -\lambda_\alpha \ln\left((-\dot{e})^p_{(equ)} \big/ (-\dot{e})^p_{(equ)0}\right) \qquad (4)$$

Figures 3 and 4 show (a) stress-strain curves, and (b) effective stress paths in undrained shear tests with varying strain rates on normally consolidated clay and structured clay. In these figures, black solid lines show the result without time effect, and blue curves show the results with time effect.

The model can describe the strain rate effects including isotach and the change in shape of effective stress path for structured clay.

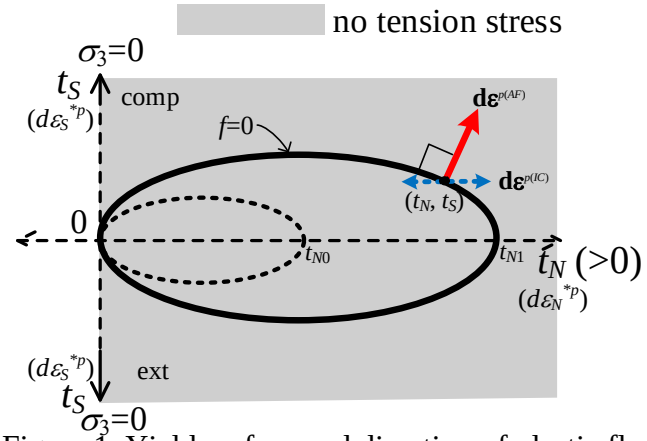

Figure 1. Yield surface and direction of plastic flow

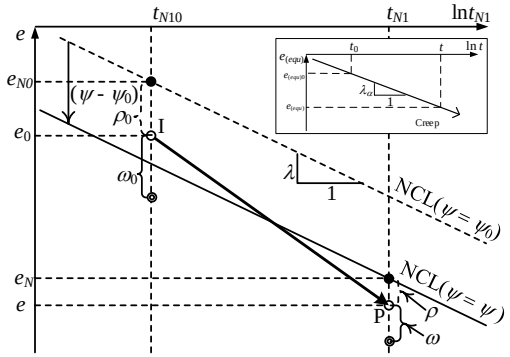

Figure 2. e – ln t_{N1} relation

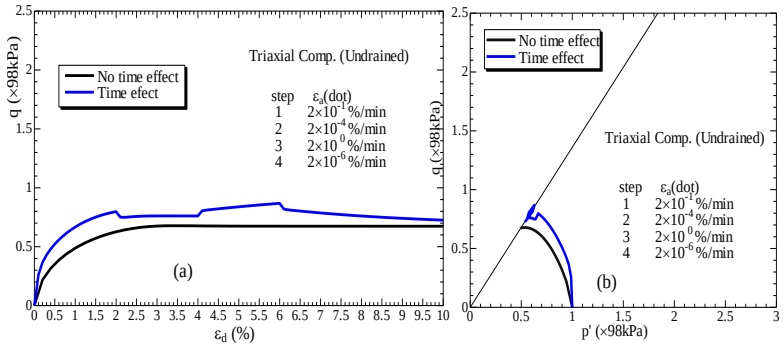

Figure 3. Simulation of normally consolidated clay

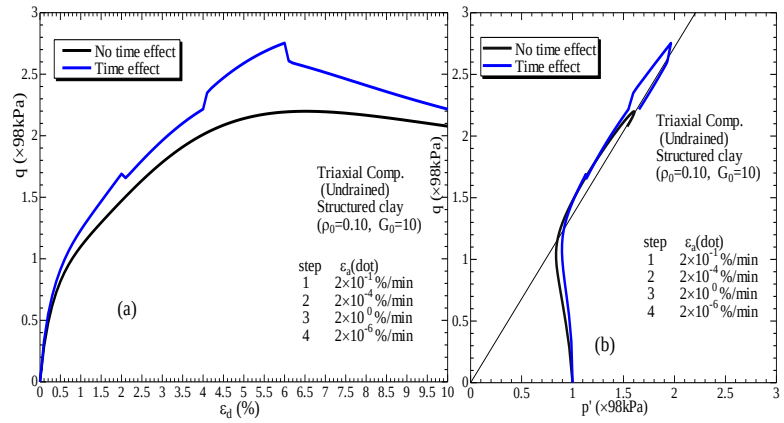

Figure 4. Simulation of structured clay

2. References

[1] Nakai, T. and Mihara, Y. (1984). A new mechanical quantity for soils and its application to elastoplastic constitutive models, *Soils and Foundations*, **24**(2), 82-94.

[2] Hashiguchi, K. (1980). Constitutive equation of elastoplastic materials with elasto-plastic transition, *Jour. of Appli. Mech., ASME*, **102**(2), 266-272.

[3] Nakai T., Shahin H.M., Kikumoto M., Kyokawa H., Zhang F. and Farias, M.M. (2011). A simple and unified three-dimensional model to describe various characteristics of soils, *Soils and Foundations*, **51**(6), 1149-1168

[4] Nakai, T. (2012). *Constitutive Modeling of Geomaterials: Principles and Applications*, CRC Press, Boca Raton/London/New York, 2012

NUMERICAL ANALYSIS OF ELASTOPLASTIC BEHAVIOR OF GEOMATERIALS AS MICROPOLAR CONTINUA

***F. Shi*[1,2,3], *N. Fantuzzi*[3], *P. Trovalusci*[4], *Y. Li*[1,2] *and Z. Wei*[1,2]**

[1] *State Key Laboratory of Coal Mine Disaster Dynamics and Control, Chongqing University, Chongqing, China*

[2] *School of Resources and Safety Engineering, Chongqing University, Chongqing, China*

[3] *DICAM Department, University of Bologna, Italy*

[4] *DISG Department, Sapienza University of Rome, Italy*

1. Background

The stability of slope formed by geomaterials such as soil and layered rocks is an important, interesting, and challenging research aspect for soil, mining, dam and road engineering. In the slope stability analysis, due to factors such as softening by water or load applied on the top, a relatively large plastic deformation can be inevitably observed in the slope, thereby forming a strain localized zone [1]. For the slope formed by complex geomaterials such as granular soil or layered rock blocks, the classical continuum theory may not be adopted because the internal lengths of the microstructure of such geomaterials should be considered [2]. Therefore, the non-local micropolar continuum theory, with the introduction of rotational degrees of freedom and the derived micro-curvatures, can allow us, due to the presence of scale parameters having the meaning of 'characteristic lengths', the analysis of strain localization problems avoiding ill conditioning in the field equations and mesh dependency in numerical solutions [3].

2. Methodology

According to ref.[4], the micropolar continuum belongs to the framework of implicit non-local continuum theories since it considers the microrotation of the material particles in addition to the classical (Cauchy continuum) displacement field. For example in 2D case, each material particle of the micropolar continumm has three degrees of freedom, i.e. two macro-displacements u_1, u_2 and one microrotation ω, whereas that of the Cauchy continumm only has u_1 and u_2. The existence of ω can results in the unsymmetric stress and strain tensors. Thus, measures of couple stress and micro-curvature should be introduced into the micropolar continuum. The linear elastic 2D micropolar constitutive relation can be written as:

$$\begin{Bmatrix} \boldsymbol{\sigma} \\ \boldsymbol{\mu} \end{Bmatrix} = \begin{bmatrix} \mathbb{A} & \mathbb{B} \\ \mathbb{B}^{\top} & \mathbb{D} \end{bmatrix} \begin{Bmatrix} \boldsymbol{\varepsilon} \\ \boldsymbol{\chi} \end{Bmatrix} \tag{1}$$

where $\boldsymbol{\sigma}$ and $\boldsymbol{\varepsilon}$ are stress and strain vectors; $\boldsymbol{\mu}$ and $\boldsymbol{\chi}$ are couple stress and micro-curvature vectors; submatrices $\mathbb{A}$, $\mathbb{B}$, $\mathbb{D}$ includes elastc constitutive components. As for the classical Cauchy continuum, the constitutive equation only relates stress to strain, i.e.:

$$\boldsymbol{\sigma} = \hat{\mathbb{A}}\boldsymbol{\varepsilon} \tag{2}$$

where $\hat{\mathbb{A}}$ is elastic constitutive components for the Cauchy continuum.

In the present study, in order to investigate the elastoplastic behavior of the slope formed by geomaterials, the finite element (FEM) codes for elastoplastic micropolar and classical Cauchy continua are developed in-house by considering a non-associated flow rule ($f(\boldsymbol{\sigma}, \boldsymbol{\mu}) = 0$) and the isotropic softening rule.Two kinds of geomaterials, i.e. soil and layered rocks, are considered for the slope and the elastic constitutive matrix is obtained from a homogenization procedure based on an energy equivalence criterion [5].

3. Simulation and main results

Based on above consideration, nonlinear elastoplastic FEM simulations using micropolar and classical Cauchy continua are conducted on an hypothetical slope (cf. Figure 1, where 4-nodes elements and complete Gauss-Legendre integration with 2×2 grid are considered in the FEM computation).

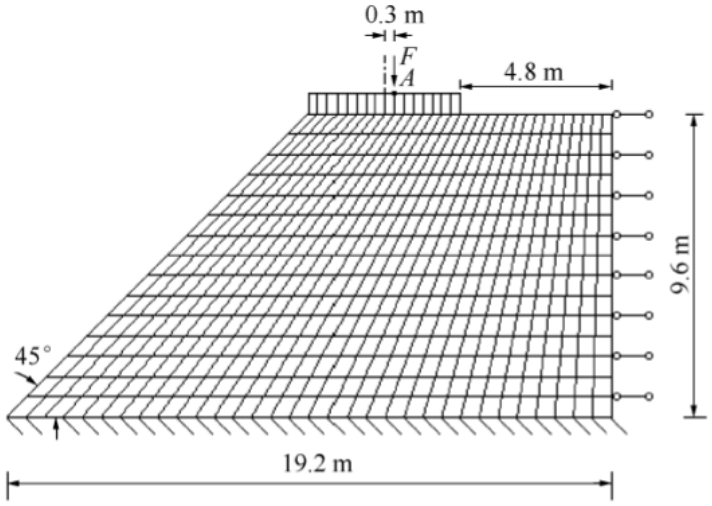

Figure 1. Sketch of the slope case with its finite element mesh.

It was found form results that the developed micropolar and Cauchy codes can both simulate the elastoplastic behavior for the slope close to failure conditions. The micropolar continuum is capable of accounting for the size effect in geomaterials. The plastic behavior of the micropolar continuum is closer to that of the Cauchy continuum when the scale parameter is small. As the scale parameter increases, the plastic zone from the micropolar continuum becomes wider, showing the occurrence of strain localisation areas. This work underlines the validity the micropolar theory when analyzing plastic response of a slope, which is essential for capturing more realistic behavior of geomaterials with various characteristic length.

References

[1] Duncan, J. M., Wright, S. G., and Brandon, T. L. (2014). *Soil strength and slope stability*. John Wiley & Sons.

[2] Tejchman, J. and Wu, W. (2009). Non-coaxiality and stress–dilatancy rule in granular materials: Fe investigation within micro-polar hypoplasticity. *International journal for numerical and analytical methods in geomechanics*, **33**, 117–142.

[3] Sluys, L., De Borst, R., and Mühlhaus, H.-B. (1993). Wave propagation, localization and dispersion in a gradient-dependent medium. *International Journal of Solids and Structures*, **30**, 1153–1171.

[4] Trovalusci, P. (2014). *Molecular Approaches for Multifield Continua: origins and current developments*, pp. 211–278. Springer Vienna.

[5] Trovalusci, P. and Masiani, R. (1999). Material symmetries of micropolar continua equivalent to lattices. *International Journal of Solids and Structures*, **36**, 2091–2108.

MODULAR ELASTOPLASTIC MODELLING OF GEOMATERIALS

G. Mortara
DICEAM, University of Reggio Calabria, Italy

1. Introduction

Over the years, many elastoplastic models for geomaterials were formulated accounting for various aspects of soil behaviour. In this work, an attempt is made to provide a modular formulation using a hierarchical yield surface and a generalised stress-dilatancy relationship. In this formulation, suitable hardening laws can be chosen as variables of the model to be coupled with closed or open yield criteria associated with the behaviour of both clays and sands (see e.g. [1]). The adoption of a hyper- or hypo-elastic law will complete the model formulation. In this abstract, the attention is drawn only to the yield surface and the stress-dilatancy relationship. More details on the methodology can be found in ref. [2, 4].

2. The yield surfaces

The general formula of the yield surface Φ is

$$\Phi = q^2 - [(1-\chi)\,\Phi_h + \chi\Phi_{co}]\,\Phi_{\rho f}^2 \tag{1}$$

where χ is a flag parameter (0 or 1) that allows to discriminate between the expressions of the two meridian functions Φ_h and Φ_{co}. These functions account for many meridian shapes and differ in the fact that function Φ_{co} naturally includes a tension cutoff. In view of their complex structure and the need to identify several parameters, the functions Φ_h, Φ_{co}, and $\Phi_{\rho f}^2$ are not reported here and the details in this respect are provided in refs. [1] and [2]. The calibration of surfaces when many parameters are involved can only be performed with the aid of an automated procedure based on the comparison between a target yield surface and surfaces related to function (1). As an example, in Fig. 1 surfaces Φ_h and Φ_{co} are compared with the target composite surface introduced in ref. [3]. As can be seen the agreement is very good especially for surface Φ_{co} that also includes the tension cutoff.

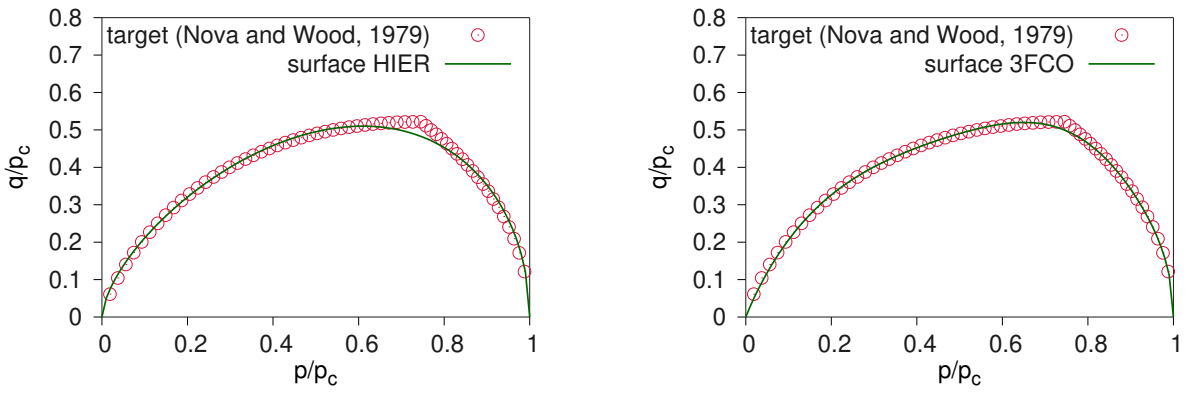

Figure 1. Comparison of target surface from ref. [3] with surfaces Φ_h (HIER) and Φ_{co} (3FCO).

3. The plastic potential

Plastic potentials are principally based on stress-dilatancy relationships (SDR) and are obtained by the integration of the flow rule differential equation. An alternative is that for a given SDR the related plastic potential is defined as an auxiliary surface giving the same rate of dilation as shown in [4]. The hierarchical expression of the stress-dilatancy relationship used here is

$$d_0 = \frac{M_g^b - \eta_0^b + cM_g\left(\eta_0 - M_g\right)}{\mu_1 + \mu_2\eta_0} \tag{2}$$

where d_0 and $\eta_0 = q_0/p$, q_0 being the value of q for $\theta = 0$, are the rate of dilation and the stress ratio under triaxial compression conditions, respectively. Parameters M_g, b, c, μ_1, and μ_2 characterize the SDR. The auxiliary plastic potential is put in the form

$$g = q^2 + \Phi_g \Phi_{\rho g}^2 \tag{3}$$

where Φ_g and $\Phi_{\rho g}$ are the meridian and deviatoric traces of g, respectively. Function Φ_g is represented by an ellipse while $\Phi_{\rho g}$ has the same expression as $\Phi_{\rho f}$ even though different parameters can be used. Similar as in the case of yield surfaces, an automated procedure was implemented to determine the parameters of (2). Figure 2 gives evidence of a very good agreement between the SDR reported in ref. [3] and the one proposed here.

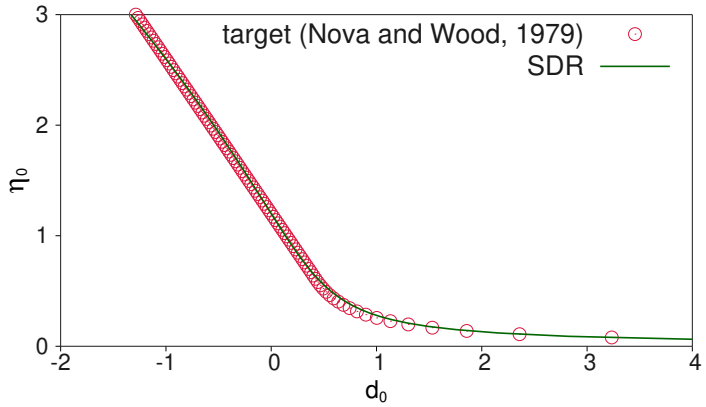

Figure 2. Comparison of the target SDR by [3] with the SDR proposed here.

4. Conclusions

Dealing with different elastoplastic formulations is possible by assuming generalized expressions for yield surfaces and plastic potentials. The problem of deriving parameters is overcome by automatic procedures based on the comparison between target yield surfaces and stress dilatancy relationships with the expressions provided in this work. A future development of this work is the implementation of a web site to apply these procedures and to use the related models as an online resource.

References

[1] Mortara, G. (2015). A constitutive framework for the elastoplastic modelling of geomaterials. *International Journal of Solids and Structures*, **63**, 139–152.

[2] Mortara, G. (2019). A new yield criterion for soils with embedded tension cut-off. *Meccanica*, **54**, 683–696.

[3] Nova, G. and Wood, D. M. (1979). A constitutive model for sand in triaxial compression. *International Journal for Numerical and Analytical Methods in Geomechanics*, **3**, 255–278.

[4] Mortara, G. (2021). Auxiliary plastic potential approach in elastoplasticity for soils. *Géotechnique Letters*, **11**, 221–229.

APD – AN AUTOMATED SYSTEM FOR DETERMINING PARAMETERS FOR CONSTITUTIVE MODELS BASED ON IN-SITU TESTS

I. Marzouk and F. Tschuchnigg
Graz University of Technology, Graz, Austria

1. Introduction

Determining soil parameters from in-situ tests has some advantages over laboratory tests. Nevertheless, it is not possible to derive the parameters directly. Very often correlations between parameters and in-situ tests results are required to estimate those parameters. Several guidelines are available in literature dealing with in-situ tests interpretation such as [1-2] for the cone penetration test (CPT) and [3] for the dilatometer test (DMT).

An ongoing research project aims to create an automated parameter determination (APD) system to determine constitutive model parameters using in-situ tests. The framework is based on a graph-based approach that inherits some of the characteristics of graph theory [4].

2. Graph-based approach

The framework is built in the programming language Python and consists of several connected modules to derive parameters from in-situ tests (CPT and DMT) as described in [5]. The implemented graph-based approach is described in detail in [4]. An example of the generated graph is shown in Figure 1, where source parameters are connected to destination parameters via intermediate parameters. The connection is generated based on the given set of methods. Within the framework of APD, the general term ‘method’ substitutes the terms of ‘correlation’, ‘formula’, ‘equation’ and ‘rule of thumb’ [4].

The generated graphs are considered as weighted directed graphs, where a direction between the pairs of nodes in the graph is defined. Searching for a path in a network from one node to another is a common problem that has been used in different applications. Several graph algorithms exist for solving the shortest path problem. However, those algorithms are not valid for the parameter determination framework as they cannot be applied to branching paths. In APD, a path to the destination node can have more than one source node as the parameters in the path can be obtained from multivariable formulas that depend on multiple input parameters (branching paths occur in the framework). As a result, the existing graph algorithms are not suitable for the parameter determination framework [4].

Two types of nodes are introduced to deal with branching paths, namely parameters (green, yellow and red nodes in Figure 1) and methods (blue nodes in Figure 1). Very often, method nodes are empirical correlations that depend on more than one parameter. Consequently, method nodes have several incoming edges which indicate all the required parameters for this method.

To generate the graph, the system requires external inputs, namely methods and parameters. Methods and parameters are defined separately in two spreadsheets in comma-separated values (CSV) format. Each CSV file has specific properties as described in [5]. The current version of APD (CPT and DMT) consists of more than 150 methods.

3. In-situ tests interpretation

The framework is able to interpret results of CPT and DMT. This is performed based on the provided database (either by the standard database provided with the system or by another preferred database provided by the user). The system converts the imported test into layers. The stratification is carried out by one of the implemented stratification algorithms or manually by the user of the

system (by defining the boundaries of each layer). Each layer has an assigned soil behaviour type SBT (depending on the classification chart). After defining the layers, the measurements (raw data) in each layer are averaged. SBT of each layer controls which methods are to be used for computing a certain parameter. In case a layer has a SBT corresponding to fine-grained soils, only methods describing fine-grained soils will be used. Finally, graphs (e.g., Figure 1) are generated presenting the links between parameters and methods and the computed value(s) for all parameters.

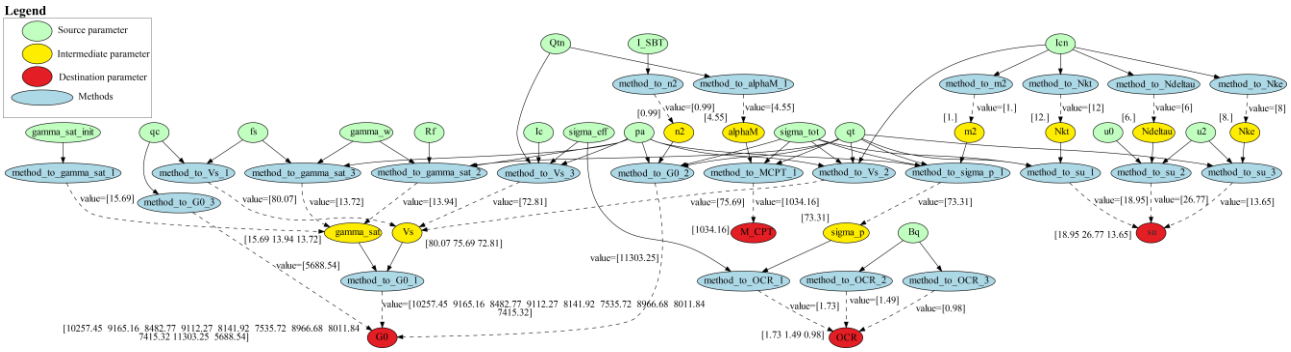

Figure 1. Example for a generated graph for a CPTu test.

4. Conclusions

APD is a transparent and adaptable framework. It allows the users to incorporate their knowledge and expertise to the system. The current version of APD consists of more than 150 methods (CPT and DMT). When all the methods in the database are used, a wide scatter in the computed values is obtained. Dealing with the scatter and selecting a suitable approach for assessing the accuracy of the computed values is part of current research activities.

The transition from the in-situ measured response to constitutive model parameters is under consideration. Methods for deriving parameters for some constitutive models, such as the Hardening Soil Small Strain Model (HS small) [6], are already included in the database. This is a key aspect of the framework.

Finally, the expansion (by including additional in-situ tests and measured in-situ shear wave velocity) of the framework, validating the output (by comparing the output of APD to interpreted values from laboratory tests) and updating and improving the database is part of ongoing research.

5. References

[1] Lunne, T., Robertson, P. K. & Powell, J. J. M. (1997). *Cone Penetration Testing in Geotechnical Practice*. First edition. Boca Raton, FL: CRC Press.

[2] Mayne, P. (2007). In-Situ Test Calibrations for Evaluating Soil Parameters, *In Characterisation and engineering properties of natural soils*.

[3] Marchetti, S., Monaco, P., Totani, G. & Calabrese, M. (2001). *The Flat Dilatometer Test (DMT) In Soil Investigations – a Report by the ISSMGE Committee TC16*.

[4] Van Berkom, I.E, Brinkgreve, R.B.J., Lengkeek, H. J. & de Jong, A. K. (2022). An Automated System to Determine Constitutive Model Parameters from in Situ Tests, *Proceedings of the 20th International Conference on Soil Mechanics and Geotechnical Engineering, Sydney 2021*.

[5] Marzouk, I., Tschuchnigg, F., Paduli, F., Lengkeek, H. J. & Brinkgreve, R.B.J. (2022). Determination of Fine-Grained Soil Parameters Using an Automated System, *In Cone Penetration Testing 2022, 540–45.*

[6] Benz, T. (2007). *Small-Strain Stiffness of Soils and Its Numerical Consequences.* Ph.D. thesis, University of Stuttgart.

NUMERICAL AND EXPERIMENTAL INVESTIGATIONS INTO FORCE CHAIN NETWORKS IN SOILS: A GRADING ENTROPY APPROACH

J. Leak[1], D. Barreto[1] and E. Imre[2]

[1] Edinburgh Napier University, Edinburgh, United Kingdom
[2] Óbuda University, Budapest, Hungary

1.Introduction.

Granular materials can be linked to their particle size distribution (PSD). The effect of PSD on soil fabric is significant. Fabric refers to the geometric arrangement of particles in a specimen [3] and dictates the propagation of forces through a granular material. As force is applied to a granular system, it may be transmitted via fabric in two ways: (1) through strong and (2) weak force chains.

Radjai et al. [2] suggested that strong force chains align themselves vertically, in the direction of the major principal stress, taking on larger proportions of force. The strong force chain network is supported orthogonally by networks that carry less stress, known as weak force chains. The weak force chain network is suggested to be aligned in the minor principal stress direction. The effect of polydispersity and soil fabric was studied in ref. [1]. It was suggested that as polydispersity increased, larger particles in the PSD were associated with the strong force chain network, whereas smaller grains were associated with the weak network. Whilst the mechanisms of force chains have been studied widely, few works have explored the effect of PSD more than that of ref. [1]. The present work aims to further the understanding of PSDs role in force chain mechanisms.

2. Methodology

To understand the role of the entire PSD, grading entropy coordinates [4] were used. Grading entropy 'condenses' the entirety of a PSD to a single point on a Cartesian plane. In this work, the normalised grading entropy coordinates were used as defined in Eqs (1). 'A' is the normalised base entropy, a logarithmic mean of the average grain diameter, and 'B' is the normalised entropy increment, a measure of how many fractions are required to describe the PSD, i.e.

$$A = \frac{S_0 - S_{0min}}{S_{0max} - S_{0min}}, B = \frac{\Delta S}{\ln(N)} \quad (1)$$

where S_0 and ΔS are the non-normalised base entropy and the entropy increment respectively, and N is the number of fractions in the PSD. These coordinates were used to interpret the behaviour of undrained monotonic triaxial tests on three PSD mixtures made from spherical glass ballotini. PSDs were made of two grain sizes: 1 mm – 1.4 mm and 0.5 mm – 0.75 mm. These grain sizes were mixed to create PSDs of 0% (1 mm – 1.4 mm), 20% (80% of 1 mm – 1.4 mm and 20% of 0.5 mm – 0.75mm) and 40% (60% of 1 mm – 1.4 mm and 40% of 0.5 mm to 0.75 mm). To interpret the microscale/contact behaviour, Discrete Element Method (DEM) simulations replicate the physical experiments.

2. Results, discussion and conclusions

It was seen that changes in the mechanical coordination number (Z_m) mirrored changes in

the normalised base entropy (A), suggesting that reductions in stress transmitting contacts are associated with decreases in the A-coordinate. As a result, 'A' may characterise the coarse grain fraction. The relationship between the normalised coordinates and fabric was further investigated using the deviatoric fabric tensor 'Φ_d' and its principal major and minor fabric components 'Φ_1', and 'Φ_3' [5] (see Fig. 1).

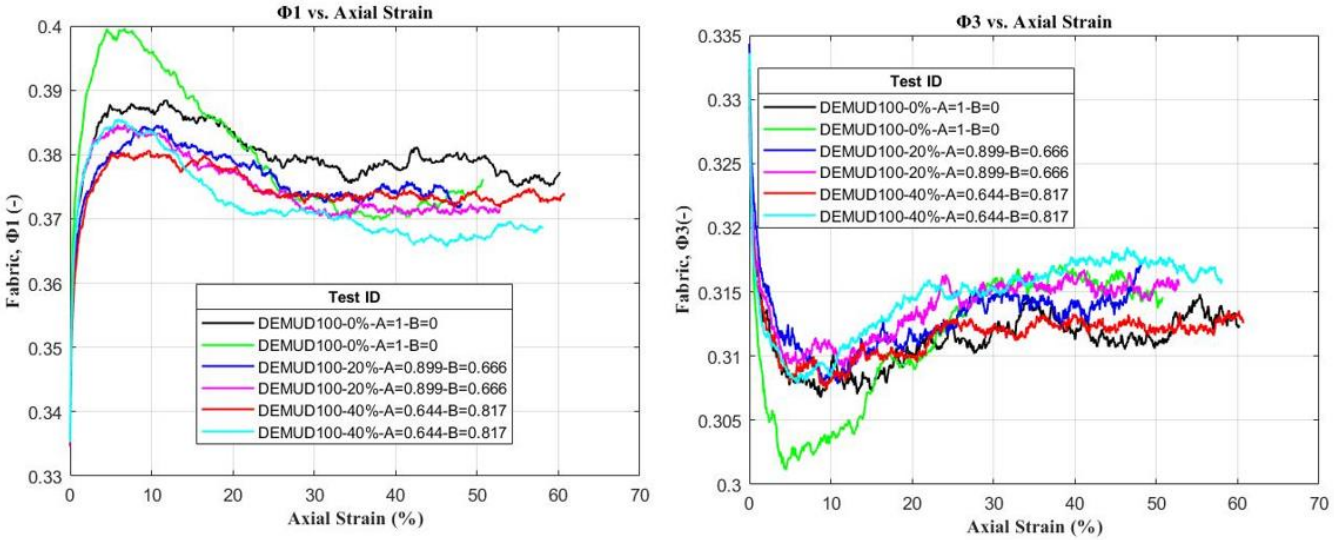

a) b)

Fig 1 a) Φ_1 with axial strain. Specimens made of a 0% PSD show greater concentrations of contacts in the major fabric direction. b) Φ_3 with axial strain. Specimens made of a 20% and 40% PSD show greater concentrations of contacts in the minor fabric direction.

Referring to Fig. 1, PSDs containing 40% finer particles showed the lowest concentration of contacts in the major fabric direction after Φ_{1peak} and exhibited the 3rd highest Φ_1 values following the 0% PSDs. This suggested that the 40% PSDs were able to create strong force chain networks prior to Φ_{1peak}, but following this, force transmission shifted to the weak force chain network. The largest Φ_3 values were associated with PSDs with greater B-coordinates (40%). This indicates the that the weak force chain network is more active in these PSDs and may depend on the fraction variety of the PSD. Based on these findings, the A-coordinate is suggested to characterise the strong network, whereas the B-coordinate relates to the weak network.

4. References

1. C. Voivret, F. Radjaı, J.-Y. Delenne, and M. S. El Youssoufi. (2009). Multiscale Force Networks in Highly Polydisperse Granular Media. Physical Review Letters. PRL 102, 178001 DOI: http://dx.doi.org/10.1103/PhysRevLett.102.178001
2. F. Radjaï, D.E. Wolf, M. Jean, J.J. Moreau. (1998). Bimodal character of stress transmission in granular packings**.** Phys. Rev. Lett., 80, pp. 61-64
3. Holtz, D.R. and Kovacs, D.W. (1981) An Introduction to Geotechnical Engineering. Prentice-Hall, Inc.
4. Lőrincz, J. (1986). Grading entropy of soils. PhD Thesis, Tech Sc, Technical University of Budapest (in Hung)
5. Satake M (1982) Fabric tensor in granular materials. In: Vermeer PA, Luger HJ (eds) IUTAM symposium on deformations and failure of granular materials. Balkema, Rotterdam, pp 63–68

THE COMPUTATION OF SOIL WATER RETENTION CURVES FROM PARTICLE SIZE DISTRIBUTIONS: ASSESSING THE ASSUMPTIONS

D. Barreto[1], E. Imre[2] and J. Leak[1]
[1] Edinburgh Napier University, Edinburgh, United Kingdom
[2] Óbuda University, Budapest, Hungary

1. Introduction

It is well recognised that the soil water retention characteristics are important to model the hydro-mechanical response of unsaturated soils. For this purpose, Wang, *et al* [1, 2] suggested computing the soil water retention curve (SWRC) from the particle size distribution (PSD). The process of determining the SWRC from the PSD follows the method proposed by Arya, *et al* [3]. Although the method is used extensively by soil scientists, its simplifying assumptions may be quite significant within the context of geotechnical modelling. Hence, the objective of the work presented here was to assess the effect of the assumptions required to estimate the SWRC from the PSD on the computed SWRC.

2. Methods and assumptions

The computation of the SWRC requires prior estimation of the pore-size distribution (POSD) which is computed from the PSD. The process described in detail in refs. [1-3] entails first dividing the PSD into many (N) size fractions. Then the following assumptions are required:

1. In each size fraction N_i (with $i = 1$, ..., N), all particles have spherical shape and equal size.
2. The specific gravity (G_s) of all particles for all N fractions is the same.
3. The volume of resulting pores corresponding to each size fraction is approximated as capillary tubes whose radii are closely related to the particle size in the fraction.
4. The total pore length is assumed in the form of $2n_i^{\alpha}R_i$, where R_i is the particle radius of fraction i, α is a model parameter related to particle shape and orientation, and n_i is the number of (spherical) particles in a cubic packing of uniform-size. On the basis of empirical data, the authors in ref. [3] suggest $1.3 \leq \alpha \leq 1.5$, while those in refs. [1, 2] used $1.35 \leq \alpha \leq 1.39$ for a smaller number of soil types.

The POSD may be first computed from the PSD, and the SWRC may then be computed as a function of the POSD. The process may be described as follows. The pore volume associated with each size fraction (N_i) may be obtained using the following phase relationship:

$$V_i = (W_i/G_s)e \tag{1}$$

where V_i is the pore volume per unit mass in the i^{th} particle size range, e is the void ratio and W_i is the mass percentage retained in the i^{th} range. Note that $\sum_{i=1}^{N} W_i = 1$. The number of particles (n_i) is then estimated as:

$$n_i = \frac{6W_i}{\pi D_i^3 G_s} \tag{2}$$

where D_i is the (average) particle diameter in the i^{th} fraction. The pore diameter (d_i) corresponding to each fraction i may then be calculated as:

$$d_i = D_i \left(\frac{4en_i^{(1-\alpha)}}{6}\right)^{0.5} \tag{3}$$

and the suction corresponding to each pore size (P_i) may be obtained from the Washburn equation as:

$$P_i = \frac{-4T_s \cos\theta}{d_i} \tag{4}$$

In order to complete the SWRC, the cumulative degree of saturation ($S_{r_{(i)}}$) can be determined by:

$$S_{r_{(i)}} = \frac{\sum_{i=1}^{j} V_i}{\sum_{k=1}^{N} V_k} \tag{5}$$

3. Results, discussion and conclusions

Following the procedures described in Section 2, several parametric analyses were performed. Fig. 1 shows the sensitivity of the resulting SWRC for a silty sand to the variation of the α parameter, that has been found to be the parameter with the most significant influence on the computation of the SWRC. As it can be seen, even when the range of α is reduced as reported by [1], the effect may not be negligible.

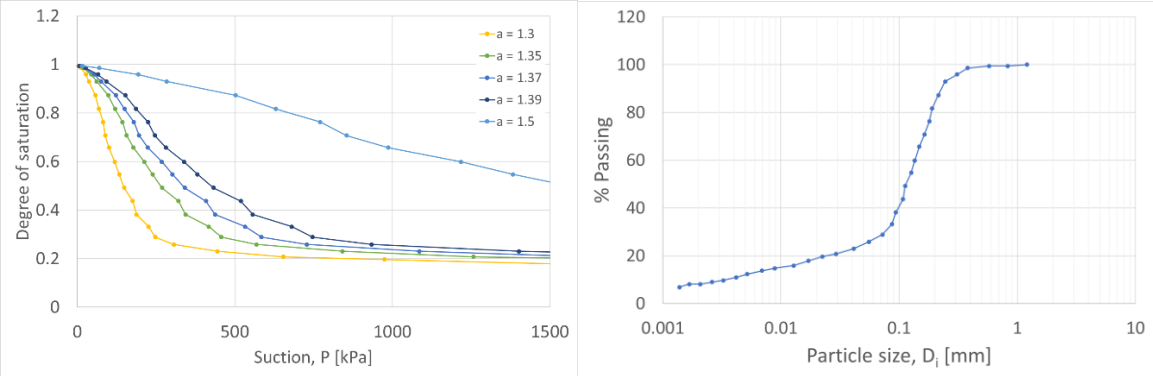

Fig. 1. a) Effect of the value of a on the computation of the SWRC for a silty sand, b) PSD of the silty sand. (Note that e = 0.43 and G_s = 2.69 n these calculations)

Considering all the assumptions described in the previous section, it is perhaps unsurprising that the value of α has the largest effect. Not only is this value related to particle shape and fabric (which have not been rigorously quantified by any study within this context), but it also affects the number of particles (n_i), which is in turn a significant assumption. The findings of this preliminary study suggest that the determination of the SWRC on the basis of PSD may be significantly improved. Existing computational power has enabled researchers to simulate numerical assemblies of particles both with and without consideration of particle shape using Discrete Element Method (DEM) simulations. Performing such simulations, even without considering partial saturation effects, yet focusing on the effect of PSD and particle shape on fabric, void ratio and local variations of pore volume only, may provide significant insight to enhance the simplified model described here. Such work is currently being conducted by the authors.

4. References

[1] Wang, M., Kong, L. & Zang, M. (2015). Effect of sample dimensions and shapes on measuring soil-water characteristic curves using pressure plate. *Journal of Rock Mechanics and Geotechnical Engineering*, **7**(5), 463–468.

[2] Wang, M., Pande, G.N., Kong, L. & Feng, Y.T. (2017). Comparison of pore-size distribution of soils obtained by different methods. *International Journal of Geomechanics*, **17**(1):06016012

[3] Arya, L.M., Leij, F.J., Shouse, P.J. & van Genuchten, M.T. (1999). Relationship between the hydraulic conductitvity function and the particle-size distribution. *Soil Science Society of America Journal*, **63**(5), 1063–1070

2. Modelling of instabilities and localized deformation

FORERUNNING FRACTURE IN DRY AND FULLY SATURATED POROUS SOLIDS

T. Ni[1], U. Galvanetto[2], M. Zaccariotto[2] and B. A. Schrefler[3]

[1]State Key Laboratory of Geohazard Prevention and Geoenvironment Protection, Chengdu University of Technology, China.

[2]Industrial Engineering Department, University of Padova, Padova, Italy

[3]Department of Civil, Environmental and Architectural Engineering, University of Padova, Padova, Italy

1. Introduction

A FEM and a novel hybrid FEM and Peridynamic modelling approach are used to predict the forerunning [3] fracture behaviour in dry and saturated porous solids. Both under the action of applied forces and fluid injection, forerunning fracture events are observed in the structure in dynamics [1]. It will be shown that: i) in dry bodies, the forerunning increases the overall fracturing speed and is, in fact, a mechanism for a crack to move faster when a steady-state propagation is no longer supported by the body/structure due to a high level of external forces; ii) in presence of the forerunning, interaction with the waves in the fluid phase increases the average speed even further compared to the movement in the same dry bodies; iii) the forerunning is an undeniable source of stepwise crack tip advancement of the main crack in continuum models; and iv) the forerunning phenomenon deserves further scrutiny because of its importance in geophysics as far as earthquake events are concerned.

2. Governing equations and numerical solution

In the whole domain Ω of a porous medium, the behaviour of solid phase is governed by the ordinary state-based peridynamic equation:

$$\rho \ddot{\boldsymbol{u}}\left(\boldsymbol{x},t\right)=\int_{\mathcal{H}_x}\left\{\underline{\mathrm{T}}\left[\boldsymbol{x},p,t\right]\left\langle\boldsymbol{\xi}\right\rangle-\ \underline{\mathrm{T}}\left[\boldsymbol{x}',p',t\right]\left\langle-\boldsymbol{\xi}\right\rangle\right\}dV_{x'}+\boldsymbol{b}\left(\boldsymbol{x},t\right)$$

and the flow field in the saturated porous media is described by Darcy's law, yielding the mass conservation as:

$$\rho s\frac{\partial p}{\partial t}+\rho\alpha\frac{\partial\varepsilon_v}{\partial t}+\rho\nabla\cdot\left[\frac{k}{\mu^w}\left(\nabla p+\rho g\right)\right]=q$$

In a plane discretization, the solid portion is discretized by peridynamic (PD) nodes and the fluid portion is discretized by 4-node FE elements. PD nodes and FE nodes share the same coordinates. A 'staggered approach' is used to solve the coupled system: the peridynamic and FEM equations are solved sequentially, and the previously obtained results for u and p are used to evaluate the fluid volumetric source terms or nodal forces for the next solving sequence.

3. Results

The geometry and constraints of the considered rectangular structure are shown in Figure 1. The mechanical and fluid parameters used in the calculation are, Young's modulus: $E = 10 GPa$, Poisson's ratio: $\upsilon = 0.2$, critical energy release rate: $G_c = 1 J/m^2$, porosity: $n_r = 0.002$, mass density: $\rho_r = \rho_f = 1000 kg/m^3$, Biot constant: $\alpha = 1$, bulk modulus and viscosity coefficient of the fluid: $K_w = 2.2\ GPa$ and $\mu_w = 10^{-3}\ Pa.s$, permeability coefficient of the reservoir domain: $k_r = 10^{-12} m^2$.

Two different loading conditions, mechanical loading and fluid injection, are adopted [2]. In the mechanical loading case, concentrated forces, 25000N, are applied on the up and down-facing surfaces of the initial crack at the central position to force its opening, and both dry and saturated condition are considered. In the fluid injection case, the injection rate is adopted as $Q = 5 \times 10^{-2}\, m^2/s$. In the simulation, forerunning of the fracture is observed, see Figures 2a to 2c. As shown in Figures 3a-3d, the wave propagation of pore pressure is also observed in the saturated structures both under the action of mechanical loading and fluid injection.

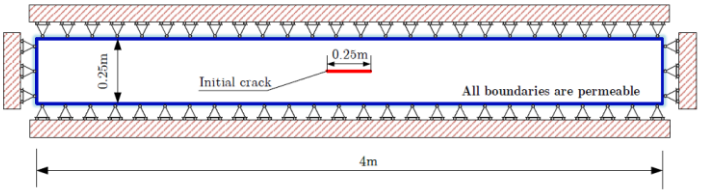

Figure 1. Geometry and constraints of the rectangular structure with a central initial crack

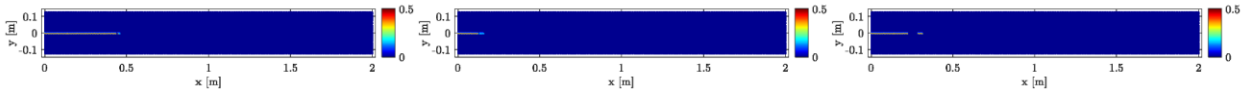

(a) Mechanical loading (dry). (b) Mechanical loading (saturated). (c) Fluid injection (saturated).

Figure 2. Forerunning fracture in the front of the crack tip.

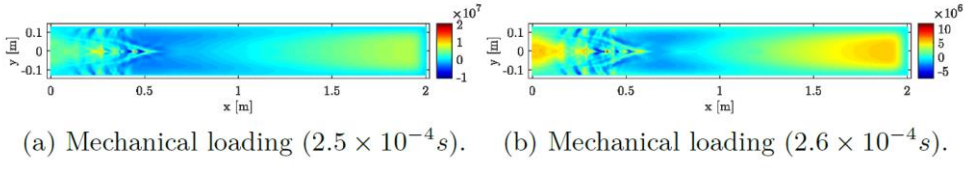

(a) Mechanical loading ($2.5 \times 10^{-4}s$). (b) Mechanical loading ($2.6 \times 10^{-4}s$).

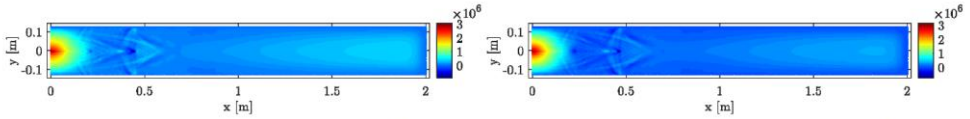

(c) Fluid injection ($4.5 \times 10^{-4}s$). (d) Fluid injection ($4.6 \times 10^{-4}s$).

Figure 3. Wave propagation of pore pressure in the saturated structures

4. References

1. Milanese, E., Ni, T., Peruzzo C., Zaccariotto, M., Galvanetto, U., Mishuris, G. S. & Schrefler B. A. (2022) Forerunning and bridging in dry and saturated fracturing solids, in "*Current Trends and Open Problems in Computational Mechanics*" (F.Aldakheel, B. Hudobivnik, M. Soleimani, H. Wessels, C. Weissenfels, and M. Marino, eds), Springer, 343-354.
2. Ni, T., Pesavento, F., Zaccariotto, M., Galvanetto, U., Schrefler , B.A. (2021) Numerical simulation of forerunning fracture in saturated porous solids with hybrid FEM/Peridynamic model, *Computers and Geotechnics*, doi.org/10.1016/j.compgeo.2021.104024.
3. Slepyan, L., Ayzenberg-Stepanenko, M., Mishuris G. (2015) Forerunning mode transition in a continuous waveguide, *J. Mech. Phys. Solids*, 78, 32–45.

ANALYSIS OF THE EFFECT OF THE LODE ANGLE ON THE STRAIN LOCALIZATION CONDITIONS IN A POROUS SANDSTONE

C. Couture[1, 2] and P. Bésuelle[1]
[1] Univ. Grenoble Alpes, CNRS, Grenoble INP, Lab. 3SR, Grenoble, France
[2] Port and Airport Research Institute, Yokosuka, Japan

1. Introduction

The development of planar kinematic zones of highly localized strain, known as deformation bands or shear bands, is a usual mode of failure in geomaterials. The occurrence of this pervasive structural mode of deformation in porous rocks has been widely observed both in the field (*e.g.*, [1]) and in laboratory settings (*e.g.*, [2]). A theoretical study of these localized deformation modes through a bifurcation analysis provides a robust framework for understanding the localization conditions [3].

To the authors' knowledge, few theoretical works have systematically examined and compared with experiments the effect of true triaxial conditions on the prediction of strain localization (onset, orientation and volume changes within the band). This is probably due to the scarcity of such experimental data, especially for porous rocks, where laboratory-scale experimental tests are generally carried out on axisymmetric loading paths, very often in compression, sometimes in extension, or more rarely in plane strain compression. In a limited number of studies, experiments have also been performed under true triaxial conditions, allowing the effect of the intermediate principal stress or Lode angle to be fully studied [4–6].

In this work, using experimental data under true triaxial conditions for the Vosges sandstone reported in [7], the deformation bands kinematics, their orientation and dilatancy angle are theoretically predicted for different loading paths [8] and compared to full field experimental measurements.

2. Constitutive model

A non-associated elastoplastic model is developed following experimental observations of the constitutive behavior of the Vosges sandstone. A non-linear mean stress dependence and a van-Eekelen type Lode angle dependence are introduced in the yield surface equation. The model parameters are retrieved from the macroscopic response of the material.

3. Shear band prediction

The deformation band kinematics at the peak stress predicted from the bifurcation analysis using this model is then compared to full-field experimental measurements, in term of shear band orientation and volumetric strain (dilatant or compactant) within the shear band (Figure 1). The Lode angle effect is analyzed, as well as the brittle-ductile transition. The results are compared with alternative and simplified models using the same data set.

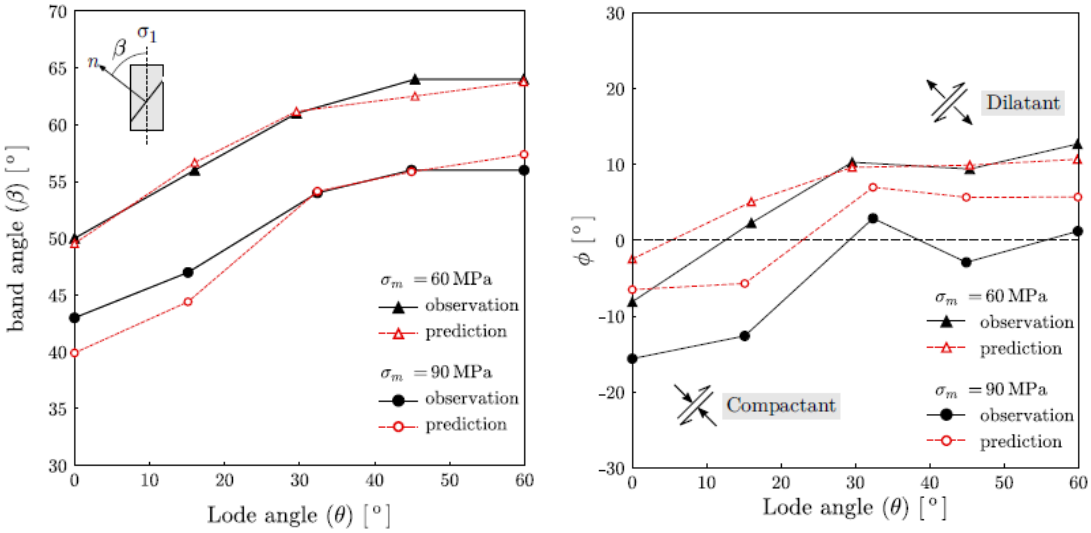

Figure 1. Lode angle impact on the shear band orientation (left) and the band dilatancy angle (right), comparison between predictions and experimental observations for two levels of mean stress (from [8]).

4. References

[1] Aydin, A. & Johnson, A.M. (1978). Development of faults as zones of deformation bands and as slip surfaces in sandstone. *Pure applied Geophys.*, **116**(4-5), 931–942.

[2] Ord, A., Vardoulakis, I. & Kajewski, R. (1991). Shear band formation in Gosford sandstone. *Int. J. Rock Mech. Min. Sci. & Geomech. Abstr.*, **28**(5), 397–409.

[3] Rice, J.R. (1976). The localization of plastic deformation. In: Koiter, W.T. (ed.) *Theoretical and Applied Mechanics*, North-Holland Pub. Comp., Delft, pp. 207–220 (1976). Proc. 14th Int. Cong. Theor. Appl. Mech.

[4] Mogi, K. (2007). *Experimental Rock Mechanics.* Taylor & Francis, London (2007).

[5] Ingraham, M., Issen, K. & Holcomb, D. (2013). Response of Castlegate sandstone to true triaxial states of stress. *J. Geophys. Res. Solid Earth*, **118**(2), 536–552.

[6] Ma, X. & Haimson, B.C. (2016). Failure characteristics of two porous sandstones subjected to true triaxial stresses. *J. Geophys. Res. Solid Earth*, **121**(9), 6477–6498.

[7] Couture, C. & Bésuelle, P. (2022). A true triaxial experimental study on porous Vosges sandstone: from strain localization precursors to failure using full-field measurements. *Int. J. Rock Mech. Mining Sci.*, **153**, 105031. https://doi.org/10.1016/j.ijrmms.2021.105031

[8] Couture, C. & Bésuelle, P. (2023). Three-invariants model and bifurcation analysis of deformation bands for a sandstone subjected to true triaxial loading paths, *Acta Geotech.*, in print.

MESO-SCALE FINITE ELEMENT MODELING OF THE FRACTURE PROCESS ZONE EVOLUTION IN CONCRETE

***Y. Sun*[1], *E. Roubin*[2], *J.B. Colliat*[1] *and J. Shao*[1]**

[1] *Univ. Lille, CNRS, Centrale Lille, UMR 9013 - LaMcube - Laboratoire de Mécanique, Multiphysique, Multi-échelle, F-59000 Lille, France*

[2] *Université Grenoble Alpes, CNRS, Grenoble INP, 3SR, Grenoble F-38000, France*

1. Introduction

The so-called Fracture Process Zone (FPZ) is well-known as a precursor of macroscopic failure for concrete. The formation of a macro-crack is a gradual process starting from a diffused micro-cracking, and also including matrix-aggregates debonding, micro-crack coalescence (cracks branching) and crack closures. Moreover, it is a reasonable assumption that this FPZ extension is partly governed by the underlying random distribution of the material meso-structure. Hence, the meso-scale (millimeter scale) fracture simulation is an efficient tools to better understand this link.

2. Methogology

In this work, we aim to simulate the extension of cracks within the FPZ and to investigate the role of the spatial distribution of heterogeneities. For this purpose, the Enhanced Finite Element Method (E-FEM) model [1] is selected for its simple but efficient way to model heterogeneous meso-structure, and sophisticated representation of complex crack features.

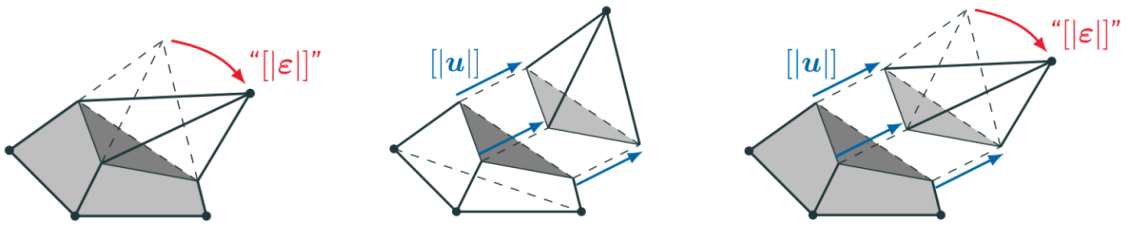

Figure 1. Three elements carrying weak, strong, and both types of discontinuities.

Referring to Fig. 1, the first discontinuity mode is related to the weak discontinuity, which represents a discontinuity in the strain field $[|\varepsilon|]$. The second character is associated with the strong discontinuity, which represents a discontinuity in the displacement field $[|\mathbf{u}|]$. Furthermore, the weak and strong discontinuity are independent and additive. The combination of both forms of discontinuity allows to simulate complex crack features (such as spontaneous crack initiation and multi-branching) while considering crack-aggregate interactions (such as the debonding on the heterogeneity interface).

In existing E-FEM models, several types of cracking modes have been proposed and put in the literature, such as the mode-I traction-opening model and the mode-II sliding-opening model. In this work, considering that the mode-I crack mode is a fairly common choice for modeling FPZ, the mode-I model with the crack opening-closing mechanism [2] is selected.

3. Meso-scale modeling of the FPZ in concrete - Noteched cube

To investigate the crack pattern evolution in the FPZ at the fine-scale, the simulation specimen (see Fig.2) was built based on an experiment which was reported by Koji Otsuka [3]. In that research, experiments were carried out with X-ray and Acoustic emission (AE) techniques to investigate the

FPZ behavior in concrete. The effect of the aggregate size was examined and it was concluded that: as the maximum inclusion size increases, the width of the Fracture Core Zone (FCZ) increases, while the length of the FCZ decreases, see Fig. 3.

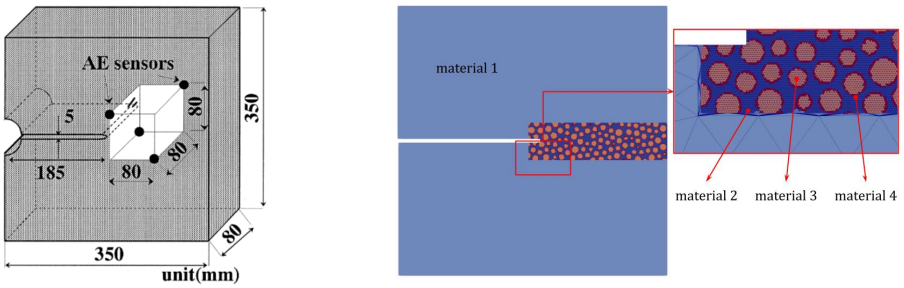

Figure 2. Experimental specimen geometry (left) and the simulation specimen (right).

4. Results and conclusions

The simulation captures many crack patterns in the FPZ, such as diffused micro-cracks, macro-crack coalescence, multi-branching, and crack closures. We also managed to simulate the experimentally observed size effect, i.e., as the inclusion size increases, the FCZ becomes wider and shorter. The most likely explanation for this observation is that a larger inclusion size leads to more tortuous cracks. It is because the crack tends to deviate through inclusions to avoid obstruction. Thus, more circuitous cracks would lead to more energy being dissipated in the crack path, see Fig.3.

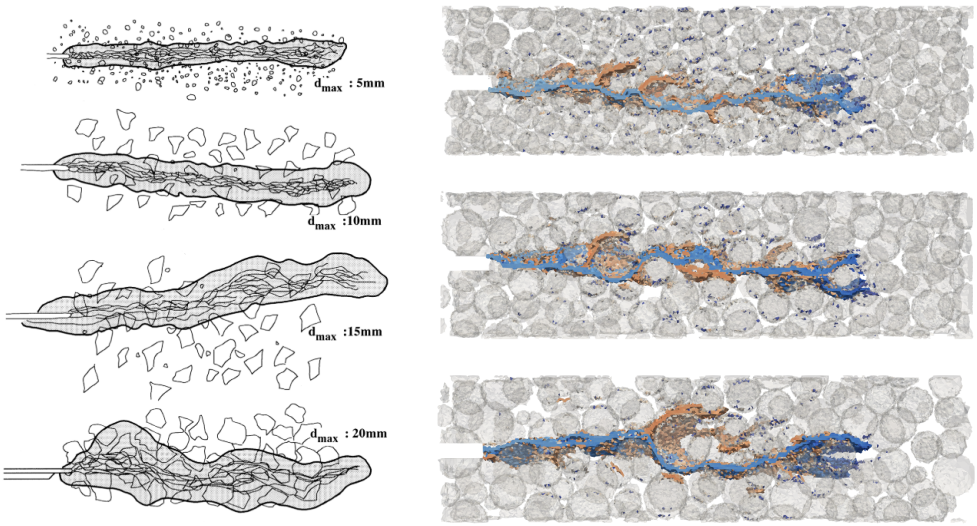

Figure 3. Relationships between the maximum aggregate size (Dmax) and dimension of the FCZ at the peak load in experimental results (left) and numerical results (right).

References

[1] Ortiz, M., Leroy, Y., and Needleman, A. (1987). A finite element method for localized failure analysis. *Computer methods in applied mechanics and engineering*, **61**, 189–214.

[2] Sun, Y., Roubin, E., Shao, J., and Colliat, J.-B. (2021). Strong discontinuity fe analysis for heterogeneous materials: The role of crack closure mechanism. *Computers & Structures*, **251**, 106556.

[3] Otsuka, K. and Date, H. (2000). Fracture process zone in concrete tension specimen. *Engineering Fracture Mechanics*, **65**, 111–131.

NUMERICAL SIMULATION OF SHEAR BAND LOCALIZATION IN CEMENTED GEOMATERIALS WITH NON–LOCAL FINITE DEFORMATION PLASTICITY

***K. Oliynyk*[1,2], *M. O. Ciantia*[1] *and C. Tamagnini*[2]**
[1] *School of Science and Engineering, University of Dundee, Dundee, UK*
[2] *Department of Civil and Environmental Engineering, University of Perugia, Perugia, Italy*

1. Introduction

Strain localization into shear bands is a very common phenomenon observed at different scales, from the laboratory specimen to the soil volumes interacting with typical civil engineering structures. Collapse of geotechnical structures is often characterized by the formation and propagation of zones of localized shear deformations, particularly in presence of soils characterized by strain softening, such as cemented granular materials or structured clays. In such cases, the quantitative prediction of the conditions which lead to localized failure, and the description of the soil/structure system behavior in the post–failure regime are of paramount importance for the assessment of ultimate and serviceability limit states.

In this work, the Particle Finite Element Method (PFEM) is employed to explore the possibility of modeling the occurrence of strain localization and the evolution of the displacement field in the post–localization regime without the pathological mesh dependence typically observed in conventional FEM simulations with classical constitutive models not possessing an internal length scale [1]. The two key points in the proposed numerical approach are the use of a fully non–linear kinematic setup allowing to treat rigorously the high deformations occurring inside the shear bands and the adoption of an isotropic hardening multiplicative plasticity model for bonded geomaterials -– the FD_Milan Model — equipped with non–local hardening laws [2]. The integral nature of the non–local state variables assigns a characteristic length scale ℓ_c to the material, which controls the size of the localized zone.

2. PFEM modeling of plane strain compression tests

A reference specimen with a width B = 1.0 m in the direction x and a height H = 1.8 m in the direction y has been considered in all the simulations. The displacements in direction z are fixed, and the specimen deforms under plane strain conditions, with prescribed vertical displacements on the top and bottom boundaries and prescribed zero normal surface tractions on the lateral boundaries. The self weight of the soil has been ignored by setting to zero the gravity acceleration, so that the actual dimensions of the specimen are not relevant. All the test have been performed under drained conditions, with p_w = 0. A vertical downward displacement u has been imposed at the top boundary in constant steps $\Delta u/H$ = 5.0e-4, up to a final value of u/H = 0.20, while vertical displacements have been fixed at the bottom boundary. The horizontal displacements along the top and bottom boundaries have been kept fixed, to simulate perfectly rough end platens. The material constants adopted in the simulations, taken from Oliynyk et al. [2], are representative of a weak calcarenite rock. In all the tests, the initial values of the preconsolidation pressure P_s and of the bond strength P_t have been assumed equal to -300 kPa and -200 kPa, respectively (in the sign convention of continuum mechanics).

3. Convergence study in the context of adaptive remeshing

Typically, convergence studies aimed at evaluating the effectiveness of a regularization method are performed by uniformly reducing the element size over the entire domain, see, e.g., [3]. In this

work, the convergence study is addressed in PFEM simulations with non-uniform, adaptive discretizations, exploring the convergence of the solution as the minimum element size h_{min} of the discretization is reduced. In particular, the ratio h_{crit}/l_c has been varied in the range [0.07,0.50]. The reason for this choice is that adaptive remeshing is an essential component of PFEM algorithmic strategy as well as an essential feature to achieve a high computational efficiency in the solution of BVPs of practical interest.

Fig. 1a shows the patterns of strain localization obtained for the two smallest values of the ratio between the critical element size h_{crit} and the characteristic length ℓ_c. The contour maps show the accumulated plastic deviatoric strain E_s^p at four different time stations. The comparison between the maps on the upper and lower rows indicate that the two numerical solutions are almost identical in terms of geometry and thickness of the two conjugate shear bands forming already at $u/H = 0.05$.

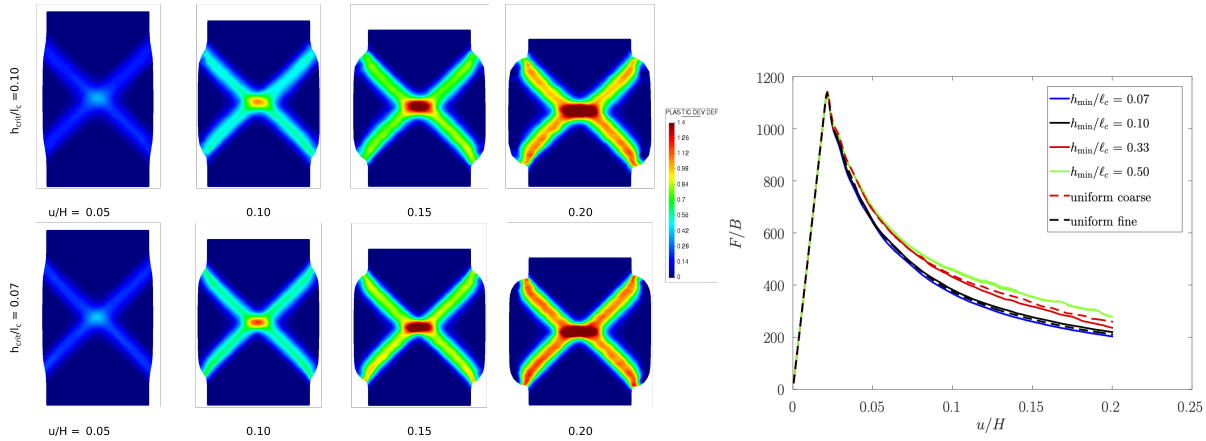

Figure 1. Biaxial tests at different h_{crit}/ℓ_c values: a) contour maps of accumulated plastic deviatoric strain at four different time stations; b) load–displacement curves.

This is reflected in the load F/B *vs*. normalized displacement u/H curves of Fig. 1b. As expected, for a highly cemented material loaded with no confining stress, the load–displacement response is brittle, with a strong strength reduction after the peak load is reached. In the post–peak regime, the solutions are significantly affected by the adopted minimum element size. As h_{crit} reduces and become sufficiently smaller than the band thickness, the solutions converge to a unique load–displacement curve.

References

[1] Vardoulakis, I. and Sulem, J. (1995). *Bifurcation analysis in geomechanics*. CRC Press.

[2] Oliynyk, K., Ciantia, M. O., and Tamagnini, C. (2021). A finite deformation multiplicative plasticity model with non–local hardening for bonded geomaterials. *CG*, **137**, 104209.

[3] Mánica, M. A., Gens, A., Vaunat, J., and Ruiz, D. F. (2018). Nonlocal plasticity modelling of strain localisation in stiff clays. *CG*, **103**, 138–150.

3. Modelling of thermo-hydro-mechanical coupling and other transient problems

FROM MENISCUS INSTABILITY TO DRYING - CRACKING OF SOILS: A MULTI-PHYSICS & MULTI-SCALE FRAMEWORK

F.I. Wu[1], R.Y. Chen[1], W. Lindqwister[1], B. Mielniczuk[2], M. Veveakis[1] and T. Hueckel[1]
[1] Duke University, Durham, NC, USA
[2] BJM, St.-Laurent Le-Minier, France

1. General

Cracking of drying soils and muds is especially critical when they are used for barriers against undesired transport of water and contaminants, including nuclear or hazardous ones or against flooding of excavations. Heat generated by waste often intensifies evaporation accelerating the drying-cracking, as demonstrated in some in-situ tests. This study presents test results of soil drying-cracking starting from a grain and a sub-grain scale, up to macro-scale.

2. Phenomenology

Drying-cracking appears to be a complex array of physical, mechanical and hydraulic processes, which have been tested and quantified at multiple-scales in terms of properties and variables that need to be communicated between scales. Drying process can be broken down into the following phases: free shrinkage; air entry/desaturation onset; constrained shrinkage/internal stress buildup; drying-cracking onset; crack propagation/networking; shrinkage limit. The phases may occur either alone, or sequentially, or by zones. They were investigated via experiments at different scales chosen for the phenomena and measurable variables driven by respective conceptual multi-physics models [1, 2, 3, 4].

3. Results

An important observation regarding cracks at macro-scale is the role of boundaries and kinematic constraints that may limit free material shrinking during drying. This is observed for instance on samples drying on a Teflon substrate with no external stress in reaction to any sort of kinematic constraints or frictional interaction are present. Instead, drying on different substrates constraining the shrinkage induces total stress caused by the reaction forces at the constraint location (e.g. tangential forces at the contact with a rough substrate) [1]. However, due to evaporation flux induced water flow and hence a suction gradient and shrinkage, a corresponding effective stress arises which, when reaching a threshold, induces local damage or cracking, or any type of instability. The trickiest issue is to understand and represent the nature of constraints, including all sorts of inhomogeneities and moving boundary conditions.

As far as drying-cracking onset is concerned, there are several ways of looking at it, depending on the scale. Most importantly, at macroscale cracks appear in the material that is still completely wet, i.e. in a saturated state, very soon after air entry. Hence, we follow an earlier hypothesis [1, 2, 4, 5] that air entry constitutes a perturbation around which a total stress concentration arises leading to a mode I crack onset. Secondly, tensile cracks seen from an image correlation deduced strain field as strain singularities, are oriented perpendicularly to the direction of constraints. Thus, we seek a singularity of a solution for a macro-scale elasto-visco-plastic effective stress state developing during evaporation induced flow. Such a singularity is controlled by a competition between seepage force rate controlled by evaporation rate and visco-plasticity rate [6] as seen on Fig. 1 for a drying 1-D slab. At the grain scale, we study local conditions for air entry, or Haines jump, which occurs at inter-grain throat where the rate of suction becomes

incompatible with geometry-controlled contact force rate yielding an instant growth of inertia forces, acceleration and a meniscus Gibbs interface-instability, Fig. 2. The instability provides a local energy excess resulting in a local meniscus jump and an adhesion discontinuity, which may be seen as a local perturbation at a larger scale leading to the onset of a fracture.

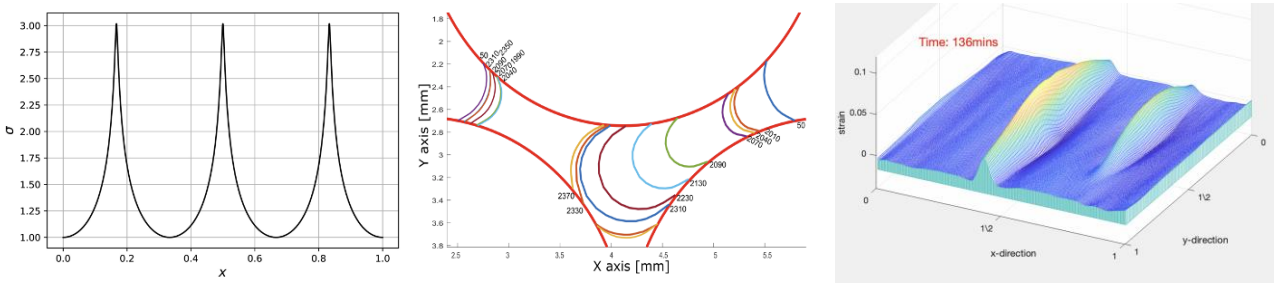

Fig.1 (left). Solution for an effective axial stress during 1-D desiccation of a visco-plastic bar for the moment of appearance of a singularity at three equi-distanced locations [6]. Fig. 2. (ctr.) Evolution in time (in seconds) of two menisci of a water volume housed between three glass cylinders. On the RHS between 2070s and 2090s the meniscus jumps over 1.3 of its total travel distance. Fig.3(right) Strain localization in a constrained slab drying test [7].

4. Conclusions

Experiments on meso-scale assemblies suggest that nearly half of the total displacement of menisci occurs via slow motion at a evaporation rate, while the other half via instantaneous jumps. Thus overall, meniscus moves at a slow rate. That translates at a macroscale into a crack propagation at a rate close to that of evaporation, rather that of brittle cracks traveling at the rate of elastic waves, several orders of magnitude higher. An open question remains about the mesoscale modeling and upscaling of the moving drying front for macro-scale models.

5. References

[1] Peron H., Hueckel T., Laloui L., Hu L.B., (2009a) Fundamentals of desiccation cracking of fine grained soils: Experimental characterisation and mechanism identification, *Can. Geotech. J.*, 46 (10), 1177-1201

[2] Peron H., Laloui L., Hueckel T., Hu L.B., (2009b) Desiccation cracking of soils, *Eur. J. Environ. Civil Engrg.*, 13 (7–8), pp. 869-888

[3] Hu L.B., Peron H., Laloui L., Hueckel T. (2013) Desiccation shrinkage of soils: multiphysics mechanisms and a microstructural model, *Int. J. Num. Anal. Meth. Geomech.*, 37, 1761–81

[4] Hueckel, T., Mielniczuk B., Hu L.B. and El-Youssoufi M.S. (2014) A three-scale criterion for drying soils, *Acta Geophysica*, 62, 5, 1049-1059; DOI: 10.2478/s11600-014-0214-9

[5] Scherer G.W. (1992) Crack-tip stress in gels, *J. Non-Cryst. Solids* **144**, 210-216, DOI: 10.1016/S0022-3093(05)80402-8.

[6] Veveakis, M. Poulet, T. (2021) A note on the instability and pattern formation of shrinkage cracks in viscoplastic soils, *Geomechanics for Energy and the Environment*, 25,100198, https://doi.org/10.1016/j.gete.2020.100198.

[7] Chen, R., Lindqwister, W., Hueckel, T., Veveakis, M. (2023). An Experimental Study on Silt Desiccation Cracking with Different Basal Constraints and Various Humidity in: Pasternak, E., Dyskin, A. (ed.) *Multiscale Proc. Instab., Deform. Fract. in Geomaterials.* IWBDG 2022

ON THE EFFECTIVE PERMEABILITY OF HETEROGENEOUS ROCKS

A.P.S. Selvadurai
McGill University, Canada

1. General

Heterogeneity in the Thermo-Hydro-Mechanical (THM) properties of naturally occurring rocks needs to be considered when samples are tested at scales where the spatial distribution of the heterogeneities can influence the estimation and interpretation of THM properties. Permeability is a key parameter in a THM model; for low permeability rocks, in particular, the influence of the small sample size required to minimize the time to saturate a sample and perform laboratory tests, needs to be reconciled with the requirements of a large sample size that can capture the spatial distribution of heterogeneity in terms of a representative volume element.

2. Background

The rock under investigation is the Cobourg limestone found in southeastern Ontario within the Paleozoic sedimentary sequence that rests on a Pre-Cambrian granitic basement rock of the Canadian Shield. Interest in this low permeability limestone stems from its suitability as a host rock for a Deep Geologic Repository (DGR) for storing low- and intermediate-level radioactive waste, in proposed sites located near the eastern shores of Lake Huron [1-4]. The Cobourg limestone is overlain by the Upper Ordovician-age siltstone and gray shale extending to a thickness of approximately 200 m and underlain by argillaceous limestone and gray shale, approximately 150 m thick. A dominant visual feature of the Cobourg limestone is the heterogeneity of the fabric, consisting of the *lighter* nodular regions of calcite and dolomite separated by *darker* argillaceous partings of a similar composition but with quartz and a low clay content (Figure 1). In this research, attention is first focused on mapping the spatial distribution of the *lighter* and *darker* species of the Cobourg limestone (Figure 1) by dissecting a cuboid measuring 80 mm x 120 mm x 300 mm into thick plate samples measuring 80 mm x 120 mm x 8 mm with a separation of 8 mm. The photographic images of the top and bottom surfaces of the ten plate sections are combined with digital imaging techniques to identify the surface features of the *lighter* and *darker* regions of each plate sample (Figure 1). The images are used to create the plausible through-thickness fabric distributions using either a *direct surface image extrusion* procedure or a computer-aided interpolation technique (Figure 2).

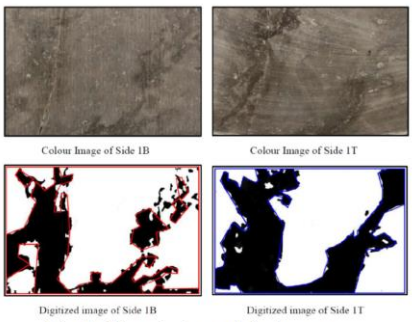

Fig 1. The photographic images

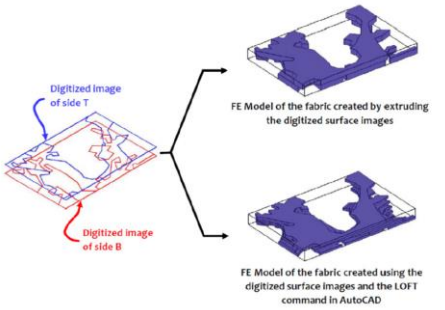

Fig 2. Digitized images and the FE models

3. Theoretical Estimates and Computational Estimates of Effective Permeability

Modelling the Cobourg limestone as a statistically homogeneous isotropic medium and provided the phasic permeabilities in the lighter (LR) and darker (DR) regions are non-zero, the effective permeability (K^*) can be bounded by the *Voigt* [V] and *Reuss* [R] estimates [5,6] (consistent with the Wiener bounds [7]) in (1) (and the Hill [8] estimate, which is the average of the V&R estimates) in the form

$$\left[\sum_{i=1}^{m}\left(\frac{V_i}{K_i}\right)\right]^{-1} < K^* < \sum_{i=1}^{m} K_i V_i \quad ; \qquad i = \mathrm{LR}, \mathrm{DR} \tag{1}$$

where V_i are the volume fractions and K_i are the permeabilities. Considering the permeability estimates for the *lighter* and *darker* regions [1,2] and the volume fractions $V_{DR} \simeq 0.54$; $V_{LR} \simeq 0.46$, the result (1) and the Hill average give

$$1.235 < (K^*/10^{-19}\mathrm{m}^2) < 4.605 \quad ; \quad (K^*/10^{-19}\mathrm{m}^2)_{\mathrm{Hill}} \simeq 2.920 \tag{2}$$

The bounds can be improved by considering the theoretical developments proposed by Hashin and Shtrikman [9] based on variational approaches, and, for a two-phase system (i.e. designated by the *lighter* (LR) and *darker* (DR) phases), take the form

$$K_{\mathrm{LR}} + \left(V_{\mathrm{DR}} \Big/ \left\{ \frac{1}{(K_{\mathrm{DR}} - K_{\mathrm{LR}})} + \frac{V_{\mathrm{LR}}}{3K_{\mathrm{LR}}} \right\} \right) \le K^* \le K_{\mathrm{DR}} + \left(V_{\mathrm{LR}} \Big/ \left\{ \frac{1}{(K_{\mathrm{LR}} - K_{\mathrm{DR}})} + \frac{V_{\mathrm{DR}}}{3K_{\mathrm{DR}}} \right\} \right) \quad \text{or} \quad 2.031 \le \left(K^*/10^{-19}\mathrm{m}^2 \right) \le 3.929 \tag{3}$$

The computational modelling of the potential flow problem is performed using the COMSOL™ finite element code and the domains are modelled using tetrahedral elements. The number of elements for ***each plate*** are in excess of 150,000 for the *extruded geometry* and more than 210,000 elements for the *LOFT command internal fabric reconstruction*. The number of DoF is generally greater than 280,000. This computational approach was used to estimate the permeabilities of the ten adjacent plates from the Cobourg limestone sample. The permeability normal to the larger surface area of the slab is denoted by K_z and the permeabilities directions aligned with the edges of a slab are denoted by K_x and K_y.

For the ***Extruded Geometry***

$$K_x^{*Ext} \simeq 2.860\times10^{-19}\mathrm{m}^2 \quad ; \quad K_y^{*Ext} \simeq 2.388\times10^{-19}\mathrm{m}^2 \quad ; \quad K_z^{*Ext} \simeq 2.049\times10^{-19}\mathrm{m}^2 \tag{4}$$

For the ***Morphed Geometry***

$$K_x^{*Ext} \simeq 2.047\times10^{-19}\mathrm{m}^2 \quad ; \quad K_y^{*Ext} \simeq 2.370\times10^{-19}\mathrm{m}^2 \quad ; \quad K_z^{*Ext} \simeq 2.409\times10^{-19}\mathrm{m}^2 \tag{5}$$

Following [10,11], we can define the ***Geometric Mean*** of the permeability as follows:

$$\begin{aligned} K_{GM}^{Extr} &= \sqrt[3]{(K_z^{*Extr})(K_x^{*Extr})(K_y^{*Extr})} = 2.410\times10^{-19}\mathrm{m}^2 \\ K_{GM}^{Morph} &= \sqrt[3]{(K_z^{*Morph})(K_x^{*Morph})(K_y^{*Morph})} = 2.266\times10^{-19}\mathrm{m}^2 \end{aligned} \tag{6}$$

4. Concluding Remarks

This research discusses the obstacles encountered in estimating the fluid transport characteristics of very low permeability rocks that are also heterogeneous. The drawbacks can be overcome by appeal to theoretical estimates based on multi-phasic approaches complemented by computational approaches that can utilize the mapped heterogeneous fabric. The studies provide comparable estimates between the *theoretical* and *computational* estimates.

5. References

[1] Selvadurai, A.P.S. (2019) A multi-phasic perspective of the intact permeability of the heterogeneous argillaceous Cobourg limestone, *Scientific Reports*, **9**: 17388,

[2] Selvadurai, A.P.S. and Głowacki, A. (2018) Estimates for the local permeability of the Cobourg limestone, *J. Rock Mech. Geotech. Engng*, **10**: 1009-1019.

[3] Selvadurai, A.P.S. and Najari, M.(2017) The thermo-hydro-mechanical behaviour of the argillaceous Cobourg Limestone, *J. Geophys Res., Solid Earth*, **122**,

[4] Selvadurai, A.P.S**.** and Najari, M. (2016) Isothermal permeability of the argillaceous Cobourg Limestone, *Oil and Gas Sci. Tech., Special Issue on Low Perm Geomaterials*, **71**, 53-69.

[5] Voigt, W. (1928) *Lehrbuch der Kristallphysik*, B.G. Teubner, Leipzig.

[6] Reuss, A. (1929) Berechnung der Fließgrenze von Mischkristallen auf Grund der Plastizitätsbedingung für Einkristalle. *J. Appl. Math. Mech*, 9, 49–58.

[7] Wiener, O. 1912 Die Theorie des Mischkörpers für das Feld des stationaären Strömung. Erste Abhandlung die Mittelswertesätsze für Kraft, Polarisation und Energie'. *Abh. Math.-Physischen Klasse Königl. Sächsh Gesell. Wissen* **32**, 509–604.

[8] Hill, R. (1952) The elastic behaviour of a crystalline aggregate, *Proc. Phys. Soc*., **65**, 349-354.

[9] Hashin, Z. and Shtrikman, S. (1962) A variational approach to the theory of effective magnetic permeability of multi-phase materials, *J. Appl. Phys*, **33**, 3125-3131.

[10]Selvadurai, A.P.S. and Selvadurai, P.A. (2010) Surface permeability tests: Experiments and modelling for estimating effective permeability, *Proc Roy Soc, Math Phys Sci Series A*, **466**: 2819-2846.

[11]Selvadurai. P.A. and Selvadurai, A.P.S.(2014) On the effective permeability of a heterogeneous porous medium: the role of the geometric mean, *Philosophical Magazine*, **94**: 2318-2338.

ON COUPLED HYDROMECHANICAL ANALYSIS OF CRYSTALLINE AND ARGILLACEOUS ROCKS

S. Pietruszczak and A.A. Jameei
McMaster University, Hamilton, Ont., Canada

1. General

This research is focused on the numerical analysis of hydro-mechanical response of different rock formations. Two main aspects are addressed. The first one deals with modelling of coupled behaviour of crystalline rocks that contain multiple pre-existing fractures. An enhanced form of Darcy's law is established based on volume averaging of the fluid pressure gradient within the referential volume adjacent to a macrocrack. This is supplemented by a constitutive stress-strain relation in rate form that incorporates an embedded discontinuity approach. Some illustrative numerical examples are provided examining the hydro-mechanical behaviour of Lac du Bonnet granite in the presence of a discrete fracture network. The second topic deals with description of anisotropy in sedimentary formations that have a strongly heterogeneous fabric. In this case, a specific measure of microstructure, based on stereology, is employed in order to account for the directional dependence of strength properties at the macroscale.

2. Modeling of hydro-mechanical response of sparsely fractured crystalline rocks

The formulation presented here incorporates an averaging of the field operators within the domain containing a discontinuity. Such an approach does not require any additional degrees of freedom to account for the presence of discontinuities, which significantly improves the computational efficiency. In order to define the hydraulic properties, a domain $\Delta\Omega$, intercepted by a fractured region of thickness t_d and the surface area $\Delta\Gamma_d$, is considered across which the superficial velocity of fluid $\mathbf{v}_f$ is discontinuous. Imposing the discontinuity in fluid pressure p and invoking some constraints for the kinematics of flow, the following enhanced form of Darcy's law has been obtained (cf. ref.[1])

$$\mathbf{v}_f = \frac{1}{\rho_f g}\bar{\mathbf{K}}\mathbf{h} = \frac{1}{\rho_f g}\bar{\mathbf{K}}\,(-\boldsymbol{\nabla}_{\mathbf{x}} p + \rho_f\,\mathbf{g}) \tag{1}$$

where $\bar{\mathbf{K}}$ is an equivalent hydraulic conductivity tensor defined as

$$\bar{\mathbf{K}} = \left[(1-\mu)\mathbf{K}^{(1)} + \mu\mathbf{K}^{(2)}\boldsymbol{\mathcal{C}}\right]\left[\mathbf{1} + \mu(\boldsymbol{\mathcal{C}} - \mathbf{1})\right]^{-1}; \qquad \mu = \chi t_d, \quad \chi = \Delta\Gamma_d/\Delta\Omega \tag{2}$$

In the equations above, ρ_f is the fluid's intrinsic density, g is the acceleration due to gravity and $\mathbf{K}^{(1)}$, $\mathbf{K}^{(2)}$ are the permeability tensors in the intact and fractured regions, respectively. Moreover, the operator $\boldsymbol{\mathcal{C}}$ defines the coefficients of constraints and its representation is provided in ref. [1].

The equivalent hydraulic conductivity $\bar{\mathbf{K}}$ is a *symmetric* second-order tensor whose components are a function of hydraulic properties of constituents (viz. intact material and fractured region) and an internal scale parameter μ. The latter is defined explicitly in eq.(2) and represents the volume fraction of the fractured zone contained within the referential domain. The respective field equations are derived following the general form of balance equations in interacting continua. The conventional finite element method is then employed for the spatial discretization and an implicit integration scheme is used for the temporal discretization.

The *mechanical* analysis incorporates an enhanced embedded discontinuity approach, which is conceptually similar to that used for specification of equivalent hydraulic conductivity. The framework employs a scale parameter χ, eq.(2), related to geometry of fractures and enables a discrete tracing of the propagation of new cracks. The constitutive relation takes the form

$$\dot{\boldsymbol{\sigma}}' = \bar{\mathfrak{D}} : \mathfrak{D} : \dot{\boldsymbol{\varepsilon}} \; ; \qquad \bar{\mathfrak{D}} = \mathcal{I} - \chi \mathfrak{D} : [\mathbf{n} \otimes (\mathcal{k} + \chi \mathbf{n} \cdot \mathfrak{D} \cdot \mathbf{n})^{-1} \otimes \mathbf{n}] \tag{3}$$

where $\boldsymbol{\sigma}'$ is the effective stress tensor, $\mathfrak{D}$ is the constitutive fourth-order tensor which defines the properties of the intact material, **n** denotes the unit normal to the fracture, $\mathcal{k}$ is the stiffness operator relating the velocity discontinuity to the effective traction rate, and $\mathcal{I}$ is an isotropic fourth-order identity tensor.

The formulation is illustrated by a numerical study involving plane strain compression of sparsely fractured dry and fully saturated samples of Lac du Bonnet granite. The finite element framework employed here incorporates a coupling between the equivalent hydraulic and mechanical properties in the weak statement of the governing field equations. Evidently, the continuing deformation affects the fracture aperture which, in turn, influences the generation of fluid pressure. The simulations take into account the pre-existing fractures and the onset and propagation of new macrockraks. The notion of the loss of stability in a saturated porous medium is also addressed by examining the evolution of the second rate of internal work.

3. Description of anisotropic properties of argillaceous rock formations

The specific type of argillaceous rock considered here is the Cobourg limestone. This rock is characterized by a heterogeneous fabric that consists of light gray calcite nodular regions interspersed with dark gray calcite-dolomite-quartz partings containing a clay component. There is also visual evidence of nominal planes of stratification. Given this complex structural arrangement, the correlation between the microstructure and the mechanical properties is a very challenging issue.

It is generally believed that anisotropy is due to stratification resulting from the sedimentation process. Heterogeneity, on the other hand, originates from the interspersed fabric (cf. [2]). The quantification of heterogeneity requires an explicit tensorial measure that includes an orientation dependent information. The specific fabric measure employed here is based on stereology. The latter offers efficient techniques for extracting microstructural data from measurements made on a set of two-dimensional planar sections within the Representative Elementary Volume of the material by sampling in a statistical sense. The descriptor used here is the 'mean intercept length', which defines the mean length of the inclusions along a set of lineal probes of a given orientation. This fabric measure is incorporated in the description of strength and deformation properties of Cobourg limestone [3]. The macroscopic framework employs the microstructure tensor approach [4], in which the material functions are enhanced to incorporate the dependence of strength properties on the volume fraction of the inclusions.

The constitutive relation is formulated within the framework of elasto-plasticity. A procedure for identification of approximation coefficients describing the spatial distribution of anisotropy parameters is developed and the formulation is verified using the experimental data available in the literature.

4. References

[1] Jameei A.A., Pietruszczak S. (2020). Embedded discontinuity approach for coupled hydro-mechanical analysis of fractured porous media, *Int. Journ. Num. Anal. Meth. Geomech,* **44**, 1880-1902.

[2] A.P.S. Selvadurai, Najari M. (2017). The thermo-hydro-mechanical behaviour of the argillaceous Cobourg limestone. *Journ. Geophys. Res.: Solid Earth.* **122**, 4157-4171.

[3] Pietruszczak S., Pakdel P. (2022). On the mechanical anisotropy of argillaceous Cobourg limestone: fabric tensor approach, *Intern. Journ. Rock Mech. Mining Sci*., **150**, 104953: 1-9.

[4] S. Pietruszczak, Z. Mroz (2001). On failure criteria for anisotropic cohesive-frictional materials. *Int. Journ. Num. Anal. Meth. Geomech.* **25**, 509-524.

NUMERICAL ASSESSMENT OF THE INFLUENCE OF BIOGENIC GAS ON THE COUPLED HYDRO-MECHANICAL RESPONSE OF ORGANIC SOILS

C. Jommi[1,2], S. Muraro[1], W.J. de Wolf[1] and M. Xu[1]
[1] Delft University of Technology, Delft, the Netherlands
[2] Politecnico di Milano, Milano, Italy

1. Motivation

In the Netherlands, about 3500 km of dykes are made of peat or lay on shallow layers of peats and organic clays. These highly organic soils are prone to degradation at increasing temperature and water deficit, which comes together with gas production, mainly CO_2 or CH_4, depending on oxygen availability. A comprehensive experimental, theoretical and numerical effort has been undertaken at TU Delft to analyse the current state of embankments and predict their response over future scenarios of increasing climatic impact. A part of this study concerns the development of theoretical and numerical models able to improve our understanding of the consequences of entrapped gas pressure build-up in embankments. The models will allow quantifying the influence of gas pressure on the stability of dykes among the factors which may hinder the safety of the current water defence infrastructure.

2. Experimental evidence

Evidence of gas entrapment in the shallow organic layers below dykes in the Netherlands dates back decades [1, 2]. Below the water table, dissolved methane and hydrogen sulphide saturate the pore fluid as a result of the decomposition of the organic matter and can be exsolved by temperature increase, water table drop or total stress reduction. Gas generation, exsolution and expansion into an initially saturated matrix of peat (Fig. 1) may eventually soften the matrix and reduce its strength as recently discussed in ref. [3]. However, even before any softening occurs in the matrix, gas overpressure decreases the average "effective" stress acting on the soil skeleton, hence, reducing the available resistance on potential failure surfaces and undermining the stability of the embankment. Results from preliminary triaxial tests performed on samples where gas was generated by undrained unloading after flushing with CO_2 supersaturated water (Fig. 1), were interpreted with a simple non-linear elastic model in ref. [4]. The interpretation is based on the hypothesis that the water retention curve upon drying of a saturated sample of peat may equally represent the equilibrium states of the peat matrix under exsolving gas (Fig. 2). The comparison between numerical results and experimental data is satisfactory in the simulation of the fluid pressure- volumetric strain history of the tested samples.

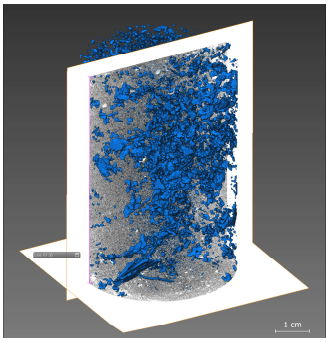

Figure 1. X-ray CT scan of a peat sample after gas generation

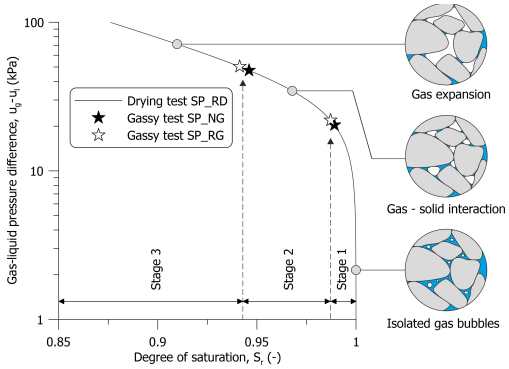

Figure 2. Projection of gas exsolution stages on the retention curve over drying

3. Numerical results

Based on the previous results, numerical models were set up to analyse simple boundary value problems, representative of various field cases. A series of fully coupled two-phase flow with hydro-mechanical coupling numerical analyses were performed accounting for the presence of gas in the soil layer to replicate field observations. The analyses were run with CODE_BRIGHT [5], calibrating simple models with available laboratory data for the various soils.

Figure 3 shows the results of a simple simulation of gas generation in peat under a less pervious silty clay cap layer. The stratigraphy replicates that of a real dyke, where water overpressure peaks between 15 kPa and 25 kPa were measured in the clay layer over time, which raised some concerns on the reliability of the measurements. The numerical results show that the clay layer above the peat may experience peaks of overpressure above 20 kPa for an increase in the gas volume as low as 1%, if the saturated hydraulic conductivity is as low as $k = 10^{-9}$ m/s.

In Figure 4, the contours of horizontal displacement due to gas expansion in the peat layer are plotted. The amount of initial gas was 10% in volume. Gas expansion and contraction with variable atmospheric conditions generate cyclic horizontal displacements, similar to the ones recorded over one year by an inclinometer installed in the slope of a regional dyke at the Leendert de Boerspolder in the Netherlands. The results of the analysis captured the trend of the seasonal displacements and suggested that temperature variations should be accounted for besides atmospheric pressure variations to match the order of magnitude of the recorded data. Advanced models for the Dutch soft soils under unsaturated conditions are being implemented to improve the quantitative predictions.

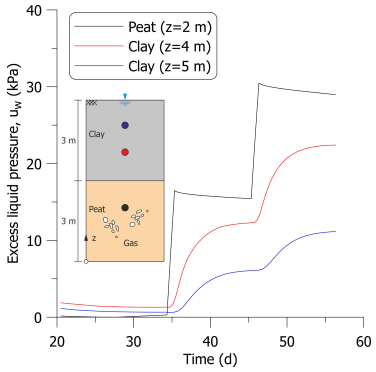

Figure 3. Water overpressure in the cap clay layer due to gas entrapment in the basal peat

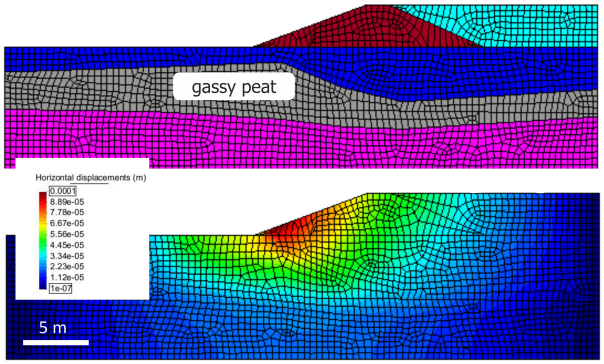

Figure 4. Displacements following gas exsolution in the peat foundation layer of a dyke

4. References

[1] Vonk, B. F., Den Haan, E., Termaat, R. & Edil, T. B. (1994). Some aspects of the engineering practice regarding peat in small polders. In *Advances in understanding and modelling mechanical behaviour of peat* (Den Haan et al. eds), 389–402, Delft: Balkema.

[2] den Haan, E. J. & Kruse, G. A. M. (2007). Characterisation and engineering properties of Dutch peats. *Proc. 2nd Int. Workshop of Characterisation and Engineering Properties of Natural Soils*, (Tan et al. eds), 29: 2101–2133, Singapore: Taylor & Francis Group.

[3] Jommi, C., Muraro, S., Trivellato, E. & Zwanenburg, C. (2019). Experimental results on the influence of gas on the mechanical response of peats. *Géotechnique* 69(9), 753–766.

[4] Zhao, H., Muraro, S. & Jommi, C. (2020). "Gas exsolution and gas invasion in peat: towards a comprehensive modelling framework." *Géotechnique Letters* 10(3): 461-467.

[5] Olivella, S., Gens, A., Carrera, J., Alonso. E. E. (1996). Numerical formulation for a simulator (CODE_BRIGHT) for the coupled analysis of saline media, *Eng. Computation* 13(7), 87-112.

NUMERICAL ANALYSES INCORPORATING AN INTERFACE ELEMENT FOR HYDRO-CHEMO-MECHANICAL COUPLING

F. Ghalamzan Esfahani, A. Gajo
University of Trento, Trento, Italy

1. Introduction

Interface behavior plays a key role in various geotechnical engineering problems. In particular, in the stability analysis of clayey slopes, the thin slip surface can be considered as an interface within the soil mass [1]. The zero-thickness Goodman's element [2] is frequently used for simulating the mechanical behaviour of interface regions. In a soil mass however, water can flow in the interface region and affect the mechanical behaviour of the interface [3]. Moreover, when a salt is dissolved in the pore fluid, salt can diffuse through the interface region and affect the mechanical response of the interface in active clays [4]. Besides, the interface may behave as a barrier to the fluxes of water and salt in its normal direction, thus preventing the flow of fluid and the diffusion of salt or may enhance the hydraulic conductivity in the tangential direction of the interface [3,5]. As a result, when modeling interfaces in soil, the fluxes of water and salt must generally be considered in addition to the purely mechanical response of the solid skeleton.

This paper presents an interface element that accounts for the hydro-chemo-mechanical coupling in the interface region. This element is an extension of the modified Goodman's element [6]. The flow of water and diffusion of salt are considered in the transversal and longitudinal directions of the interface region.

2. Methodology

We assume that the interface element is composed of a solid and a fluid phase and can be simulated with a modified Goodman's element with a non-zero thickness for the fluxes of water and salt (Fig.1). For the solid phase, the interface element consists of two surfaces with six nodes (three nodes on each surface) that can move with respect to each other (Fig.1). The fluid phase is composed of pore water and dissolved salt and is represented by 4 nodes (two nodes on each surface). The hydro-chemo-mechanical coupling is considered in this interface element because a change of salt concentration affects the friction angle of the soil [4]. The normal and shear effective stresses ($\boldsymbol{\sigma}' = [\sigma_n' \quad \sigma_s']^T$) are conjugated to the relative displacement of the interface element in the normal and transversal directions ($\delta\boldsymbol{\epsilon} = [\delta\epsilon_n \quad \delta\epsilon_s]^T$). We have considered the following balance equations: 1) the momentum balance for the whole medium, 2) the mass balance of pore fluid, 3) the mass balance of diffusing salt. Water flow and salt diffusion are considered in both longitudinal and transversal directions, while the hydro-mechanical coupling is considered only in the direction normal to the interface element. The proposed interface element has been implemented in a user-defined subroutine (UEL) of ABAQUS.

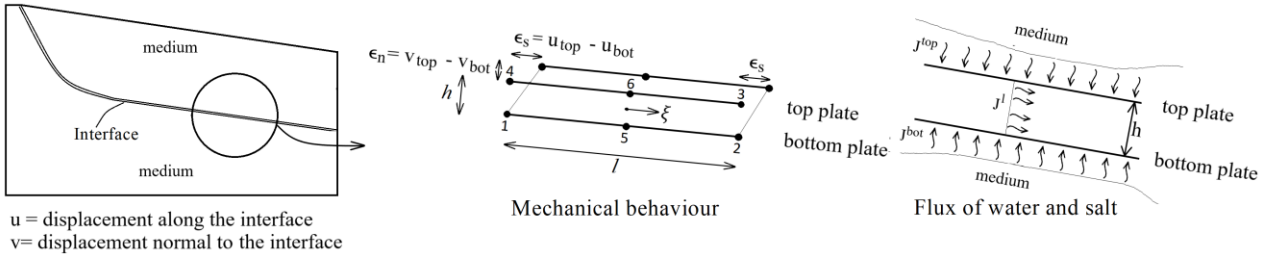

Fig 1. Mechanical behavior and fluxes of water and salt in the interface element

3. Results

Two numerical tests are described below for the sake of presenting the typical interface responses with regards to salt diffusion.

In order to examine salt diffusion in the longitudinal direction of the interface element, a 100 mm high column has been analyzed (Fig. 2a). The displacement and pore pressure of all nodes have been constrained. The salt concentration was increased from distilled water to 30 kg/m^3 at the top of the model. The longitudinal diffusion coefficient of the interface was assumed to be equal to 10^{-7} m^2/s. Figure 2a shows that salt progressively diffuses from the external boundary into the interface elements.

In order to examine the effects of transverse salt diffusion through the interface element, a soil column with an interface at the middle height has been simulated (Fig.2b). The diffusion coefficient of soil mass was assumed to be equal to 10^{-7} m^2/s, whereas different values of the diffusion coefficient (D_t) of the interface were examined (namely 10^{-7} m^2/s, 10^{-8} m^2/s, and 10^{-9} m^2/s). Figure 2b shows the distribution of salt concentration in the soil column for the different values of D_t when stationary conditions are reached. It can be observed that there is a salt concentration drop at the middle of the soil column, where the interface is positioned. The amount of salt concentration drop increases with the decrease of the diffusion coefficient of the interface D_t. When the diffusion coefficient D_t is equal to the diffusion coefficient of the soil mass, the salt concentration distribution is continuous, as expected.

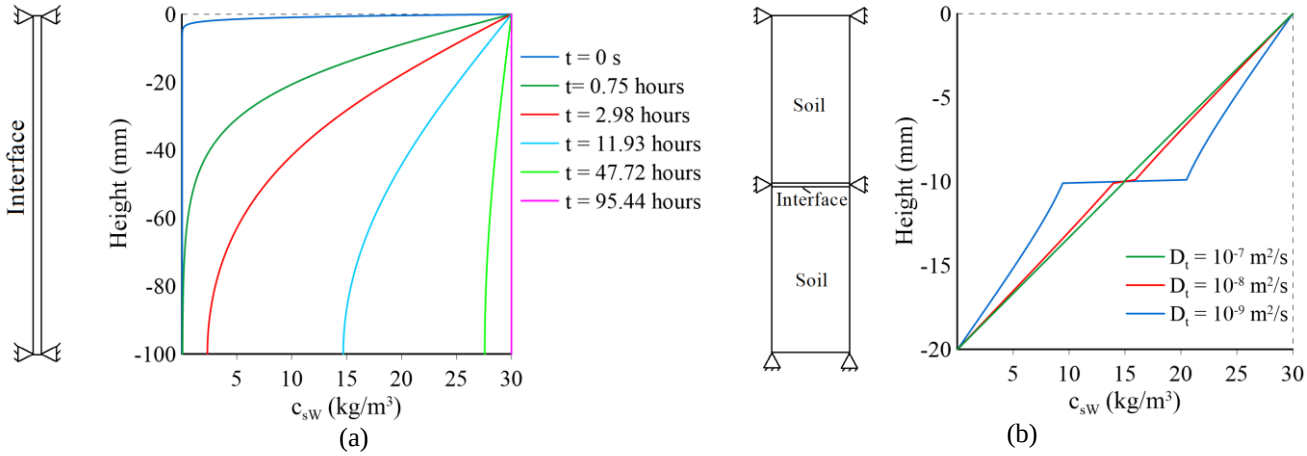

Fig 2. Distribution of salt concentration a) in the longitudinal direction of the interface elements, b) in the normal direction of interface element

5. References

[1] Di Maio, C., Vassallo, R., Vallario, M. (2013) Plastic and viscous shear displacements of a deep and very slow landslide in stiff clay formation. *Eng. Geol.* **162**, 53–66

[2] Goodman, R.E., Taylor, R.L., Brekke, T.L. (1968) A model for the mechanics of jointed rock. *J. Soil Mech. Found. Div. ASCE*, **94**, 637–659.

[3] Segura, J.M., Carol, I. (2008) Coupled HM analysis using zero-thickness interface elements with double nodes. Part I: Theoretical model. *Int. J. Numer. Anal. Meth. Geomech*. **32**, 2083–2101.

[4] Di Maio, C., Scaringi, G. (2016) Shear displacements induced by decrease in pore solution concentration on a pre-existing slip surface. *Eng. Geol.* **200**, 1–9.

[5] Di Maio, C., De Rosa, J., Vassallo, R., Coviello, R., Macchia, G. (2020) Hydraulic conductivity and pore water pressures in a clayey landslide: experimental data. *Geosciences* **10**(3), 102.

[6] Kaliakin, V.N., Li, J. (1995) Insight into deficiencies associated with commonly used zero-thickness interface elements. *Comput. Geotech.* **17**(2), 225–252.

NUMERICAL INSIGHT ON THE ROLE OF HYDRAULIC PROPERTIES ON INFILTRATION AND EVAPORATION

M. Aimar[1], G. Della Vecchia[2], G. Guida[3], G. Musso[1] and V.S. Vespo[1]
[1] Politecnico di Torino, Torino, Italy
[2] Politecnico di Milano, Milano, Italy
[3] University of Roma Tor Vergata, Roma, Italy

1. Introduction

The pore water pressure in the vadose zone is controlled by the interaction between the soil and the atmosphere, through evaporation and infiltration. These processes are strongly influenced by the soil hydraulic conductivity and water retention properties. In this contribution, the role of the parameters characterizing the soil hydraulic behaviour is investigated via a numerical model developed to reproduce infiltration and evaporation. The model is based on the balance equations of water and air mass and thermal energy, integrated with the Finite Element Method by using the software COMSOL Multiphysics®.

2. Numerical model

Modelling of infiltration and evaporation processes in unsaturated soils is generally based on the mass balance equations of the air and water species [1], by including a storage term accounting for the changes in the liquid degree of saturation S_l and, if necessary, in porosity. Mass transport occurs via advection and diffusion, according to Darcy's and Fick's laws. It is acknowledged that modelling evaporation processes also requires the thermal energy balance, including the heat flux due to conduction and convection and obtaining the temperature field. In this work, porosity changes were neglected and the linear momentum balance of the solid skeleton was not implemented.

A 1D simulation of evaporation and infiltration was carried out for a 0.3 m high vertical soil column. The water retention curve of the soil (*i.e.*, the link between S_l and matric suction s) was described by the van Genuchten relationship [2]:

$$S_l = S_{l,r} + \left(1 - S_{l,r}\right)\left[1 + \left(sP^{-1}\right)^n\right]^{-m} \tag{1}$$

where $S_{l,r}$ = 0.05 is the residual degree of liquid saturation, and P, n (=3) and m (=0.4) are model parameters. The advective flow of liquid and gas was modelled through a generalized Darcy's law with a liquid or gas conductivity K_α (α = liquid or gas) equal to the product between a saturated value K_{sat} and the relative permeability $k_{\alpha,rel}$ – the latter given in ref. [2].

The simulation of evaporation assumed that the column was initially fully saturated by liquid. An outgoing water flux, *i.e.* the actual evaporation rate *AE*, was imposed at the model top. *AE* is a function of a potential evaporation rate, *PE*, depending on temperature, relative humidity and wind speed (here neglected, given the controlled laboratory conditions). The simulation of the infiltration assumed a column with an initial S_l = 0.2. Infiltration was triggered by imposing atmospheric pressure on the liquid and gas phases at the top boundary. The bottom of the column was set as impervious in both models. Further details can be found in [3, 4].

3. Sensitivity analysis

The results of the numerical simulations obtained with two values of van Genuchten's parameter P (*i.e.*, 1 kPa and 100 kPa) and two values of K_{sat} (*i.e.*, 10^{-4} m/s and 5×10^{-9} m/s) are presented in the following. These scenarios were selected from a larger dataset encompassing a broad

range of subsoil conditions of engineering interest [3]. Figure 1(e) reports the evolution of the normalized evaporation rate *AE*/*PE* for the selected parameter combinations. In general, increasing K_{sat} and/or *P* entails a longer stage of liquid water flow, with a delayed drop in the *AE*/*PE* ratio. As for the infiltration problem, Figure 1(i) shows the normalized infiltration rate i/K_{sat} versus the modified time $t^* = t \times K_{sat}$ (*i* being the infiltration rate and *t* the physical time). The saturated conductivity governs the magnitude of the infiltration rate and the time scale of the phenomenon, while *P* affects the infiltration evolution, as the time at which a sharp decrease in infiltration occurs is shorter as *P* increases. The role of these parameters is also highlighted from the profiles of liquid degree of saturation S_l at different times. Figure 2(e) provides the profiles when residual saturation at the top of the column is attained during evaporation. Higher air entry values *P* lead to more uniform S_l profiles along depth, whereas if the hydraulic conductivity is small marked changes in liquid degree of saturation occur in the proximity of the surface. Saturation profiles during infiltration are presented in Figure 2(i): interestingly, the isochrones of water content do not depend on K_{sat} when t^* is adopted as a time variable. During the initial stages of infiltration, the water front progresses downwards, with S_l slightly below 1. Liquid saturation is approached only when the front has reached the bottom of the column. For $P = 1$ kPa, full saturation is first reached at the base of the column and then the saturation front moves upwards. For $P = 100$ kPa, the process is more homogeneous along the column height.

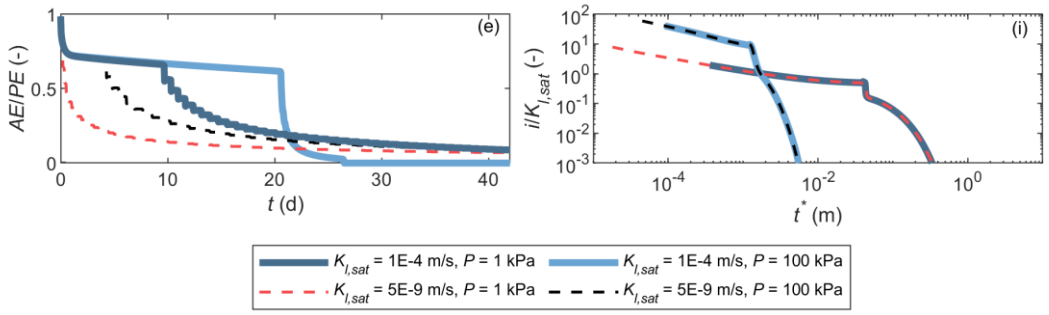

Figure 1. Time histories of (e) evaporation rates and (i) infiltration rates.

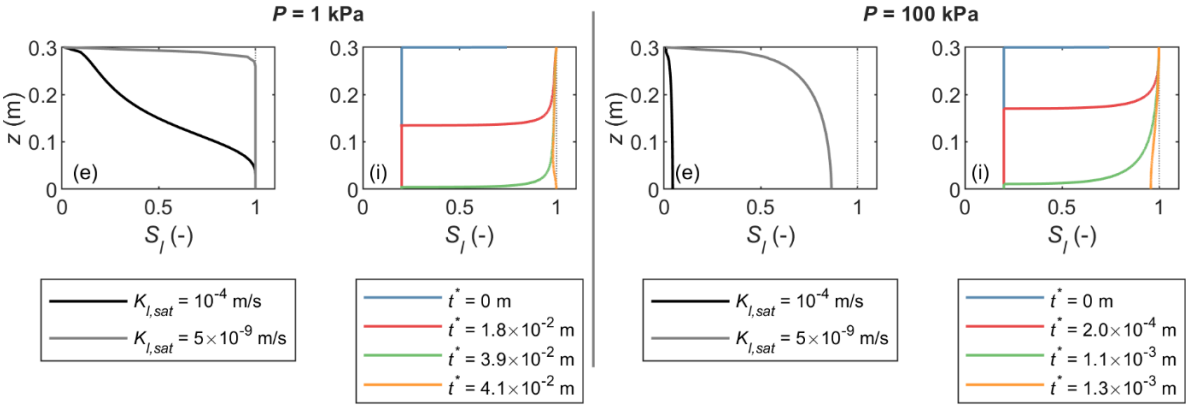

Figure 2. Profiles of the liquid degree of saturation S_l in (e) evaporation and (i) infiltration.

5. References

[1] Bear J. & Cheng A.H.-D. (2010). *Modeling groundwater flow and contaminant transport*, vol 23. Springer, Dordrecht.

[2] Van Genuchten M.T. (1980). A closed-form equation for predicting the hydraulic conductivity of unsaturated soils, *Soil Sci Soc Am J*, **44** (5), 892-898.

[3] Guida G., Vespo V.S., Musso G. & Della Vecchia G. (2023). The role of hydraulic and thermal properties of soil on evaporation: a numerical insight, *Environ Geotech [under review]*.

[4] Aimar M., Della Vecchia G. & Musso G. (2023): One phase vs two-phase modelling of infiltration processes. In: Conferenza Nazionale dei Ricercatori di Ingegneria Geotecnica (CNRIG23).

A MULTIPHYSICS MODEL FOR THE NEAR-FIELD EVOLUTION OF A GEOLOGICAL REPOSITORY FOR RADIOACTIVE WASTE

U. Vo[1], M. Fall[1] , J. Infante-Sedano[1] and T. S. Nguyen[1,2,*]
[1] University of Ottawa, Ottawa, Ont., Canada
[2]Canadian Nuclear Safety Commission, Ottawa, Canada
**Son.nguyen@cnsc-ccsn.gc.ca*

1. Introduction

Geological disposal of radioactive waste originating from the production of electricity is being considered in many countries, including Canada. A deep geological repository (DGR) relies on a system of multiple engineered and natural barriers in order to provide containment and isolation of the highly radioactive used fuel, in order to protect the surface environment for periods of hundreds of thousands to millions of years. For example, in the current Canadian concept [1]: i) the first barrier is the nuclear fuel pellet that is durable and temperature-resistant and possesses a low dissolution potential; ii) the second barrier is the fuel bundle composed of a number of corrosion-resistant zircaloy sealed tubes called elements, in which the fuel pellets are inserted; iii) the third barrier is the fuel container containing 48 bundles which is designed to be resistant to anticipated loads and corrosion; iv) the fourth barrier is a compacted bentonite sealing system that would surround the container in the emplacement room (the buffer); v) the fifth barrier is the natural rock formation that would protect the DGR from natural events and from human intrusion, and also provide a barrier to eventual radionuclide migration to the near surface environment. For the long time period being considered, the multiple barrier system would be subjected to many perturbations that result in coupled multiphysical processes that would affect its performance. In this work, we formulate a mathematical model of these processes focusing on the compacted bentonite buffer and the host rock in the vicinity of the buffer. This work is part of the CNSC's regulatory research program to build an independent knowledge for the review of licence applications for DGRs in Canada.

2. Conceptual and mathematical model

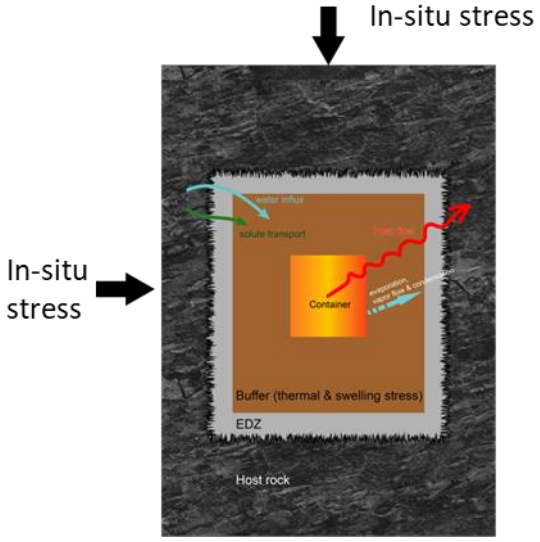

Figure 1. Coupled THMC processes in the buffer and near-field host rock

The processes in the near–field of a DGR are conceptualized in Figure 1. The bentonite buffer and host rock are idealized as porous media. The host rock is saturated with saline water while the bentonite buffer is emplaced in an unsaturated condition. Suction in the buffer would draw pore fluid from the host rock. On the other hand, radiogenic heat from the used fuel, in addition to inducing thermal stresses in the overall system, would trigger a transient outward flow of vapour and liquid water from the buffer. These two opposing flow components result in a complex evolution of the water content in the buffer that in turn influences the development of swelling pressure. Solutes in the rock porewater would also have a strong influence on the swelling potential of the buffer. Based on the above conceptualization, a mathematical model was developed, with governing equations derived from the consideration of momentum conservation, mass conservation and energy (heat) conservation, along with the adoption of a modified Bishop's effective stress principle, Darcy's laws for partially saturated media, and empirical models for swelling pressure that take into account temperature and salinity effects. The primary unknowns in the equations are temperature, pore fluid pressure, displacement of the solid skeleton, and solute concentrations.

3. Verification and validation of the model

The model is verified first against existing analytical solutions. It is then validated against experimental data for a i) thermal diffusion experiment in a bentonite column [2], and ii) the transport of saline solution in a clayrock at elevated temperature [3] (Figure 3).

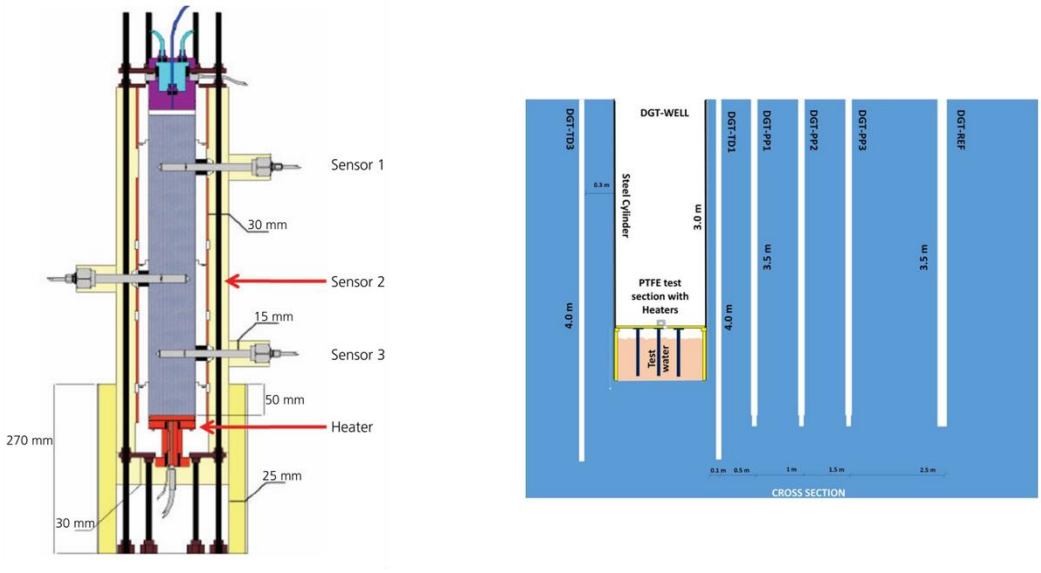

a) Thermal diffusion in a bentonite column

b) Thermal diffusion of salt solution in clayrock

Figure 3. Experiments for validation of mathematical model

5. References

[1] Noronha, J. (2016). Deep geological repository conceptual designs report: crystalline/sedimentary rock environment. Report No. APM-REP-00440-0015-R001, Issue May.

[2] Nguyen TS, Li Z, Garitte B, Barnichon JD (2019). Modelling a heater experiment for radioactive waste disposal. *Environmental Geotechnics*, **6(2)**, 87–100.

[3] Institut de Radioprotection et de Surete Nucleaire (2021). DIGIT, a thermal diffusion experiment. *Private communication*.

NUMERICAL ANALYSIS OF HYDRO-THERMAL FRACTURING IN ANISOTROPIC AND HETEROGENEOUS ROCKS

***Z. Yu*[1,2], *J.F. Shao*[2,1], *M. Wang*[2], *Y. Sun*[2] *and M.N. Vu*[3]**

[1] *Key Laboratory of Ministry of Education on Safe Mining of Deep Metal Mines, College of Resources and Civil Engineering, Northeastern University, Shenyang, 110819, China*

[2] *University of Lille, CNRS, EC Lille, LaMcube, UMR9013, 59000 Lille, France*

[3] *Andra, 92298 Chatenay-Malabry, France*

1. Introduction

In the context of underground disposal of radioactive waste, it is crucial to investigate the short and long term deformation and damage processes of both geological and engineered barriers, under thermal and hydromechanical conditions. The objective of this paper is to study the cracking process induced by temperature change. The novelty is to take into account the effect of material anisotropy and microscopic heterogeneity.

2. Methodology

Among various numerical methods developed for modeling cracking processes, the phase-field method is able to describe the initiation and propagation of cracks based on the variational formulation of fracture [1, 2]. In this study, two independent damage fields are used to easily capture tensile and shear cracks as well as mixed ones. By minimizing the total energy functional [3], the evolutions of two crack fields are governed by the following relations:

$$\begin{cases} -h_t'(d^t)w_{e+}^0 - g_c^t\left\{\frac{1}{l_d}d^t - l_d\Delta d^t\right\} = 0 \ , \ \dot{d^t} > 0 \\ -h_s'(d^s)w_-^s - g_c^s\left\{\frac{1}{l_d}d^s - l_d\Delta d^s\right\} = 0 \ , \ \dot{d^s} > 0 \end{cases} \tag{1}$$

where $d^\alpha(\alpha = t, s)$ denotes the auxiliary scalar variable of each crack field and l_d is the scale length parameter controlling the width of localized crack. The functions $h_t'(d^t)$ and $h_s'(d^s)$ describe the effects of tensile and shear cracks on the elastic properties of materials, while g_c^t and g_c^s denote the toughness for tensile and shear cracks. The driving energies of tensile crack w_{e+}^0 and shear crack w_-^s are given by:

$$\begin{cases} w_e^{0+} = \frac{1}{2}\boldsymbol{\sigma}^{t+} : \boldsymbol{\varepsilon^e} \\ \\ w_-^s = \frac{1}{2G}\langle \frac{\langle\sigma_1^t\rangle_- - \langle\sigma_3^t\rangle_-}{2\cos\varphi} + \frac{\langle\sigma_1^t\rangle_- + \langle\sigma_3^t\rangle_-}{2}\tan\varphi - c\rangle_+^2 \end{cases} \tag{2}$$

where $\boldsymbol{\sigma}^{t+}$ is the Terzaghi effective stress tensor, which is more suitable for rock-like material. In addition, at the microscopic scale, the studied claystone is composed of clay matrix and mineral grains such as quartz and calcite [4]. The macroscopic elastic properties of claystone are determined here through a Mori-Tanaka homogenization scheme.

3. Example of application

We show here an example of cracking induced by temperature change in a saturated porous medium. We consider a cylindrical sample with a radius of 10 mm, as shown in Figure 1. The initial elastic properties are not uniform in the sample due to a random spatial distribution of mineral compositions.

The external boundary is first subjected to a confining stress of σ_{rr}^0 = -12 MPa. An initial pore pressure of p_0 = 5 MPa is also prescribed. Then, a constant heat power of Q = 0.44 W is applied at the cylinder center point. The external boundary surface is considered as impermeable and adiabatic during the heating period. The heat diffusion takes place quite rapidly in the whole sample due to its small size. It is very interesting to observe that the tensile damage field is clearly not uniform. This is the consequence of material heterogeneity.

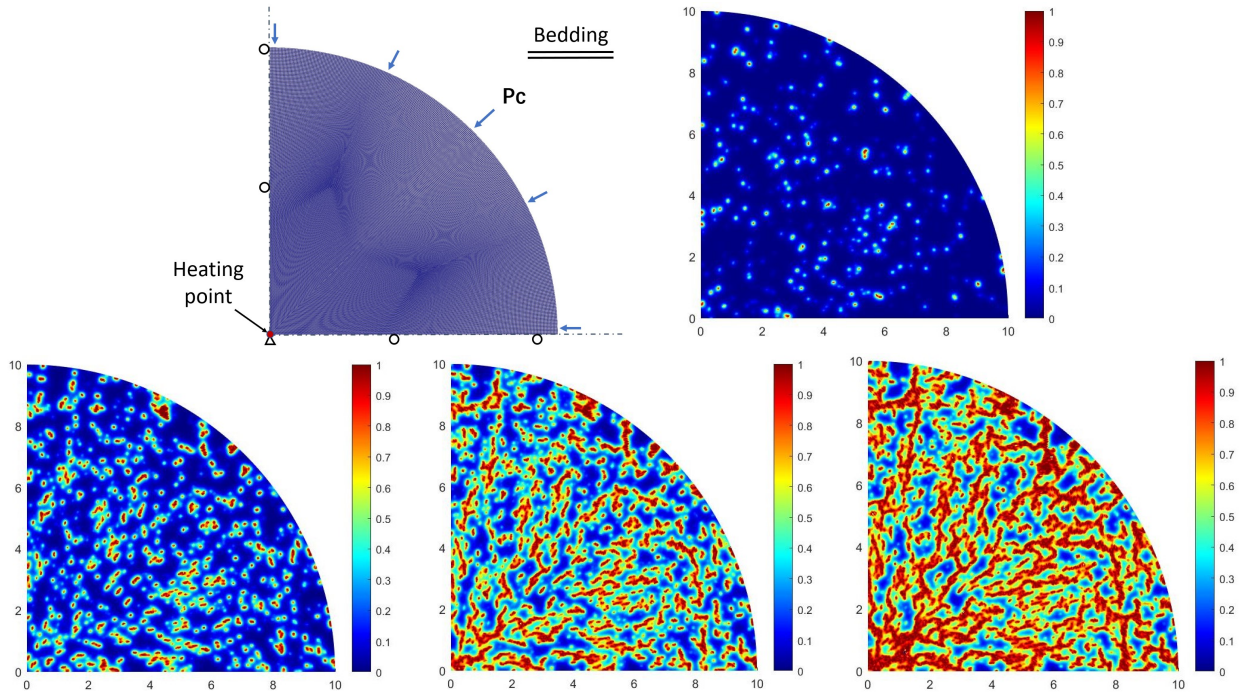

Figure 1. Geometry and boundary conditions of heating test and distributions of tensile damage at four time steps of 600, 880, 1080 and 1200 minutes

4. Conclusions

In this study, we have proposed an extended phase-field model to describe the progressive cracking process in saturated rocks by considering thermo-hydromechanical coupling. Both tensile and shear cracks are considered. The initiation of cracks is directly related to the spatial distribution of mineral compositions of rock. Mainly tensile cracks are induced by temperature rise. The initial anisotropy of material (bedding planes) has also an important influence on the induced cracking process (not shown in this abstract).

References

[1] Francfort, G. A. and Marigo, J.-J. (1998). Revisiting brittle fracture as an energy minimization problem. *Journal of the Mechanics and Physics of Solids*, **46**, 1319–1342.

[2] Bourdin, B., Francfort, G. A., and Marigo, J.-J. (2000). Numerical experiments in revisited brittle fracture. *Journal of the Mechanics and Physics of Solids*, **48**, 797–826.

[3] Yu, Z., Sun, Y., Vu, M. N., and Shao, J. F. (2023). Modeling of mixed cracks in rock-like brittle materials under compressive stresses by a double-phase-field method. *Rock Mechanics and Rock Engineering*, **online**, doi.org/10.1007/s00603–022–03196–w.

[4] Armand, G., Conil, N., Talandier, J., and Seyedi, D. M. (2017). Fundamental aspects of the hydromechanical behaviour of callovo-oxfordian claystone: from experimental studies to model calibration and validation. *Computers and Geotechnics*, **85**, 277–286.

EXPERIMENTAL BEHAVIOR AND CONSTITUTIVE MODELING OF SOILS SUBJECTED TO FREEZE-THAW CYCLES

M. Sanchez[1], B. Zhou[1,2], and Z. Shang[1]
[1]Department of Civil and Environmental Engineering, Texas A&M University, USA.
[2] Power China Huadong Engineering Corporation Limited, Hangzhou, China.

1. General

Seasonal frozen soils dominate approximately 55% of the total earth's surface land. In those regions, a good understating of the behavior of frozen soils is critical for a safe and economical design of new engineering projects and for assessing the condition of existing civil infrastructure. Furthermore, as a result of the changes in climatic conditions, issues associated with soils subjected to Freezing-Thawing (Fr-Th) cycles are becoming more significant. This is because key engineering properties of soils, such as, strength, stiffness, permeability, and thermal conductivity depend on the freezing temperature (T) and number of Fr-Th cycles, among other factors.

It has been observed that under freezing temperatures not all the water present in soils is converted into ice [1]. The amount of unfrozen water in frozen soils is mainly related to capillary effects. The unfrozen water content at a given freezing temperature can be directly related to the cryonic suction (e.g., [2]) and it plays a critical role to understand the volume change behavior observed in frozen soils (e.g., [3]). This work presents an experimental and numerical investigation related to the volumetric behavior of soils subjected to Fr-Th cycles. The work also discusses the results of a new constitutive model proposed to describe the behavior of soils under repeated Fr-Th cycles. This study shows that irreversible strains develop as a result of Fr-Th cycles. Their sign and magnitude strongly depend on the freezing temperature, stress level and loading history.

2. Materials and methods

A commercial silt was adopted for the experiment campaign. The soil did not exhibit a plastic behavior. The adopted water content to prepare the reconstituted samples was 30%, which is around 1.2 times the liquid limit. The initial void ratio was 0.8. The slurry was subjected to Fr-Th cycles in a 1-D cell manufactured in a 3-D printer. The test was conducted under open system conditions inside a fully instrumented environmental chamber capable of conducting tests at freezing temperatures under relative humidity-controlled conditions. Volume changes were recorded using a Linear Variable Differential Transformer (LVDT) during cyclic Fr-Th. The tests were conducted under different loading and stress history conditions, covering a wide range of over consolidation ratios (OCR), including OCR = 1, i.e., normally consolidated (NC) conditions.

For the numerical simulations of the tests, an advanced constitutive model was developed in the context of elastoplasticity theory for strain-hardening materials. The proposed framework incorporates key features to reproduce the behavior of frozen soils, such as, cryonic suction (e.g., [2]), volume change associated with water phase transformation, as well as dependence on loading history and stress level. The definition of effective stresses for frozen soils proposed in [2] and [3] has been adopted in this work.

3. Results

The soil samples were loaded and/or unloaded up to pre-determined stress levels at laboratory room temperature (i.e., T = 20°C). Then, the samples were subjected to eight Fr-Th cycles with temperatures variation between 5°C and -7°C. Each Fr-Th cycle was completed in one day.

Figure 1 shows, as an example, the results obtained for one of the experiments involving a normally consolidated (NC) sample. In this experiment a vertical stress σ_v= 10 kPa was applied first. Then, a first series of Fr-Th cycles were applied maintaining σ_v= 10 kPa. The collapse

compression behavior observed during these Fr-Th cycles is identified as C1N_10. Afterwards, the sample was loaded up to vertical net stress σ_v = 100 kPa and subjected to another series of Fr-Th cycles, exhibiting a subsequent volume reduction (C1N_100). Then, the sample was unloaded until σ_v = 10 kPa, and the third series of Fr-Th cycles were applied. Under this OC state, the sample experienced a volume expansion (C1O_10). In all the cases, it was also observed that the major accumulation of irreversible strains took place during the initial Fr-Th cycles, after the 5th cycle no net plastic defamations were recorded.

Figure 1a) shows the generalized σ_v -T path, together with the cycles of the applied temperature. Figure 1b shows the comparison of the numerical and experimental results in terms of σ'_v and void ratio (*e*), together with the evolution of *e* during Fr-Th cycles. In an initially OC sample, a tendency to a net increase of the volume during Fr-Th cycles was observed. It is also evident that the model can satisfactorily capture the main experimental trends observed in this study. Those include a tendency for the NC soil to compress during Fr-Th cycles and a volume expansion when the Fr-Th cycles are applied to an OC soil.

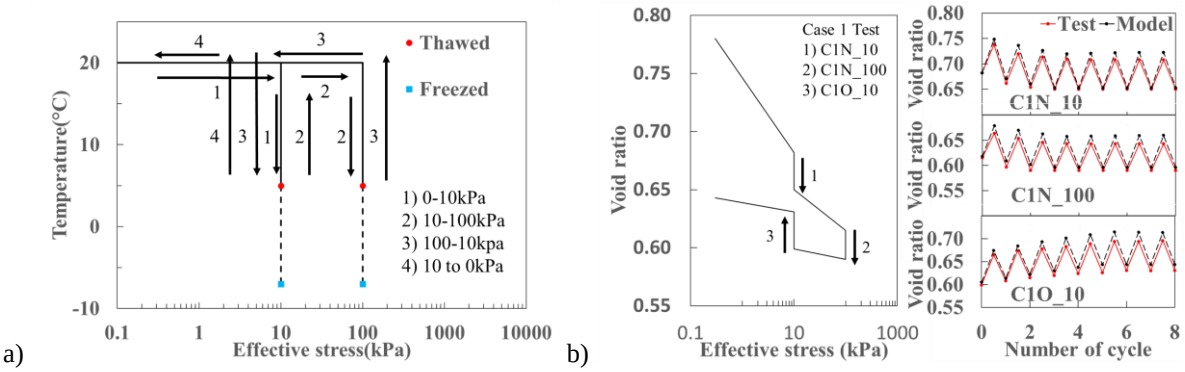

Figure 1. Test and modeling results, a) generalized stress path σ'_v–T together with T cycles, and b) changes of e in terms of σ'_v, together with the evolution of e during Fr-Th cycles.

4. Conclusions

This study examined the behavior of soils subjected to Fr-Th cycles through a set of experiments conducted under constant σ_v and at freezing temperature. It was observed that NC soils tend to accumulate positive volumetric plastic strains during Fr-Th cycles, whereas Fr-Th cycles applied to OC soils result in accumulation of negative volumetric strains (dilatancy). In both cases (i.e., NC and OC) the accumulation of plastic strains was more noticeable during the first cycles. An advanced constitutive model was adopted to interpret the test results and to explore other factors affecting the response of soils subjected to Fr-Th cycles.

5. Acknowledgments

The authors acknowledge the financial support from the United States National Science Foundation, award number: 2034204.

6. References

[1] Taber, S. (1930). The mechanics of frost heaving. *The Journal of Geology*, **38**(4), 303-317.

[2] Nishimura, S., Gens, A., Olivella, S. & Jardine, R. J. (2009). THM-coupled finite element analysis of frozen soil: formulation and application. *Géotechnique*, **59**(3), 159–171.

[3] Shastri A., Sánchez M., Gai X. Lee M., & Dewers T. (2021). "Mechanical behavior of frozen soils: experimental investigation and numerical modeling". *Comput Geotech*, **138**, 104361

4. Discrete Element Method and its applications

DEM SIMULATIONS OF FRACTURE IN PRE-FLAWED MARBLE SPECIMENS SUBJECTED TO UNIAXIAL COMPRESSION

D. Tomporowski and J. Tejchman
Gdańsk University of Technology, Gdańsk, Poland

1. Introduction

Rock masses are highly disordered, heterogeneous, and anisotropic quasi-brittle materials with a complex microstructure associated with a variety of mineralogical compositions, grain morphologies, and grain size distributions. Different forms of discontinuities, including bedding planes, joints, faults, shear zones, fissures, and dikes, may be found in the rocks. Fracture is a significant property of rock-like materials that causes both strength and stiffness losses and occurs before the structure fails. A narrow zone constituted of scattered micro-cracks called a fracture process zone (FPZ) or a strain localization zone is generated at first. A unique discrete macro-crack occurs during further deformation. Because fracture/damage usually begins and spreads from pre-existing discontinuities, they considerably impair the rock mass strength (being weak parts). Thus, at the macroscopic level, rock failure is primarily governed by its microstructure, which includes pre-existing defects and cracks. As a result, a good knowledge of fracture in rock masses under loads at the mesoscale is essential for failure prediction and mitigation of related hazards, as well as for designing safe and cost-effective structures built in and on rock masses.

It has been known from the literature that geometries of defects, such as flaw inclination angle, intact length between faults, and bridging angle, have a significant impact on the mechanical compressive behaviour of rock masses. Pre-flawed specimens have two types of cracks in experiments: wing (tensile) cracks and secondary (shear) cracks. Wing cracks are main tensile cracks that begin at or near the points of defects and propagate in a curved manner away from the greatest compressive stress direction. Secondary cracks, on the other hand, begin in a direction that is direction quasi-coplanar to flaws and parallel to wing fractures, but in the opposite direction. They spread out more diffusely and appear to arise rather from a shear mechanism. Coalescence occurs when two flaws are linked together by a mix of cracks. It can take place through wing cracks, a combination of wing and secondary cracks (which is a stable process), or secondary cracks (the process is unstable).

2. Research aims

The current work focuses on a progressive fracture phenomenon in rocks under uniaxial compression [1]. We studied numerically in depth the impact of pre-existing open faults with various inclinations on the formation and coalescence of cracks in marble specimens at the meso-level. Marble was described as a cohesive/bonded granular material in which constituent particles exerted mutual forces on one another through their contacts. The behaviour of cracked rock specimens was reproduced using a 3D particle DEM model that was shown in the literature to be particularly effective in mimicking the progressive failure of rocks. A series of numerical tests were performed in the current paper on intact and pre-cracked/notched marble specimens under uniaxial compression to see if DEM could replicate wing and secondary cracks developing at the tips of pre-existing flaws and to gain meso-mechanical insights into the damage mechanisms associated with those cracks. The effect of the inclination of pre-existing faults on the fracture pattern and compressive strength of specimens received here special consideration. The fracture in marble specimens was modelled using either a packing of bonded spherical or clumped discrete elements

for comparison The numerical simulations were compared directly to the experimental findings by Yang et al. [2]. In the experiments [2], four types of cylindrical specimens 'A'-'D' were prepared. Specimens 'A' were intact, and the remaining specimens were not. The pre-existing cuts had a different angle of inclination to the vertical: 30^o (specimen 'B'), 45^o ('C') and 60^o ('D').

The novel aspects of the research in the current paper are: a) thorough 3D simulations of fracture of cylindrical pre-flawed marble specimens under uniaxial compression using DEM as compared to laboratory experiments [2], b) comparative fracture calculations in rock specimens utilizing either spheres or clumps, and c) investigation of the effect of the ratio of cohesive and tensile strength of particle contacts (*C/T*-ratio) on the specimens' behaviour. The impact of a grain size range was also examined. The DEM simulations were conducted without the use of mesostructure data from real marble samples [2] due to a lack of information regarding the mineralogical volume, location, shape and size of minerals, and initial porosity. The open-source DEM code Yade [3,4] was used to run all 3D DEM simulations.

3. Conclusions

When compared to spheres, clumps had a greater uniaxial compressive to tensile strength ratio than spheres (by a factor of around 2).

Moderate agreement between numerical and experimental results was achieved. The numerical strength of specimens decreased as the pre-existing flaw inclination to the horizontal was lowered, similar to the tests. It was, however, between 25% and 200% higher in pre-flawed specimens than in the experiments (independently of the grain shape). Pure spheres and non-symmetric clumps had some different effects on failure patterns. The calculated crack pattern in the pre-flawed specimens 'C' and 'D' was in good agreement with the experiment when employing spheres, whereas the pre-flawed specimen 'B' was in medium agreement, and the intact specimen 'A' showed no agreement. For clumps, the intact specimen 'A' and the pre-flawed specimens 'C' and 'D' had a fair agreement, whereas the pre-flawed specimen 'B' had no agreement. We can conclude that a better agreement can be achieved when using clumps by also considering that the ratio between compressive and tensile strength is higher and more realistic in this case. The DEM results can most likely be improved by considering the true crystal shape and true specimen porosity.

The *C/T* ratio had a great impact on failure patterns in specimens composed of spheres. The satisfactory DEM results in terms of failure patterns were obtained for the ratio *C/T*=2. The experimental failure patterns should serve as the foundation for calibrating this ratio.

The number of all broken contacts decreased as the inclination of a pre-existing flaw to the horizontal was lowered. It was higher in clumps due to a higher number of particle contacts.

The addition of small grains did not affect the calculated strengths and fracture geometry.

4. References

[1] Tomporowski, D., Nitka, M., Tejchman, J. (2023). Application of the 3D DEM in the modelling of fractures in pre-flawed marble specimens during uniaxial compression, *Engineering Fracture Mechanics* **277**, 108978.

[2] Yang, S.Q., Jiang, Y.Z., Xu, W.Y. & Chen X.Q. (2008). Experimental investigation on strength and failure behavior of pre-cracked marble under conventional triaxial compression, *International Journal of Solid and Structures* **45**, 4796-4819.

[3] Šmilauer, V. et al. Yade Documentation 3rd ed. The Yade Project (2021). doi:10.5281/zenodo.5705394 (http://yade-dem.org/doc/).

[4] Nitka, M., Tejchman, J. (2020). Meso-mechanical modelling of damage in concrete using discrete element method with porous ITZs of defined width around aggregates, *Engineering Fracture Mechanics* **231**, 107029.

MODELING CAPILLARY TRANSITIONS IN UNSATURATED MEDIA ACROSS ALL SATURATION REGIMES

***N. Younes*[1,2,3], *R. Wan* [3], *A. Wautier*[2], *O. Millet*[1], *and F. Nicot* [4]**

[1] *LaSIE, UMR CNRS 7356, University of La Rochelle, 17042, La Rochelle Cedex 1, France*

[2] *INRAE, Aix-Marseille University, UR RECOVER,13182 Aix-en-Provence Cedex 5, France*

[3] *Department of Civil Engineering, Schulich School of Engineering, University of Calgary, Canada*

[4] *University Savoie Mont-Blanc , ISTerre, Chambéry, France*

1. Context

In most geotechnical engineering applications, the presence of unsaturated soils is unavoidable, especially in earth dikes and dams. When a soil is wetted so that it is partially saturated, capillary bridges form in between the grains, making its behavior way more complex than that of dry and fully saturated soils which are on the other hand well understood. In unsaturated soils, several regimes can be distinguished depending on the degree of water saturation: *pendular*, *funicular*, and *capillary* regimes. The first regime (pendular) refers to capillary bridges existing only between pairs of grains and has been previously investigated in the literature by resorting to point capillary forces rather than the capillary stress tensor $\boldsymbol{\sigma}^{\text{cap}}$ [1–4]. The latter approach, however, does not hold for the two other regimes (funicular and capillary), in which the *coalescence* of capillary bridges takes place. As such, one can indirectly determine the capillary stress tensor as follows

$$\boldsymbol{\sigma}^{\text{cap}} = \boldsymbol{\sigma}^{\text{tot}} - \boldsymbol{\sigma}^{\text{LW}} \tag{1}$$

where $\boldsymbol{\sigma}^{\text{tot}}$ is the total stress a sample is being subjected to, and $\boldsymbol{\sigma}^{\text{LW}}$ is the Love-Weber stress tensor that explicitly computes every single grain-to-grain interaction.

2. Numerical model

We therefore propose a phase-field-based Lattice Boltzmann Method (LBM) model coupled with the Discrete Element Method (DEM) with the purpose of simulating unsaturated media over a large range of degrees of saturation S_r, and most importantly the transition between the various regimes. The formation of capillary bridges between the particles is simulated via a LBM scheme that solves Navier-Stokes and Allen-Cahn equations to address multiphase flow in complex geometries. This method has recently demonstrated its capabilities in handling the merging of capillary bridges [5], which allows us to model partially saturated media at different saturation regimes, *e.g.*, *pendular*, *funicular*, and *capillary* regimes. As for the grain kinematics, these are computed using DEM where the contact behavior between spherical particles is based on a simple elastic-plastic contact law [6]. Using an efficient LBM x DEM coupling framework, this allows us to simulate the capillary effect in wet sand whereby a cubical sample readily collapses when dry, whereas it can stand up when wet at different degrees of saturation, as seen in Figures 1(a), (b) and (c). To quantify the capillary effects as the granular system is being wetted, we define the mean capillary stress p^{cap} as follows:

$$p^{\text{cap}} = \frac{1}{3}\text{Tr}\left(\boldsymbol{\sigma}^{\text{cap}}\right). \tag{2}$$

3. Results

An assembly of several thousands of spherical particles connected by capillary bridges is wetted at increasing degrees of water saturation. It is shown that the mean capillary stress p^{cap} increases

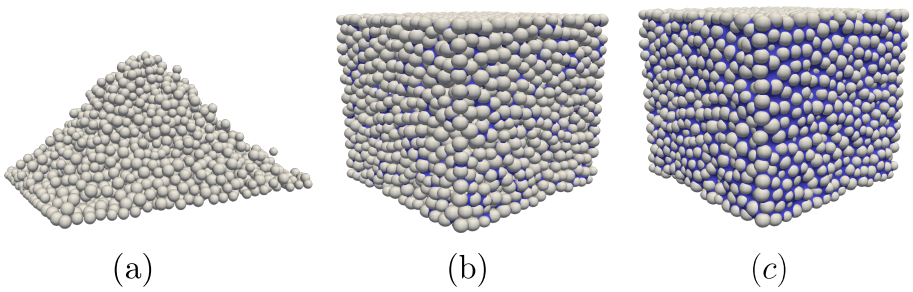

Figure 1. (a) Collapse of a dry sample. (b) and (c) Stable wet samples for degrees of saturation of $Sr \in \{11.41; 72.77\}$ %, respectively. All the simulations do not have supporting lateral walls.

with the degree of saturation up to a certain threshold beyond which capillarity effects are lost until complete saturation, cf. Figure 2. The example provided in this short communication indicates that the coupling of LBM with DEM computations can be a viable tool for modeling unsaturated soils at the micro-scale across the saturation regimes, *i.e.*, from *pendular*, *funicular*, *capillary* to full saturation.

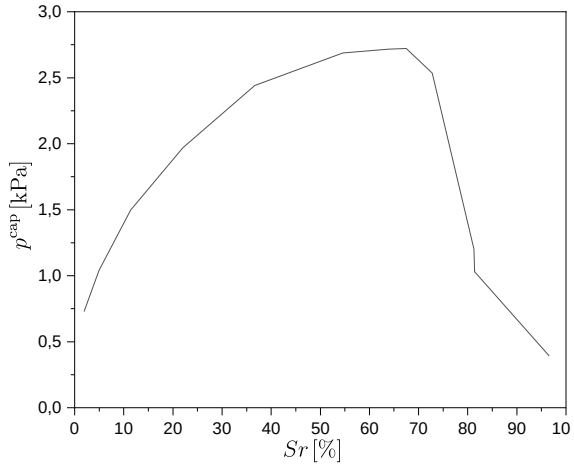

Figure 2. Mean capillary stress p^{cap} [kPa] evolution in terms of degrees of saturation S_r [%].

.

References

[1] Luc Scholtès et al. “On the capillary stress tensor in wet granular materials”. In: *International journal for numerical and analytical methods in geomechanics* 33.10 (2009), pp. 1289–1313.

[2] Jérôme Duriez and Richard Wan. “Stress in wet granular media with interfaces via homogenization and discrete element approaches”. In: *Journal of Engineering Mechanics-ASCE* 142.12 (2016).

[3] Jérôme Duriez and Richard Wan. “Contact angle mechanical influence in wet granular soils”. In: *Acta Geotechnica* 12.1 (2017), pp. 67–83.

[4] Jérôme Duriez et al. “The micromechanical nature of stresses in triphasic granular media with interfaces”. In: *Journal of the Mechanics and Physics of Solids* 99 (2017), pp. 495–511.

[5] N Younes et al. “Phase-field Lattice Boltzmann model for liquid bridges and coalescence in wet granular media”. In: *Powder Technology* (2022), p. 117942.

[6] Peter A Cundall and Otto DL Strack. “A discrete numerical model for granular assemblies”. In: *geotechnique* 29.1 (1979), pp. 47–65.

DEM-PFV ANALYSES OF SUFFUSION PHENOMENA DURING PERMEATION GROUTING TREATMENTS

K. Boschi [1,2], B. Chareyre [3] and C. di Prisco [1]
[1] Politecnico di Milano, Milan, Italy
[2] International Centre for Numerical Methods in Engineering, Barcelona, Spain
[3] Grenoble Institute of Technology - 3SR, Grenoble, France

1. Introduction

In permeation grouting applications in highly graded soils, even if low injection pressures are imposed, suffusion phenomena are expected [1, 4]: finer particles, not involved in force chains, are washed out by seepage, without any change in volumetric strain. When suffusion takes place, both particle size distribution (PSD) and intrinsic permeability (k) of the injected soil starts evolving with time, leading to highly heterogeneous spatial distributions. This complex phenomenon is characterised by a solid-to-fluid transition of washed-out finer particles. For this reason, its numerical simulation requires a discontinuum approach. In this class of numerical methods, the authors have chosen to employ the DEM-PFV coupled method (implemented in YADE software [2, 3] and already validated by the authors [1] on seepage laboratory experimental test results), conjugating the capability of dealing with a pore-scale modelling and computational efficiency.

2. DEM-PFV model

The DEM-PFV generated model (Figure 1a) is homogeneous (with a rather constant void ratio e), assumed to be representative of an in-situ soil sample located at a certain distance from the injection source. The initially imposed confining pressure (p_0) mimics the depth of the sample. During the test, all the boundaries are rigid and kept fixed, except for the $y = 0$ rigid boundary on which total stress $\sigma_{yy} = p_0$ is imposed. The specimen is fully saturated by a Newtonian fluid (being μ_f the fluid viscosity) and subject to a hydraulic gradient i along the y direction, whereas the boundaries along z and x directions are assumed to be impervious. Gravity is neglected and, for $y = 0$, fluid pressure p is imposed equal to p_f, whereas, for $y = L$, $p = 0$. Therefore, $i = p_f/(L \cdot \gamma_f)$, being γ_f the fluid weight per unit volume. The two boundaries along y direction are selective: only DEM spheres with diameters $D < D_{20}$ can pass through them; in this way, boundary effects in the investigated suffusion phenomena are minimized. Specimens characterised by either continuously graded or gap-graded PSDs (as the ones shown in Figure 1b) are tested.

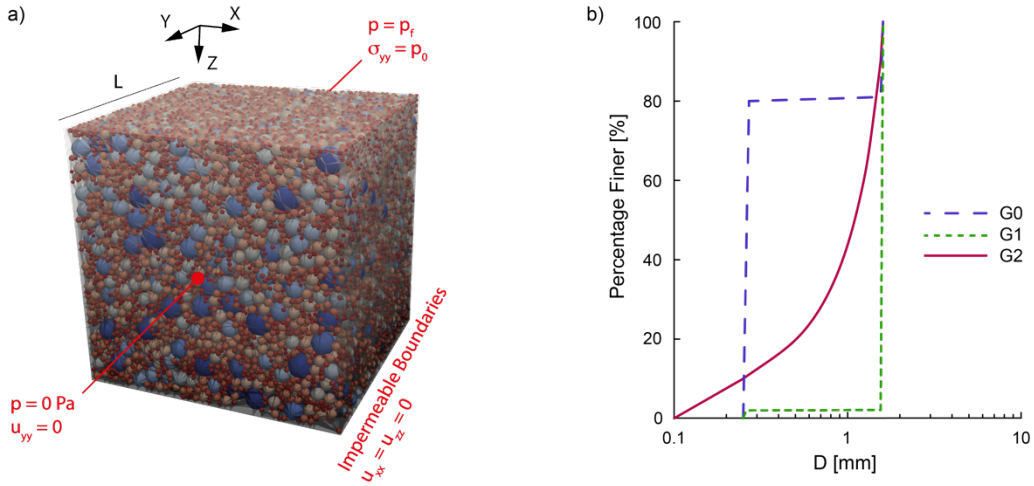

Figure 1. a) DEM-PFV model and b) employed PSDs.

3. Main results and discussion

A parametric analysis of how soil (PSD, e, p_0), fluid (μ_f) and injection conditions (i) affect suffusion and the associated mechanisms, occurring at the micro-scale, has been performed. As was expected, PSD turns out to play the key role in governing suffusion mechanisms. For example, in case $e = e_{max}$, $p_0 = 5$ kPa, $\mu_f = 1$ mPa·s and $i \cong 1$, if G0 PSD (Figure 1b) is tested, suffusion is not detected. In contrast, if G1 PSD is tested, its fine fraction is fully transported (Figure 2a) by the flux throughout pores. Finally, in case G2 PSD is tested, not all pores and constrictions are large enough to allow finer fraction transport, so clogging/deposition zones develop and then a small fraction of fine particles actually reaches the $y = L$ boundary (Figure 2b). For either lower i or higher μ_f, the temporal evolution from the initial homogeneous configuration to the final heterogeneous steady-state one is slower.

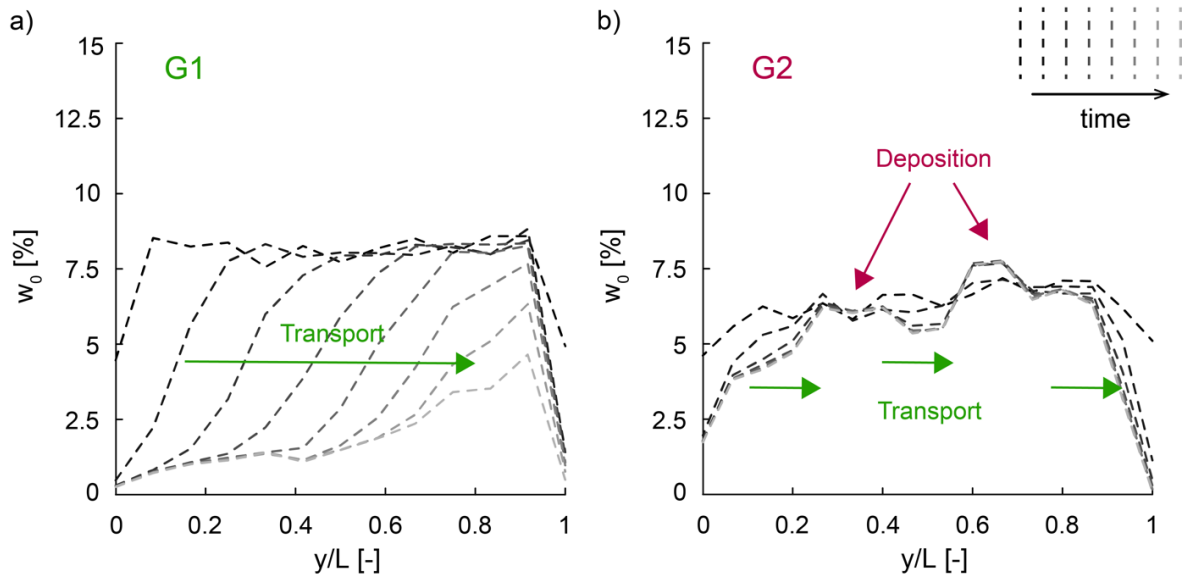

Figure 2. Spatial distributions in time of w_0 (weight of all fine particles located in a y-range normalised by the overall fine particles' weight, being fine particles the ones characterised by a diameter D such that $D_0 \leq D \leq D_{10}$).

Given the soil to be treated and injection operational parameters, this numerical strategy can be employed as a useful tool for (i) predicting suffusion mechanisms prone to occur at various distances from the injection source, (ii) providing a quantification of the changes in terms of pore size distributions and k and (iii) effectively designing permeation grouting treatments. For instance, if a soil turns out to be susceptible to a significant fine fraction transport characterised by a considerable travelling distance (as in Figure 2a), to enhance grout permeation, the earlier fine particles' removal from the zone to be treated, by means of water injections, can be suggested. Conversely, when clogging zones are expected (as in Figure 2b), grout permeation is obstructed and low viscosity solutions, e.g. colloidal silica grouts, are preferred.

4. References

[1] Boschi, K. (2022). *Permeation grouting in granular materials. From micro to macro, from experimental to numerical and vice versa*. PhD Thesis. Politecnico di Milano.

[2] Chareyre, B., Cortis, A., Catalano, E., & Barthélemy, E. (2012). Pore-scale modeling of viscous flow and induced forces in dense sphere packings. *Transport in porous media*, 94, 595-615.

[3] Šmilauer, V., Catalano, E., Chareyre, B., Dorofeenko, S., Duriez, J., Gladky, A., ... & Thoeni, K. (2010). *Yade reference documentation*. Yade Documentation, 474(1).

[4] Valdes, J. R., & Santamarina, J. C. (2006). Particle clogging in radial flow: Microscale mechanisms. *SPE Journal*, 11(02), 193-198.

CONSTITUTIVE TENSOR OF GEOMATERIALS IN DISCRETE ELEMENT MODELLING FOR BIFURCATION ANALYSES

***M. Farahnak*[1], *R. Wan*[1], *M. Pouragha*[2] *and F. Nicot*[1,3]**
[1] *University of Calgary, Calgary, AB, Canada*
[2] *Carleton University, Ottawa, ON, Canada*
[3] *Université Savoie Mont Blanc, Chambéry, France*

1. Introduction

This study presents a numerical multi-scale approach to investigate instability and localization in granular materials. A multi-directional probing analysis is employed to tackle the challenge of characterizing the constitutive law in a micromechanical approach. Using the Discrete Element Modeling (DEM), multi-directional probes are performed at different material states enabling us to compute the incremental tangent (stiffness) operator that is key in continuum approaches for analyzing bifurcation in elastoplasticity [1]. A distinct constitutive tensor is obtained for each tensorial zone within the incremental loading space demonstrating a multi-linear constitutive law that describes the non-linearity arising from the direction-dependency [2]. Incorporating the proposed approach, the predicted incremental tangent operator successfully maps strain and stress increments in a piecewise manner. The instability condition is subsequently evaluated with respect to spectral characteristics of the computed constitutive tensor belonging to each tensorial zone. A meso-scale analysis is also provided to detect shear band localization and validate the well-known Rice criterion [3] as a continuum-based concept within a micromechanical discrete modeling framework.

2. Numerical approach

The proposed approach is presented within the elastoplasticity framework where the incremental tangent constitutive tensor is computed by performing a series of DEM strain probing at different material states during a plane strain test on a dense sample. By distinguishing between elastic and plastic parts of the strain increments, the least square method is invoked to obtain the incremental tangent operator from the performed strain probes such that $\mathrm{d}\boldsymbol{\sigma} = \mathbb{D} : \mathrm{d}\boldsymbol{\varepsilon}$. While a unique elastic tangent operator is computed for all the elastic probe directions, dividing the incremental loading space into tensorial zones is required to find a distinct incremental elastoplastic operator for each identified zone. The proposed approach enables us to examine the instability condition with respect to the tangent operator and the vanishing of its positive-definiteness, i.e., $\det \mathbb{D}^{sym} = 0$.

In order to detect localization, the DEM sample is divided into meso-scale cells each representing a representative elementary volume so that meso-scale stress and strain can be related through a constitutive law. For each cell, meso-scale stress and strain are calculated from microvariables. In accordance with the elastoplasticity theory, the localization criterion is given by the vanishing of the determinant of the acoustic tensor $\boldsymbol{A} = \boldsymbol{n}.\mathbb{D}.\boldsymbol{n}$, i.e., $\det(\boldsymbol{A}) = 0$ with $\boldsymbol{n}$ being the vector normal to the shear band [3].

3. Results and conclusions

Using the computed elastoplastic tangent operator for each of the tensorial zones, the predicted incremental stress response envelope for a material state close to the peak stress ratio is compared with the DEM probing results, as illustrated in Fig 1a. A very good agreement is observed when the directional non-linearity has been taken into account using the tensorial zones similar to a multi-linear constitutive function. Subsequently, the obtained elastoplastic tangent operator is investigated within

each tensorial zone such that the instability condition $\det \mathbb{D}^{sym} = 0$ is compared to the second-order work criterion calculated for incremental strains and stresses in DEM probing. Results illustrated in Fig. 1b show that the tensorial zone with the elastoplastic tangent operator satisfying the instability condition, i.e., with both probing altitude (θ) and azimuth (ϕ) angles between $\pi/2$ and π, coincides with the instability cone having negative second order work. This observation confirms the equivalence of the two instability conditions incorporating the proposed discrete to continuum approach.

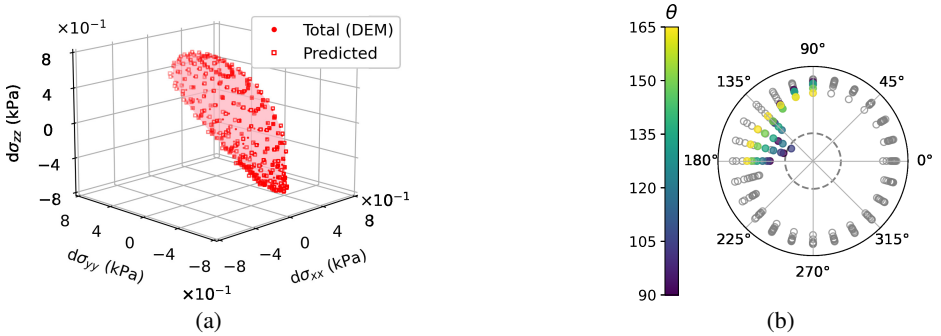

Figure 1. (a) Incremental stress response envelope, (b) normalized second order work calculated from DEM. The colored markers correspond to the tensorial zone satisfying $\det \mathbb{D}^{sym} = 0$.

In the meso-scale analysis (see Fig. 2a), the elastoplastic tangent operator is computed for each cell, and a numerical scheme searching for the normal vectors resulting in vanishing the determinant of acoustic tensor is implemented to find the shear band localization angle. Results illustrated in Fig. 2b show that Rice's criterion with the elasto-plastic tangent operator obtained from the proposed multi-scale approach, is capable of reasonably detecting the shear band orientation originally demonstrated by the deviatoric strain field derived directly from DEM simulation, i.e., Fig. 2c.

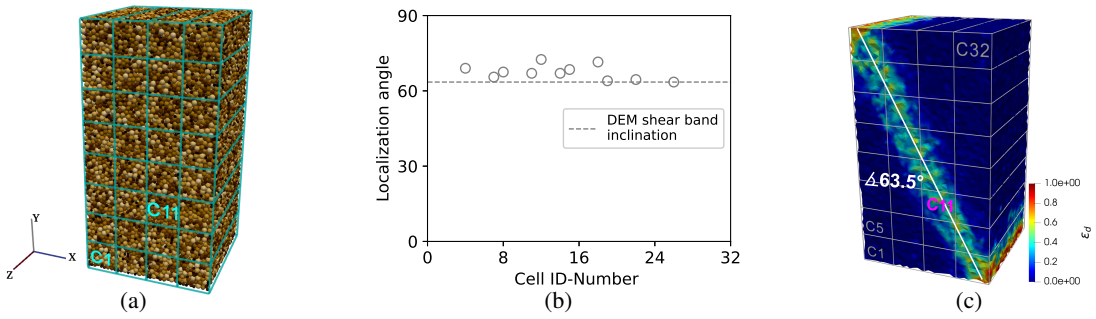

Figure 2. (a) Meso-scale cells within the DEM sample, (b) localization angle calculated by Rice's criterion for cells locating inside the shear band, and (c) deviatoric strain field in DEM simulation.

References

[1] Imposimato, S. and Nova, R. (1998). Investigation on the uniqueness of the incremental response of elastoplastic models for virgin sand. *Mechanics of Cohesive-Frictional Materials*, **3**, 65–87.

[2] Darve, F. and Labanieh, S. (1982). Incremental constitutive law for sands and clays: Simulations of monotonic and cyclic tests. *International Journal for Numerical and Analytical Methods in Geomechanics*, **6**, 243–275.

[3] Rice, J. R. (1976). The localization of plastic deformation. pp. 207–229.

A BASIC NUMERICAL MODEL FOR HYGROSCOPIC SWELLING PARTICLES

***I. Vego*[1], *V. Richefeu*[1], *A. Tengattini*[1,2] *and G. Viggiani*[1]**
[1] *Univ. Grenoble Alpes, Grenoble INP, CNRS, 3SR, F-38000 Grenoble, France*
[2] *Institut Laue-Langevin (ILL), 71 Avenue des Martyrs, 38000 Grenoble*

1. Introduction

The effects of water on the behaviour of granular materials can be significant. In granular assemblies composed of hydrophobic-impermeable particles, water affects the effective stress or it induces inter-particle capillary forces [1]. However, there are many materials where the interaction with water directly affects the properties of individual particles, *e.g.*, cereals, flour, pharmaceutical excipients [2, 3]. Even a small increase of water content can activate chemical reactions causing a relaxation of the polymer chains, and thus, for instance, an increase in size or deterioration of mechanical properties of the material [4]. These translate to particle-scale phenomena, such as swelling or deterioration of mechanical properties, which in turn influence the macroscopic response of the material. *Water-sensitive* particles can, in fact, agglomerate, altering the flow properties of the material, thus reducing the product functionality [2, 3]. All these phenomena often induce inefficiencies in the supply chain [5], which obviously raises important economical and sustainability issues. Several studies have focused their attention on the effects of water-content on the macroscopic response or the properties of individual particles [2, 3]. However, the link between particle-scale phenomena and the assembly-scale material response appears to be largely ignored in the literature [3]. That is why, more recently, experimental campaigns have been carried by this group to understand the chemo-hydro-mechanical behaviour of such materials [6]. Specifically, samples of couscous particles were exposed to high relative humidity air and subjected to constant vertical stress. The water adsorption induced particle-scale phenomena such as swelling and decrease of mechanical properties, which in turn influenced the sample-scale response, revealing a peculiar dilation-compaction behaviour. All the morphological microstructural variables were correlated to water content, which could be considered as the driving variable of the problem. No matter how rich the data-sets, the experimental observations should be supported by numerical models. Thanks to the perfect control of the boundary conditions and the possibility of quantifying variables non measurable experimentally, numerical tools are beneficial to further investigate the behaviour of water-sensitive materials. For these reasons, a novel model is being developed and implemented to digitally reproduce the behaviour of hygroscopic swelling particles.

2. The model

The model design is intentionally simple. Its goal is to capture the material response found experimentally, while limiting the number of independent variables. The purpose is not to specifically simulate a specific material, but rather to provide a tool that could be adapted to any water-sensitive material. Since the objective is to link the particle-scale phenomena to the overall response of the assembly, the discrete element method (DEM) is selected as the appropriate approach to address the problem. The often complex geometry of particles is approximated by spheres, and their kinematics is restricted to 2D. The spheres are placed in a box of four rigid walls, and only the vertical displacement of the upper wall is allowed (see Figure 1). A constant force is applied on this wall, in order to mimic realistic conditions, such as in a storage silo. The model allows for the concurrent particle dilation and the decrease of mechanical properties, a feature often ignored when modelling water-sensitive granular materials [7]. The inter-particle forces are modelled with the non-linear elastic Hertz-Mindlin model, and the Coulomb criterion limits the tangential forces. A large particle interpenetration simulates the particle deformability. No cohesion is considered in the current version of the model.

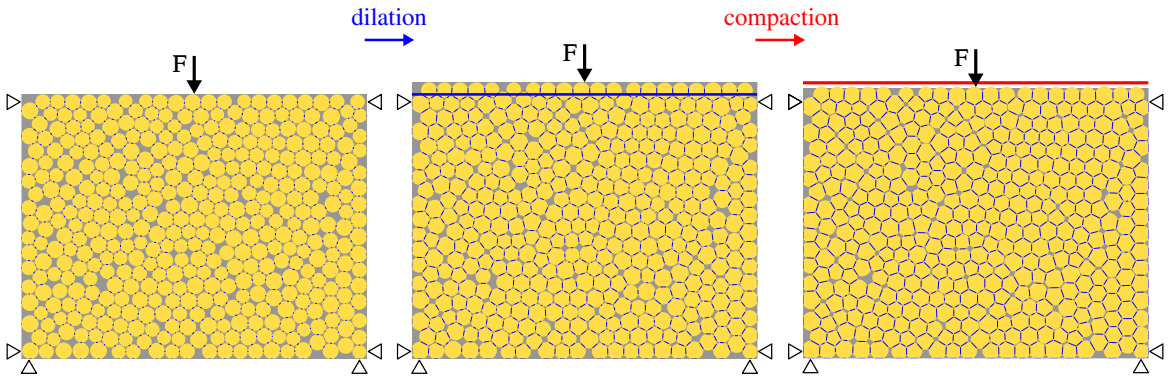

Figure 1. Dilation-compaction response of an assembly of hygroscopic swelling particles subjected to a constant force F. Initially, the swelling induces a dilation of the system. Eventually, for higher water particle, when the particles become softer, the assembly is compacted by the constant vertical load applied.

3. Results and conclusions

Preliminary sensitivity studies have been carried out to verify the validity of the model, as well as to explore the effects of variables that could not be controlled (load or relative humidity) or measured (inter-particle forces) during the laboratory tests [6]. The input parameters were calibrated according to experimental observations [6]. Naturally, because of the geometrical restrictions, it was not possible to quantitatively compare the response of the assembly to that measured in the experiments. However, despite being at a preliminary stage, the newly developed model could reproduce some feature measured experimentally: a dilation-compaction response (Figure 1), a linear free-swelling response (zero vertical load) of the system with increasing water content, and a coherent quadratic growth of contact areas, that was measured experimentally [6].

Further improvements of the model will involve removing the 2D restrictions, accurately modelling the particle shape, including in the model particles cohesion, and accounting for water content (thus swelling) heterogeneities.

References

[1] Fredlund, D. G. and Rahardjo, H. (1993). *Soil mechanics for unsaturated soils*. John Wiley & Sons.

[2] Aguilera, J., del Valle, J., and Karel, M. (1995). Caking phenomena in amorphous food powders. *Trends in Food Science & Technology*, **6**, 149–155.

[3] Zafar, U., Vivacqua, V., Calvert, G., Ghadiri, M., and Cleaver, J. S. (2017). A review of bulk powder caking. *Powder Technology*, **313**, 389–401.

[4] Damodaran, S. and Parkin, K. (2017). *Fennema's Food Chemistry (5th ed.)*. CRC press.

[5] Chauhan, C., Dhir, A., Akram, M. U., and Salo, J. (2021). Food loss and waste in food supply chains. a systematic literature review and framework development approach. *Journal of Cleaner Production*, **295**, 126438.

[6] Vego, I. (2023). *Multi-modal investigation of hygroscopic granular media at high relative humidity*. Ph.D. thesis, Université Grenoble Alpes.

[7] Sweijen, T., Chareyre, B., Hassanizadeh, S. M., and Karadimitriou, N. (2017). Grain-scale modelling of swelling granular materials; application to super absorbent polymers. *Powder Technology*, **318**, 411–422.

COMPUTATIONAL MODELING OF MULTIPHASE FLUIDS INTERACTING WITH IRREGULAR-SHAPED GRANULAR PARTICLES

J. Zhao[1,2], Z. Lai[1] and S. Zhao[1]

[1] The Hong Kong University of Science and Technology, Hong Kong SAR, China

[2] HKUST Shenzhen-Hong Kong Collaborative Innovation Research Institute, Shenzhen 518045, China

1. Introduction

Fluid-particle interactions underpin the operation and performance of key civil infrastructure. Internal erosion in earth dams, rock armor for coastal protection, and debris flows are typical examples. Coupled computational fluid dynamics and discrete element method (CFD-DEM) has been a prevailing method for the simulation of fluid-particle interactions [1]. Unresolved CFD-DEM coupling and spherical particles with empirical interaction force models are dominantly used. This study presents a new fully resolved coupled CFD-DEM based on the signed distance field (SDF) and immersed boundary method (IBM) to fully consider arbitrarily shaped granular particles interacting with multiphase fluids. The IBM is adapted to be consistent with the SDF to fully resolve fluid-particle interactions for an irregular shaped particle. Basic formulations and benchmark examples are presented.

2. Fully resolved CFD-DEM based on SDF and IBM

A signed distance field (SDF) description of particle uses a function $d = \Phi(x): \mathcal{R}^3 \rightarrow \mathcal{R}$ to map a point x to a signed value d, as illustrated in Fig. 1a. A SDF-based interface provides the signed distance at a query point, defined positive if the point is inside the particle surface and negative otherwise, and a surface projection function to define its projection onto a particle surface. Associated particle properties, including mass and moment of inertia, are calculated from the reconstructed triangular mesh from the particle surface. Fig. 1c shows a DEM packing of irregular particles generated based on SDF [2].

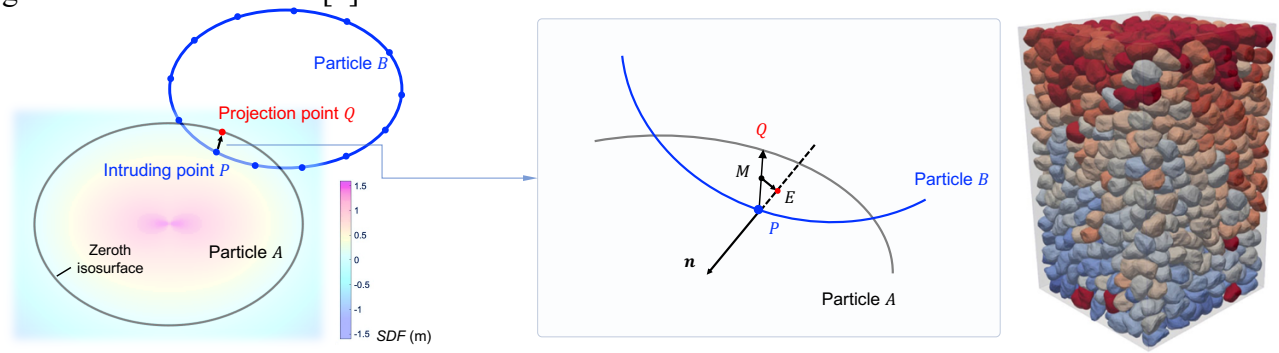

(a) (b) (c)

Fig. 1 (a) SDF particle model, (b) node-to-surface contact detection in SDF, and (c) DEM simulation of triaxial compression of irregular particle sample.

The CFD solves the continuity equation and the NS equation that are formulated to consider air-liquid two phase fluids. The immersed boundary method in the CFD assume a fictitious CFD domain for the space occupied by the DEM particles to evaluate the forces exerted from the fluids to the particles (see Fig. 2a) and add the calculated forces as extra terms to the Navier-Stokes equation for CFD solution. The SDF formulation enables rigorous consideration of the surface tension at the interface of solid and multiphase fluid based on novel cell-based node searching algorithm for solid fraction field (see Fig. 2b) [3]. Fig. 3a presents a demonstrative simulation of the collision of two

particles with irregular shapes (top) in comparison with spheres (bottom). Fig. 3b shows the resolved CFD-DEM simulation of a mudflow erodes flow bed with irregular shaped granular particle.

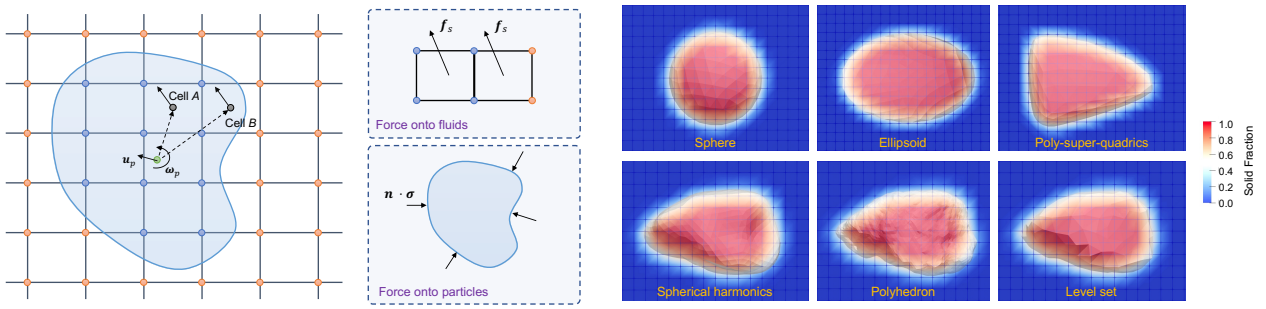

(a) (b)

Fig. 2 (a) IBM for fluid-particle interaction and (b) demonstration of SDF-based estimation of solid field for different particles.

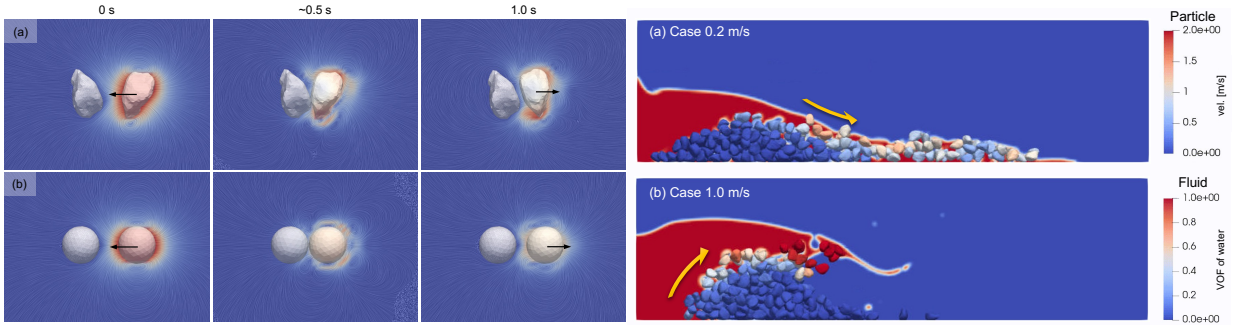

(a) (b)

Fig. 3 (a) Particle collision in water and (b) Mudflow erosion of granular particles.

3. Conclusions

We presented a signed distance field based fully resolved CFD-DEM for modeling of the interactions between multiphase fluids and arbitrarily shaped granular particles which are important to a wide range of engineering problems. Immersed boundary method in the CFD is adapted to be consistent with the SDF for consideration of the fluid-particle interactions. Demonstrative examples show the method can faithfully capture key mechanics and physics underpinning the interactions.

4. Acknowledgements

This work was supported by National Natural Science Foundation of China (by 11972030), Research Grants Council of Hong Kong (by GRF Projects No. 16211221 & No. 16208720, and F-HKUST601/19), and the Project of Hetao Shenzhen-Hong Kong Science and Technology Innovation Cooperation Zone (Grant No. HZQBKCZYB-2020083). J Zhao acknowledges the financial support of HKUST internal supports thorough FP907 and IEG22EG01.

5. References

[1] Zhao, J.D. & Shan, T. (2013). Coupled CFD-DEM simulation of fluid-particle interaction in geomechanics. *Powder Technology*. 239, 248-258.

[2] Lai Z.S., Zhao S.W., Zhao J.D. & Huang L.C. (2022). Signed distance field framework for unified DEM modeling of granular media with arbitrary particle shapes. *Computational Mechanics*. 70: 763–783.

[3] Lai Z.S., Zhao J.D., Zhao S.W. & Huang L.C. (2023). Signed distance field enhanced fully resolved CFD-DEM for simulation of granular flows involving multiphase fluids and irregular-shaped particles. *Computer Methods in Applied Mechanics and Engineering*. Under review.

HYDRAULIC FRCTURING PROCESS IN ROCKS – SMALL SCALE SIMULATIONS WITH A NOVEL MESOSCOPIC THERMO-HYDRO-MECHANICAL APPROACH

M. Krzaczek and J. Tejchman
Gdańsk University of Technology, Gdańsk, Poland

1. Introduction

Hydraulic fracturing (HF) is a major technique (developed steadily since 1947) for increasing the productivity of petroleum, gas, or heat in low-permeability rock formations. HF enables the economic extraction of petroleum/gas/heat from rocks that have a permeability of less than 10^{-16} m^2. By pumping a significant amount of pressurized fluid at a pressure of about 70 MPa into a wellbore, this technique fractures rocks at a target depth of roughly 2-6 km, causing either cracks in the deep-rock formations or strengthening the connectivity of the pre-existing fracture network, allowing natural gas, petroleum, and heat to flow more freely by exceeding the pressure gradient of rocks. This technology uses horizontal wellbores because they offer a far larger exposure to a formation than traditional vertical wellbores. A slurry of water, proppant (sand), and chemical additives called hydraulic fracturing fluid is frequently used to open and enlarge cracks in rock formations. Small grains of hydraulic fracturing proppants keep the cracks open when the hydraulic pressure is released from the well. At a continuous rate of around 2 m^3/s, fluid is injected. The gas extraction from deep shale layers is now at about 5-15%. This percentage is still very high in the face of extremely low shale permeability. It means that during HF the rock permeability must be significantly increased by both opening already-closed cracks (that follow the rock joint and slide fault network) and initiating brand-new hydraulic cracks in intact shales. The overall permeability is enhanced by dense networks of branched cracks that HF creates, whose spacing and opening width are sufficient. Since the precise geometry of subsurface cracks is still unknown, most of the understanding of the fracturing process is empirical. The laboratory tests described in [1] demonstrated a significant influence of injection rates and fluid viscosities on fracture branching patterns.

Testing the propagation of fracture networks in situ and at the laboratory scale is difficult. Therefore, it is essential to construct a realistic numerical model to comprehend and describe the rock crack phenomenon during the development of hydraulic fracturing and to optimize it for enhancing a gas extraction (e.g. by changing the pumping rate/cycles and fluid viscosity) for overcoming partly the shortages of experimental methods. Numerical simulation studies are, thus, necessary to increase the efficiency of HF. There are, however, a number of challenging problems that must be solved in simulations, including e.g. coupling strategy between the solid and fluid domain and remeshing process (data transfer from the old mesh to the new mesh) induced by significant solid deformation caused by fluid pressure, multi-phase flow and thermal strains.

2. Research aims

The paper aims to quantitatively illustrate the effect of the injected fluid temperature, the fluid dynamic viscosity (dependent upon temperature), and the gas content in macro-pores on the evolution of a hydraulic fracture, fluid/gas pressures, and velocities during a small-scale hydraulic fracturing process in rock specimens under two-dimensional (2D) conditions For non-saturated porous materials with very low porosity, a unique DEM/CFD-based thermal-hydro-mechanical technique of pressurized fracturing laminar viscous fluid flow of a variable temperature containing liquid and gas was devised [2]. Heat transfer involved both the fluid (diffusion and advection) and

cohesive granular particles (conduction). Numerical 2D THM mesoscopic computations were performed utilizing a DEM along with fluid flow and heat transfer. By using discrete spherical elements interacting through elastic-brittle normal contacts that could break to cause fractures, DEM was used to depict the mechanical behaviour of the rock mass. Laminar viscous two-phase (water and gas) fracturing fluid flow through pores and cracks in a continuous domain between the spherical discrete elements was described using CFD (where a flow network made up of channels was adopted). Small-size cohesive granular specimens imitating rock under plane strain compression were subjected to THM calculations in non-isothermal settings. In the first estimate, the rock specimen consisted of spheres of different diameters with no pre-existing micro-cracks/faults/bedding layers and with a single injection slot. The effects of the temperature difference between the rock matrix and the fluid being injected, the fluid's dynamic viscosity, and the amount of gas present in the rock matrix on the initiation and spread of a single hydraulic fracture were the next factors to be examined in-depth in a series of small-scale hydraulic fracturing simulations. This article is a follow-up to the authors' earlier small-size mesoscopic studies on hydraulic fracturing in rock segments [3], [4], which utilized and extensively discussed a 2D fully coupled DEM/CFD technique without heat transfer. Here, a novel mathematical THM model was applied [4] that took additionally into account heat transfer in both rock mass and fracturing fluid.

3. Conclusions

The impact of the temperature difference between the rock matrix and the injected fluid on the hydraulic fracture shape was visible. The fluid temperature difference between the bottom and the top of the fracture strongly increased with the initial temperature of the rock matrix. The lowest density of both phases decreased with increasing rock matrix temperature. Advection strongly dominated the energy transport in the fluid; it was significantly higher than the diffusion energy.

For the low dynamic viscosities of the injected fluid, the hydraulic fracturing process lasted shorter and the hydraulic fracture shape was, thus, more vertical. The maximum temperature difference between the fluid and the rock matrix was higher for the high dynamic viscosity above the injection point and lower at the injection point.

The greater the initial content of the gas phase in the rock matrix, the more curved the hydraulic fracture, the significantly slower the hydraulic fracture propagation velocity, and the greater the fluid temperature reduction in the hydraulic fracture. The heat exchange between the fluid and solid was more intense for the high initial gas content, and the grains surrounding the fracture were then strongly cooled.

The development of thermal cracks may contribute to a noticeable increase in crack branching, leading to rock permeability growth.

4. References

[1] Li, W.F., Frash, L.P., Carey, J.W., Welch, H.J., Meng, M., Nguyen, H., Viswanathan, H., Rougier, E., Lei, Z., Rahimi-Aghdam, S. & Bazant, Z.P. (2021). Injection Parameters that Promote Branching of Hydraulic Cracks, *Geophys. Res. Lett*., **48** (12) e2021GL093321.

[2] Krzaczek, M., Nitka, M. Tejchman, J., (2022). A novel DEM-based pore-scale thermal-hydro-mechanical model for fractured non-saturated porous materials, *Acta Geotechnica* 10.1007/s11440-022-01746-8.

[3] Krzaczek, M., Kozicki, J., Nitka, M., Tejchman, J. (2020). Simulations of hydro-fracking in rock mass at meso-scale using fully coupled DEM/CFD approach, *Acta Geotechnica* **15**, 297-324.

[4] Krzaczek, M., Nitka, M. & Tejchman, J. (2021). Effect of gas content in macropores on hydraulic fracturing in rocks using a fully coupled DEM/CFD approach, *International Journal for Numerical and Analytical Methods in Geomechanics* **45**(2) 234-264.

RAY-TRACING DISCRETE ELEMENT MODELING AND IN-SITU VISUALIZATION OF GEO-HAZARDS

S. Zhao and J. Zhao
The Hong Kong University of Science and Technology, Hong Kong SAR, China

1. Introduction

In-situ visualization of geo-hazards such as landslides and debris flows has never been so urgent for the coming era of Big Data and Artificial Intelligence (AI), which is helpful for engineers to use a digital system such as Metaverse to make real-time decisions and mitigate the risk. The in-situ visualization can be implemented using a ray-tracing (RT) technique fed by the synchronized simulation data obtained from a direct numerical simulation (DNS) or machine learning. A recent study [1] employed a DNS approach based on material point method (MPM) in conjunction with a CPU-based RT engine to in-situ visualize a landslide. This study presents a DNS scheme based on discrete element method (DEM) to model landslides, where the RT technique is seamlessly applied to accelerating DEM simulations on graphic processing units (GPUs). Therefore, both simulation and visualization can be fully accelerated with shared data by using the RT hardware on RTX GPUs of NVIDIA.

2. Ray-tracing discrete element modeling

Ray tracing is a prevailing technique to render images and videos with extra realism in computer graphics. During rendering, the color of each pixel is determined by casting a ray into a model scene. The model scene most often consists of a large number of objects, and it is computationally intensive to query a collision between a ray and all potentially touching objects. The physical RT unit was invented by NVIDIA to tackle ray-object collision on GPUs [2]. Attracted by the powerful RT unit, researchers managed to apply RT cores to general-purpose scientific computing beyond ray-tracing tasks, e.g., [3]. The authors also applied the RT unit to accelerate particle-based numerical simulations in their recent work [4].

To leverage the powerful RT cores for DEM simulations, the neighbor searching procedure needs first transferring to an equivalent RT problem. Then, an imaginary short ray is cast into the model scene that has all particles organized in an accelerate structure. Next, the interparticle contact detection is identified by checking whether the cast ray is inside the expanded axis-aligned bounding box (AABB) of a neighboring particle, cf. Fig. 1a. Such a ray-AABB collision detection is fully accelerated by the RT cores with an NVIDIA's OptiX pipeline as shown in Fig. 1b. Interested readers are referred to [4] for more details on the implementation.

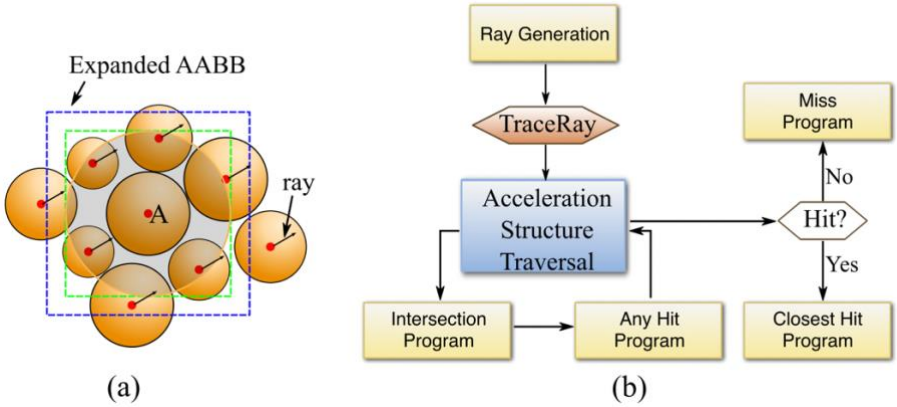

Fig. 1 (a) Ray-tracing neighbor search, (b) a ray-tracing pipeline in OptiX 7.

3. Particle-terrain contact detection

In the RT-DEM-based DNS scheme, a terrain is modeled by a digital elevation model, and soil particles are simplified as spheres. It is assumed that particles are smaller than the grid size of the digital elevation model to ease the particle-terrain contact detection. Thus, a particle has at most 4 grid cells (8 triangular facets) that can be identified efficiently by indexing its coordinates with respect to the regular grid cells. Moreover, a weighting scheme is applied to contact force when a particle touches with adjacent triangles, which ensures robust sliding of a particle across cells.

4. Numerical simulation

A landslide is simulated with the proposed RT-DEM framework. The terrain is built with a digital elevation model composed of around 0.12 M triangular facets, while the release region is made up of around 1.6 M particles with radii of 0.125 m, cf. Fig. 2a. The detailed simulation setup follows our previous work [4]. The sliding simulation lasts for 100 s with visualization snapshots shown in Fig. 2 b&c, where the colormap shows the elevation of particles. As reported in our work [4], a 100-second simulation of a sliding takes only 6.5 min on a single NVIDIA RTX 3090 GPU. Note that both RT-DEM and visualization are implemented with OptiX.

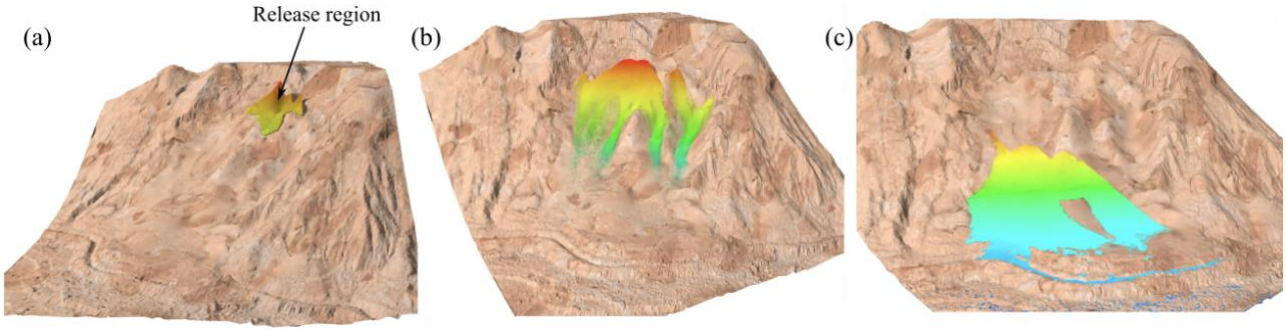

Fig. 2 Visualization of a landslide at a time instant of (a) 0 s, (b) 10 s and (c) 100 s.

5. Conclusion

The proposed DNS scheme can seamlessly combine the computation of DEM simulation and in-situ visualization, where the interparticle contact detection in DEM shares the same data with the ray-tracing collision detection in visualization. The proposed scheme can be fully accelerated with the modern GPUs with ray-tracing (RT) cores, which can be a promising approach for next-generation computing tools in modeling of geo-hazards with in-situ visualization.

6. Acknowledgements

This work was supported by Research Grants Council of Hong Kong (by GRF Projects No. 16211221 & No. 16206322), and the Project of Hetao Shenzhen-Hong Kong Science and Technology Innovation Cooperation Zone (Grant No. HZQBKCZYB-2020083).

7. References

[1] Abram, G., Solis, A., Liang, Y., & Kumar, K. (2022). In situ visualization of regional-scale natural hazards with Galaxy and Material Point Method. *Comput. Sci. Eng.*, *24*(2), 31–39.

[2] NVIDIA. NVIDIA Turing GPU architecture: graphics reinvented; 2018. https://bit.ly/2NGLr5t

[3] Wald I., Usher W., Morrical N., Lediaev L. & Pascucci V. (2019). RTX beyond ray tracing: exploring the use of hardware ray tracing cores for tet-mesh point location. *High Perform. Graph. (HPG)*. 7-13.

[4] Zhao, S., Lai, Z., & Zhao, J. (2022). Leveraging ray tracing cores for particle-based simulations on GPUs. *Int. J. Numer. Meth. Eng.*, **124**(3), 696–713.

5. Application of numerical techniques to practical problems

ARCHING STRESS DISTRIBUTION IN EMBANKMENTS CONSTRUCTED ON PILED SOFT SOILS

R.L. Michalowski[1] and K. Brzeziński[2]
[1]University of Michigan, Ann Arbor, U.S.A.
[2]Warsaw University of Technology, Poland

Soil arching

Soil arching is an elusive phenomenon, associated with non-uniform compliance of the supporting structure. Design of embankments on soft soils reinforced by piles makes use of this phenomenon to predict the partition of the load between the piles and the soft soil. An early attempt to quantify this partition is owed to Hewlett & Randolph [1], who suggested that there is a formation of dome-shape features within the embankment fill, resting on a system of piles or columns, transferring the bulk of the load to the stronger layers of underlying soil. The mechanism of load transfer appears to be interesting; it can be characterized as a distributed or *diffused arching*, driven by the difference in compliance of the pile support and the soft soil between the piles.

Stress and deformation in embankments resting on a pile support system

A schematic of a cross-section through a sand embankment supported by piles capped with beams (half of a periodic cell) is illustrated in Fig. 1(a). The density of the embankment fill is taken at 1900 kg/m^3, Young's modulus 60 MPa, and Poisson's ratio 0.3. Plastic deformation is described by non-associative Mohr-Coulomb model with internal friction angle 40° and dilatancy of 10°. While the major principal stress trajectories form an arch-like shape, Fig. 1(b), the stress distribution provided no evidence that a hypothetical arch with elevated stress actually forms [2].

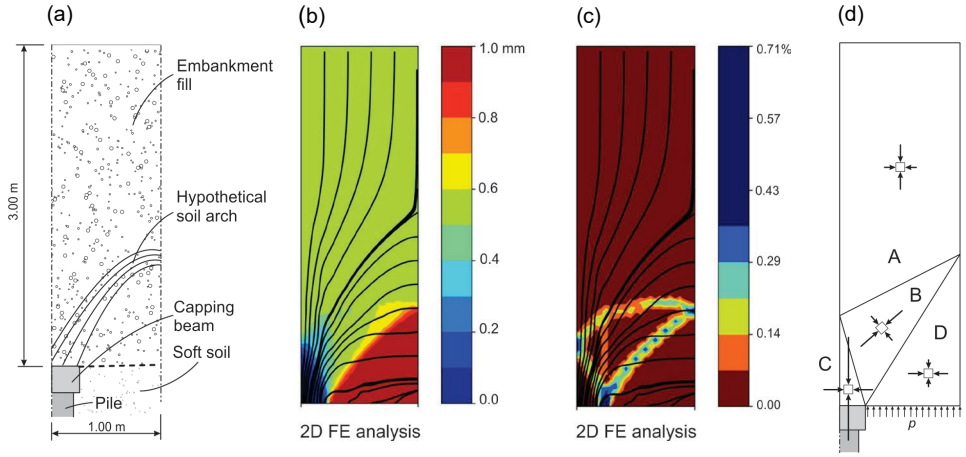

Figure 1. (a) Half of embankment periodic cell (2D), (b) vertical displacements with trajectories of major principal stresses, (c) maximum shear strain increment in plastic mechanism, and (d) schematic of admissible stress field.

An interesting feature of the strain field is the trap-door type plastic mechanism forming in the lower part of the embankment [2], with the process driven by the settlement of the soft soil, Fig. 1(c). Inspection of the stress field did not reveal any arching-type features above the mechanism, though a distinct transfer of the major portion of the load to the pile caps took place.

Calculations for a 3D model with piles distributed in a square grid pattern, Fig. 2(a), revealed similar features as found in the 2D simulations. The white regions in Figs. 2(b) and (c) indicate major principal stresses being off the color scale; above the scale when bordering with red, and

below when bordering with blue. The graph indicates the transfer of a considerable portion of the embankment load to the pile. A surprising outcome of these computations is the monotonic distribution of the major principal stress along the minor principal stress trajectories, indicating no traces of the type of arching often considered in design methods.

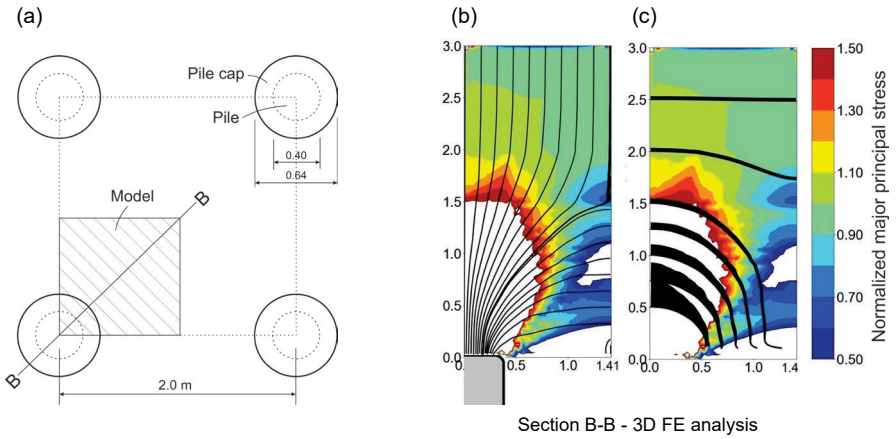

Figure 2. (a) Top view of the 3D periodic cell, (b) major principal stresses (normalized) and major principal stress trajectories, and (c) magnitudes of major principal stresses illustrated by thickness of the black bands (section B-B).

Efficacy of the pile support system

The efficacy of the pile support system is defined as the ratio of the load transferred to the piles to the total load within a single computational cell. This efficacy depends significantly on the properties of the embankment fill, embankment height, and the settlement of the soft soil. While this measure of performance can be deduced from numerical (*e.g.*, FEM) calculations, it can also be considered using the plasticity static collapse theorem, with the following formulation: Given the embankment height and spacing of piles, what is the minimum support stress p (Fig. 1(d)) for which an admissible stress field can be found? The stress field is indicated schematically in Fig. 1(d). Stress discontinuities separate regions A through D; stresses change with depth, but principal stress directions do not change with depth in regions A, C, D; however, they do change with depth in region B. Efficacy calculated for a 5-m tall embankment with pile spacing of 2.0 m was found to be 0.905 using the FEM approach [2] and 0.902 when using the static collapse theorem (Fig. 1(d)).

General remarks

Numerical simulations of the stress state in embankments placed above pile-reinforced soft soils did not reveal arch-like features in the stress field, but they confirmed distributed transfer of the major portion of load to the piles. This transfer is characterized by diffused features with monotonically increasing stresses, rather than arches with concentrated stresses, typically used to visualize soil arching. Both finite element simulations and limit analysis were found useful in estimating the efficacy of the pile support system.

Acknowledgement

The work summarized in this abstract was supported by the National Science Foundation, Grant No. CMMI-1901582. This support is greatly appreciated.

References

[1] Hewlett, W. J. & Randolph, M. F. (1988). Analysis of piled embankments. *Ground Engineering*, **21**(3), 12-18.

[2] Brzeziński, K. & Michalowski, R. L. (2021). Diffused arching in embankments supported by non-compliant columns with capping beams. *Comput. Geotech.*, **132**, 104031.

PERMEABLE WALLS FOR MITIGATING FAST DEBRIS FLOWS: A TWO-PHASE TWO-LAYER DEPTH-INTEGRATED SPH-FD MODELING

S.M. Tayyebi, M. Pastor, A. Hernandez, L. Gao, and M.M. Stickle
E.T.S.I. Caminos Canales y Puertos, Universidad Politécnica de Madrid, Spain

1. Introduction

The debris flow's behavior depends on the properties of flowing mass (solid and fluid phases) and basal surface, including resistance to erosion and permeability, which can cause pore pressure dissipation and dewatering. This technique can also be used to reduce the runout distance and propagation velocity of debris flows, using structural countermeasures such as permeable walls and permeable screens, which retain the solid fraction while leaving the water to pass through them. In this paper, we will present a numerical model, capable of considering the saturated and unsaturated hydro-mechanical behavior of landslides.

2. Proposed two-phase model

A two-phase coupled model [1,2] is applied to capture the dynamic of solid and fluid phases. The governing equation consists of two depth-integrated balance equations that describe the propagation of phases and a consolidation equation which describes the evolution of excess pore-water pressure along the vertical axis in a depth-integrated model, i.e.

$$\frac{\bar{d}^{(\alpha)}h_\alpha}{dt} + h_\alpha \mathrm{div}\bar{v}_\alpha = \bar{n}_\alpha e_R \tag{1}$$

$$\frac{\bar{d}^{(s)}\bar{\boldsymbol{v}}_{\boldsymbol{\alpha}}}{dt} = \frac{1}{h_\alpha}\mathrm{grad}P_\alpha + \frac{1}{h_\alpha}F_\alpha \mathrm{grad}\bar{n}_\alpha + S_\alpha \tag{2}$$

$$\frac{d^{(s)}\Delta p_w}{dt} = -\bar{\rho}_d^{'} b_3 \frac{d^{(s)}h}{dt} + c_v\left(\frac{\partial^2 \Delta p_w}{\partial x_3^{\,2}}\right) - E_m \frac{1}{1-\bar{n}}\frac{d^{(s)}\bar{n}}{dt} \tag{3}$$

where, in the two-phase model, each phase is characterized by its density (ρ), depth-averaged flow velocity $(\bar{\boldsymbol{v}})$, height (h) and averaged porosity $(\bar{n})$. The subscript α denotes the solid or fluid phase, $\Delta\bar{p}_w$ is the excess pore-water pressure and e_R an erosion coefficient. Moreover, P_α is the pressure acting on phases, F_α is a multiplier of porosity variation and S_α is the source term, c_v is a consolidation coefficient, $\bar{\rho}_d^{'}$ is the effective density and E_m is the oedometric modulus.

The resulting differential equations are discretized in time with the 4th-order Runge Kutta method in the Smoothed-Particle Hydrodynamics (SPH) and the Forward Time Centered Space (FTCS) method in the finite difference method.

The consolidation and dewatering times, respectively, are defined as:

$$T_{cons} = \frac{h^2}{c_v} \qquad T_{dew} = \frac{h}{\bar{k}_w} \tag{4}$$

where $\bar{k}_w$ is the hydraulic conductivity. The higher the soil permeability, a higher rate of dewatering can be achieved.

In this study, permeable walls are introduced to stop the flow. The wall boundary conditions are introduced by defining sets of special particles at wall locations. Permeable walls allow the water to flow through them and contribute to dewatering. They can be modeled simply by imposing the zero-normal velocity only on solid nodes.

3. Numerical results

In this study, we have considered a general case where the total height h is divided into three layers. The partial heights of solid (h_s), fluid (h_w), and air (h_a) are depicted in Figure 1(*a*). In the first simulation (see Figure 1(b)), the potential of the proposed model to reproduce the propagation of a debris flow contained between two permeable walls is evaluated. Figure 1(b-1) shows the initial conditions of the dam break problems over a horizontal plane. The two-phase material with a height of 10 m is contained between two permeable walls. The flowing material is fully saturated at the initial time and allowed to liquefy. Figure 1(*b*) shows that these permeable walls allow the water to pass through. Once the porosity $(\bar{n})$ reaches its low limit $(\bar{n}_{min})$, the upper part of the sliding mass will be unsaturated. Relative height (α) and total height (h) can be computed as:

$$\alpha = \frac{1-\bar{n}_{min}}{\bar{n}_{min}}\frac{h_w}{h_s} \qquad h = \frac{h_s + h_w}{\left[1-\bar{n}_{min}\left(1-\alpha\right)\right]} \tag{5}$$

Figure 1(c) shows the simulation results of an inclined dam-break case. The numerical results show that applying a two-phase model implementing desaturation to simulate debris flows equipped with permeable walls or screens is essential to capture the realistic behavior of solid and fluid phases, and their interaction with permeable walls.

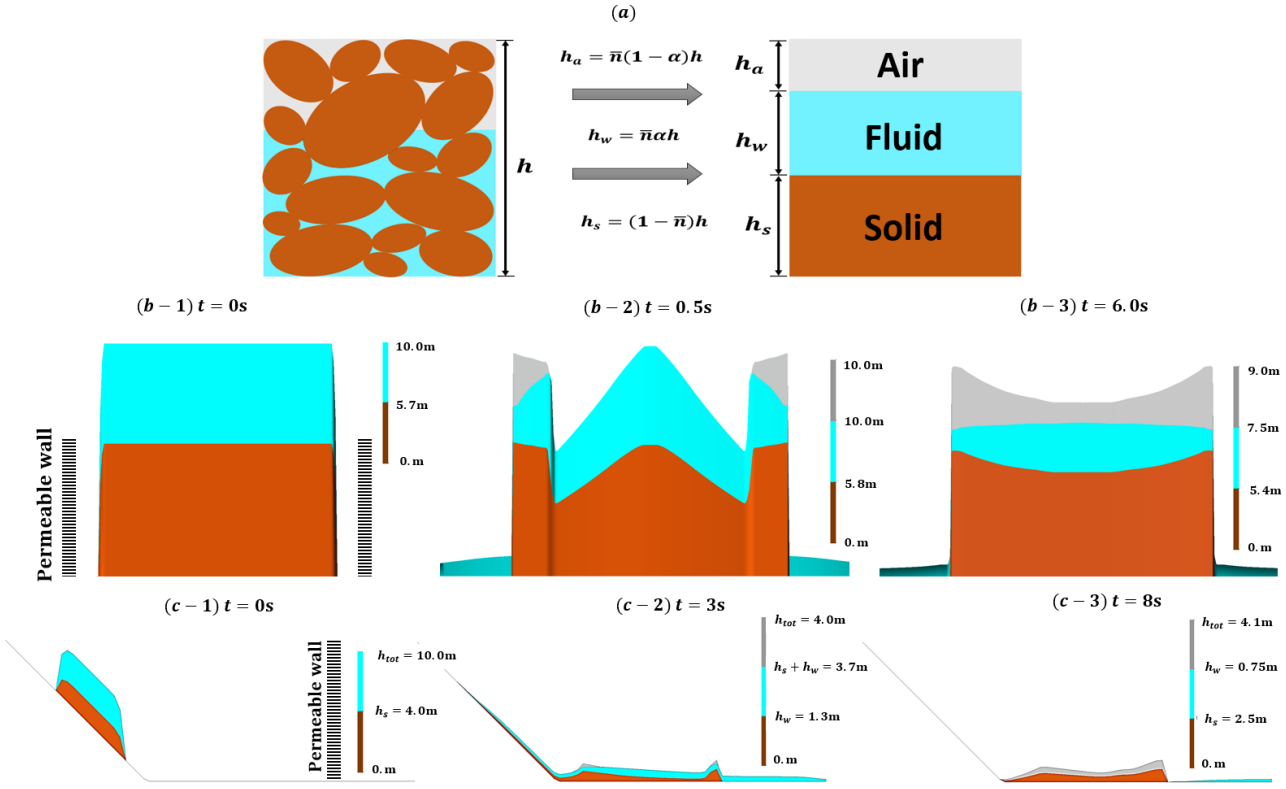

Figure 1. (*a*) Magnitudes characterizing the partially saturated debris flow components. (*b*) A debris flow contained between two permeable walls. (*c*) An inclined dam-break with a permeable wall.

4. References

[1] Pastor, M., Tayyebi, S.M., Hernandez, A., et al. (2023). A New Two-Layer Two-Phase Depth-Integrated SPH Model Implementing Dewatering: Application to Debris Flows. *Computers and Geotechnics*, 153.

[2] Tayyebi, S.M., Pastor, M., Hernandez, A., et al. (2022). Two-Phase Two-Layer Depth-Integrated SPH-FD Model: Application to Lahars and Debris Flows. *Land* **11**(10): 1629.

NUMERICAL ANALYSIS OF SEEPAGE IN THE OBERNBERG LANDSLIDE DAM

R. Shafieiganjeh[1], B. Schneider-Muntau[2], M. Ostermann[3] and B. Gems[1]
[1] Unit of Hydraulic Engineering, University of Innsbruck, Innsbruck, Austria
[2] Unit of Geotechnical and Tunnel Engineering, University of Innsbruck, Innsbruck, Austria
[3] GeoSphere Austria, Vienna, Austria

1. Introduction

Landslide dams are formed as the result of a natural blockage of river valleys by mass movements. They consist of a heterogeneous mass of unconsolidated earth and rock materials with no engineered water barrier, a filter zone to prevent piping, and a drained zone to control pore pressure [1]. In this research, the potential of piping failure is analyzed for the Obernberg landslide dam in Austria by numerical modeling. Obernberg rock avalanche is dated 8.6 ka and the formed lake due to the event is still existing. The lake is subjected to seasonal fluctuations, hence a transient seepage analysis is conducted. The main aims of this modeling are to obtain a general idea of the requirements for the landslide dams' numerical modeling and to assess the seepage effects on the stability and deformation of the dam.

2. Material and methods

The methodology applied in this research is a combination of field surveys, data measurements, laboratory experiments, and numerical modeling. To accurately simulate seepage through the dam, the hydraulic boundary conditions of the dam area including lake level fluctuation and flow velocity at the dam's outlets are measured. Samples are taken from the rock avalanche deposit and the dam materials are analyzed for grain size distribution, the coefficient of permeability, stiffness, and shear strength parameters. Using these data, a numerical model is designed in Plaxis 3D. The model consists of a permeable and coarse-grained layer at the top as rock avalanche debris, a finer and less permeable layer as alluvium, and a bedrock layer. The lake is modeled as an inactive material inside the rock avalanche debris, in which the phreatic level follows a custom water level corresponding to the lake level. The constitutive model 'hardening soil' is used as it is capable of accurately simulating the stress-induced pore pressure evolution [2]. The material parameters of the model are presented in Table 1.

Table 1 Material properties used in the numerical model

Layer	γ_{unsat} (kN/m^3)	c' (kN/m^2)	φ'	E_{50}^{ref} (kN/m^2)	E_{oed}^{ref} (kN/m^2)	E_{ur}^{ref} (kN/m^2)	ν_{ur}	ψ	k (cm/s)	Drainage type
Landslide	21.5	75	41	1E5	0.5E5	5E5	0.3	7	5.2E-2	Drained
Alluvium	21	58	40	3.4E4	1.7E4	1.7E5	0.3	0	3.4E-5	Undrained
Bedrock	20	17000	50	2.5E7	1.25E7	12.5E7	0.2	0	1.2E-7	Drained

γ_{unsat} = Unsaturated unit weight; c' = cohesion; φ' = Friction angle; E_{50}^{ref} = Secant reference stiffness modulus; E_{oed}^{ref} = Secant reference oedometer stiffness modulus; E_{ur}^{ref} = Unloading-reloading reference stiffness modulus; ν_{ur} = Poisson's ratio; ψ = Dilatancy angle; k = Permeability

To assess the seepage into the dam, various rates/ratios in terms of drawdown and filling of the lake were considered. Different ratios reflect the variation of the lake level (L) relative to the whole depth (H) (L/H=0.2, 0.4, 0.6, 0.8, 1). The drawdown and filling rates are defined as the relation between the lake level changes and time (L/time= 1, 0.5, 0.1, 0.05 m/day). A fully-coupled flow deformation analysis was conducted to compute displacements and discharge in a specific time interval. In addition, the factor of safety for the dam area was calculated using the strength reduction method.

3. Results and discussion

The variations of discharge, displacement, and factor of safety (FoS) at the dam's down-faced slope as a result of a transient seepage are shown in Figure 1. Regardless of the drawdown and filling duration (rate= L/time), the discharge out of the dam is constant under the low lake level changes (ratio of 0.2). As the ratio grows, a difference is observable between low and high rates. For drawdown scenarios, the drop in the discharge happens slowly at higher rates as the rate in the soil medium and the external water level are not the same. Following the rise in the lake, the discharge increases at lower rates which indicates the increase in the relative permeability of the soil in the dam's outlets. The displacement of the down-faced slope of the dam is rather small and its trend follows the rate. As the rate decreases, the dam material densifies and displacement reaches a constant value. The FoS is also changing depending on the rate and reaches a minimum for higher rates (> 0.7) during the drawdown. As the lake level drops and the dam's material settles, the FoS increases. In the case of a rise in the lake level, the FoS is at its lowest when the lake infills at a low rate. This is due to the increase of relative permeability in the outlets over the longer duration (lower rate).

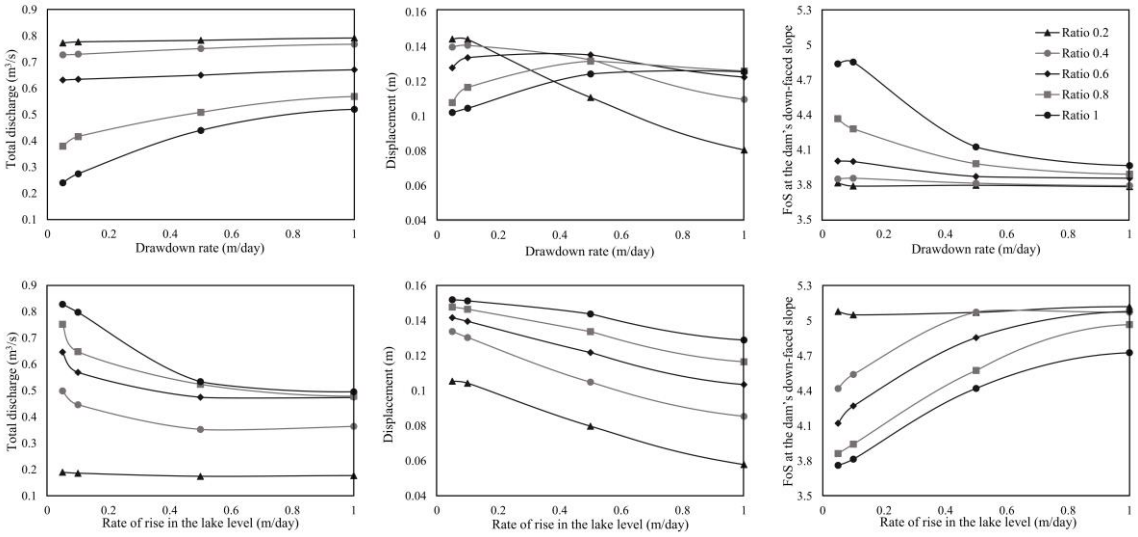

Figure 1 Results of numerical modeling of the dam under the transient seepage condition

4. Conclusions

This research aims to assess the seepage into a landslide dam by means of a coupled finite element analysis. Based on the numerical modeling outcomes, the development of the seepage path depends highly on the soil permeability and hydraulic gradient. Nevertheless, the flow velocity out of the dam and displacements are particularly affected by the duration of drawdown or rise of the lake level. This emphasizes the importance of the lake level fluctuations on the overall stability of the dam. The case studied here is a long-term existing landslide dam, hence it was expected to observe rather high values for the factor of safety.

5. References

[1] Costa, J.E. & Schuster, R. L., (1988). The formation and failure of natural dams. *Geol. Soc. America Bull*. 100(7), 1054-1068.

[2] Berilgen, M.M. (2007). Investigation of stability of slopes under drawdown conditions, *Computers and Geotechnics*, V. 34, pp. 81-91.

NUMERICAL SIMULATION OF SOIL LIQUEFACTION IN A CENTRIFUGE TEST CONSIDERING THE SOIL PREPARATION METHOD

C. Saade, Z. Li, S. Escoffier and L. Thorel
Laboratoire Centrifugeuses Géotechniques (CG), Département GERS, Université Gustave Eiffel
Allée des Ponts et Chaussées, CS 5004, 44344, Bouguenais, France

1. Introduction

Soil liquefaction, which is a major topic in geotechnical earthquake engineering, is regarded as both a complex and devastating phenomenon. The liquefaction-induced damage or failure of embankments has attracted the attention of researchers and engineers for decades. In recent decades, many laboratory tests were conducted to investigate the liquefaction behavior of soils. As it was reported, the soil preparation method affects significantly the liquefaction resistance [1, 2], which should be carefully considered. In this study, a dynamic centrifuge test of an embankment resting on liquefiable ground was simulated. The effect of wet tamping method that was used in the preparation of the centrifuge model was carefully considered in the numerical model.

2. Methodology

Different from the air pluviation method that is often adopted in the centrifuge model preparation, in this study, the liquefiable ground under the embankment (Hostun HN31 sand) was prepared using wet under-compaction method. As mentioned before, different preparation methods influence greatly the liquefaction behavior. Therefore, for the numerical modeling, the effect of the wet under-compaction on the cyclic resistance of the soil has to be carefully considered. In this study, the advanced constitutive model PM4Sand [3] was used in the modeling of soil liquefaction. In the PM4Sand model, the contraction rate parameter h_{po} plays an important role in the cyclic shear strength of soil, which can be well calibrated with $CRR - N$ curves from the simple shear tests. In order to be consistent with the model preparation method in the centrifuge test, h_{po} has to be calibrated against the $CRR - N$ curves which were obtained by the same wet under-compaction method. Therefore, the triaxial cyclic $CRR - N$ curves of Gobbi [4] were adopted, and the experimental data were converted to the simple shear form by the equation proposed by Idriss and Boulanger [5]. Then, the calibration of cyclic resistance of sand prepared with wet under-compaction method was performed. In order to highlight the difference between different preparation methods, the calibration was also carried out for the sand prepared with conventional air pluviation method and the experimental results of Kassas [6] were adopted.

Figure 1 shows the calibration results and the different $CRR - N$ curves from wet compaction and air pluviation methods. It is clear that the cyclic shear resistance of the sand prepared with wet under-compaction model is lower, which is in accordance with Benahmed [2]. These two calibrated $CRR - N$ curves were then applied in the simulation of a centrifuge test of an embankment resting on a soil ground.

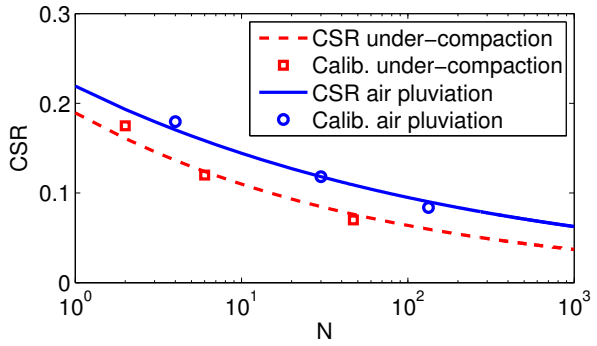

Figure 1. Calibration of the cyclic shear resistance considering different sand preparation methods

3. Results

The simulation results were compared with those of the centrifuge test, in which the soil was prepared with under-compaction. As shown in Figure 2 that the model with parameters calibrated with under-compaction method has a better performance in terms of acceleration response.

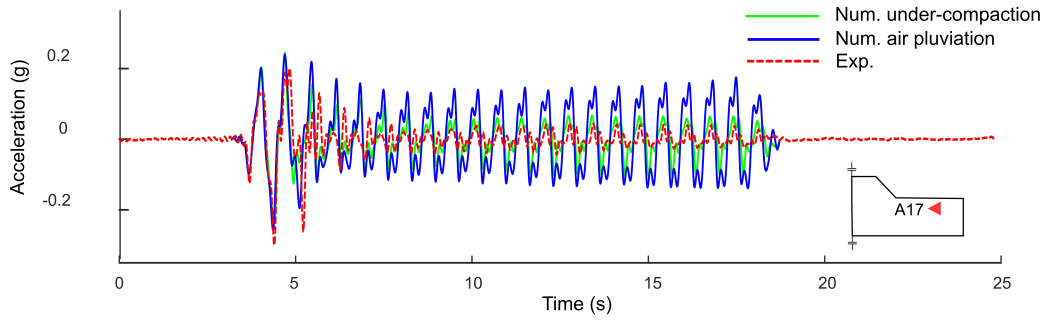

Figure 2. Numerical results vs. centrifuge test results

References

[1] Tatsuoka, F., Ochi, K., Fujii, S., and Okamoto, M. (1986). Cyclic undrained triaxial and torsional shear strength of sands for different sample preparation methods. *Soils and Foundations*, **26**, 23–41.

[2] Benahmed, N. (2001). *Comportement mécanique d'un sable sous cisaillement monotone et cyclique: Application aux phénomène de liquéfaction et de mobilité cyclique.*. Ph.D. thesis, Ecole National des Ponts et Chaussée.

[3] Boulanger, R. W. and Ziotopoulou, K. (2015). PM4Sand Version 3 : A sand plasticity model for earthquake engineering applications. *Centre for Geotechnical Modeling, University of California*.

[4] Gobbi, S. (2020). *Characterization of liquefaction parameters for saturated soil under dynamic loading using laboratory tests and calibration of constitutive laws by numerical modelling*. Ph.D. thesis, Université Paris Est.

[5] Idriss, I. and Boulanger, R. (2008). Soil liquefaction during earthquakes. *EERI Publication, Monograph MNO*, **12**.

[6] Kassas, K. (2021). *Structure-Soil-Structure Interaction (SSSI) of adjacent buildings founded on liquefiable soil*. Ph.D. thesis, ETH Zurich, Zurich.

NUMERICAL ANALYSIS OF LIQUEFACTION POTENTIAL OF A TAILINGS DAM

A. Geppetti[1] J. Facciorusso[1] G. Ciardi[2] L. F. Prada-Sarmiento[3] C. Madiai[1]
1 Department of Civil and Environmental Engineering, University of Florence, Firenze, Italy
2 Department of Civil and Environmental Engineering, University of Perugia, Perugia, Italy
3 Department of Civil and Architectural Engineering, Aarhus University, Denmark

1. Introduction

One of the most impactful aspects of mining activities is the need to store vast quantities of waste near the mine itself. This waste, commonly referred to as tailings, is characterized by a typical behaviour of non-cohesive contractive soils. These materials are often retained by earth dams constructed with the coarser fraction of the tailings. Several studies have shown that one of the most frequent causes of collapse of these structures is liquefaction triggered by earthquakes. In this study, the seismic liquefaction potential of a tailings dam located in southern Tuscany (Italy) was examined through numerical analyses conducted with the software OpenSees. The liquefaction potential was evaluated for both the material contained in the settling basin and that constituting the dam itself.

2. Tailings dam characterization

The analyzed tailings dam has a crest height of about 36.5 m above ground level and contains a volume of about 600.000 m^3 of slurry. The dam built with the upstream method has the configuration shown in Fig. 1, in which it is possible to identify three geotechnical units: settling tailings (U1), embankment material (U2) and clay foundation (U3).

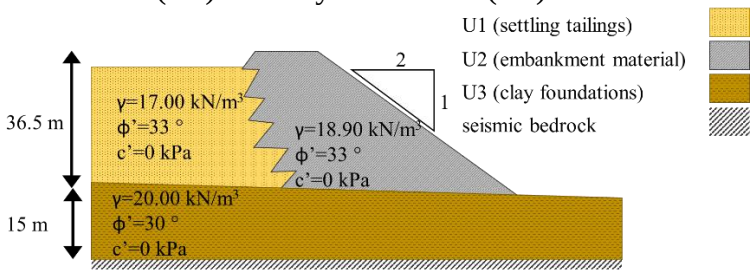

Figure 1. Tailings dam section.

3. Numerical model definition

A 2D finite element model of the structure was created with OpenSees software to examine its liquefaction potential under seismic conditions. The domain was discretized with a mesh incorporating 1147 quadrangular elements, each with the longest side of approximately 3 m. The dimensions of the elements were determined considering the shear wave velocity propagation in the material and the maximum frequency of the seismic signal. The water table was placed approximately at the level of the basin top to simulate fully saturated conditions. Different constitutive models were assigned to the three geotechnical units, to represent the diverse mechanical behavior of these materials. The SANISAND [1] constitutive model was assigned to the U1 geotechnical unit, while PM4Sand [2] was used for U2, and the Pressure Independent Multi Yield PIMY model [3] was given to U3. The calibrated parameters for the SANISAND model were validated through the comparison of undrained cyclic triaxial tests results with numerical simulations of the same test. It was not possible to apply the same procedure to the U2 material, as it contains a large coarse fraction which prevents laboratory tests from being carried out. Therefore, the parameters attributed to the PM4Sand constitutive model were estimated by field surveys (CPT, SPT). Finally, for the PIMY model the

parameters suggested by the authors in ref. [3] were used. The nodes at the base of the model were prevented from translating in the vertical direction and had the properties of a Lysmer-Kuhlemeyer (1969) dashpot. Elements close to the lateral boundaries of the domain were assigned a large thickness, to allow them to absorb the seismic waves and simulate free-field conditions. The seismic input obtained using SCALCONA 3.0 software, as suggested by the Tuscany Region guidelines for a 2475-year return period, was deconvoluted to bring the signal to the basis of the 2D model.

5. Results and conclusion

The performed analysis consisted of two steps. First, a gravitational load was applied to calculate the initial stress distribution. Later, a dynamic analysis was conducted in which the seismic load was applied to the nodes at the base of the model. The liquefaction potential was evaluated as [4]:

$$\zeta = -\frac{\sigma'_{ii}(t^{dyn}) - \sigma'_{ii}(t=0)}{\sigma'_{ii}(t=0)}$$

where $\sigma'_{ii}(t^{dyn})$ is the trace of the effective stress tensor at a precise moment of the earthquake and $\sigma'_{ii}(t=0)$ is the trace of the effective stress tensor before the earthquake. Liquefaction occurs if $\zeta = 1$. It is possible to observe (Fig. 2) that the maximum ζ, recorded at the end of the strong motion, reached is about 0.18 in some limited areas of the embankment.

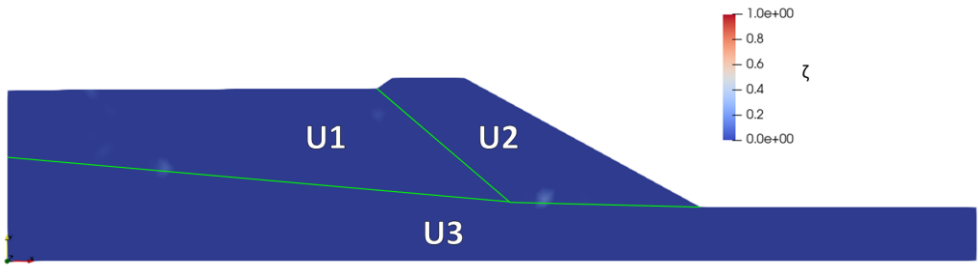

Figure 2. Liquefaction potential evaluation through effective stress ratio ζ.

From this preliminary analysis it emerged that the structure is not particularly prone to seismic liquefaction. However, further work in numerical modelling and materials characterization is needed to obtain more reliable results.

6. References

[1] Dafalias Y. F., Manzari M.T. (2004). Simple Plasticity Sand Model Accounting for Fabric Change Effects. *Journal of engineering mechanics, ASCE*, **130(6)**, 622-634.

[2] Boulanger R. W., Ziotopoulou K. (2017). PM4Sand (version 3.1): A sand plasticity model for earthquake engineering applications. Report No. UCD/CGM-17/01. *Center for Geotechnical Modeling, Department of Civil and Environmental Engineering, University of California, Davis, CA.*

[3] Yang Z., Elgamal A., Parra E. (2003). Computational Model for Cyclic Mobility and Associated Shear Deformation. *Journal of Geotechnical and Geoenvironmental Engineering, ASCE*, **129(12)**, 1119-1127.

[4] Machaček, J., Triantafyllidis, T., Staubach, P. (2018). Fully coupled simulation of an opencast mine subjected to earthquake loading. *Soil Dynamics and Earthquake Engineering*, **115**, 853-867.

USING VOLUME AVERAGING TECHNIQUE FOR MODELLING OF DEEP MIXING

A. Abed and M. Karstunen
Chalmers University of Technology, Gothenburg, Sweden

1. Introduction

The Volume Averaging Technique (VAT) is an attractive numerical tool to homogenize two independent constitutive models. In the current study, VAT is used for deriving the averaged material response of the column-improved ground to map this fully 3D problem into an equivalent 2D plane-strain counterpart. The method is validated in the field scale by replicating the measured performance of the trial embankments in Paimio in Finland, demonstrating very good accuracy.

2. Volume averaging technique and numerical implementation

VAT represents the behaviour of a composite material by an equivalent uniform material. Vogler [1], being inspired by the early work in refs. [2] and [3], adopted VAT to model the behaviour of the deep mixed columns and the surrounding untreated natural soil assuming an equivalent homogenised material. The method is based on the following fundamental averaging equation:

$$\boldsymbol{\sigma}^{\dot{e}q\prime} = \Omega_c \, \dot{\boldsymbol{\sigma}}^{c\prime} + \Omega_s \, \dot{\boldsymbol{\sigma}}^{s\prime} \tag{1}$$

where $\boldsymbol{\sigma}^{\dot{e}q\prime}$ is the 'averaged' effective stress rate in the equivalent homogenised material, $\dot{\boldsymbol{\sigma}}^{c\prime}$ and $\dot{\boldsymbol{\sigma}}^{s\prime}$ are the effective stress rates in the column and the soil, respectively. The symbols Ω_c and Ω_s denote the volume fraction of the column and the soil, respectively. Similar to Eq. (1), the equivalent strain rate $\boldsymbol{\varepsilon}^{\dot{e}q}$ reads:

$$\boldsymbol{\varepsilon}^{\dot{e}q} = \Omega_c \, \dot{\boldsymbol{\varepsilon}}^{c} + \Omega_s \, \dot{\boldsymbol{\varepsilon}}^{s} \tag{2}$$

where $\dot{\boldsymbol{\varepsilon}}^{c}$ and $\dot{\boldsymbol{\varepsilon}}^{s}$ are the strain rates in the column and the soil, respectively. To use the above-mentioned homogenisation equations, the following assumptions are employed for the case of vertically loaded embankments on improved soil:

Kinematic constraints

$$\dot{\varepsilon}_{yy}^{eq} = \dot{\varepsilon}_{yy}^{c} = \dot{\varepsilon}_{yy}^{s} \quad \text{and} \quad \dot{\gamma}_{xz}^{eq} = \dot{\gamma}_{xz}^{c} = \dot{\gamma}_{xz}^{s}$$

Local mechanical balance (3)

$$\dot{\sigma}_{xx}^{eq\prime} = \dot{\sigma}_{xx}^{c\prime} = \dot{\sigma}_{xx}^{s\prime} \; ; \; \dot{\sigma}_{zz}^{eq\prime} = \dot{\sigma}_{zz}^{c\prime} = \dot{\sigma}_{zz}^{s\prime}$$
$$\dot{\sigma}_{xy}^{eq} = \dot{\sigma}_{xy}^{c} = \dot{\sigma}_{xy}^{s} \; ; \; \dot{\sigma}_{zy}^{eq} = \dot{\sigma}_{zy}^{c} = \dot{\sigma}_{zy}^{s}$$

After some algebraic operations, the following analytical form for the equivalent material stiffness matrix $\mathbf{D}^{eq}$ can be derived [1]:

$$\mathbf{D}^{eq} = \Omega_c \mathbf{D}^{c} \mathbf{S}^{c} + \Omega_s \mathbf{D}^{s} \mathbf{S}^{s} \tag{4}$$

where $\mathbf{S}^{c}$ and $\mathbf{S}^{s}$ are the so-called strain distribution matrices, which depend on the constituent stiffness matrices (i.e., $\mathbf{D}^{c}$ and $\mathbf{D}^{s}$) and volume ratios (i.e., Ω_c and Ω_s).

The homogenisation procedure is implemented into the commercial finite element code Plaxis 2D (version 2021) as a User Defined Model based on [1]. The analysis starts by assuming elastic behaviour for columns and soil allowing to form the matrix $\mathbf{D}^{eq}$ analytically employing Eq. (4). Then, following the standard finite element procedure, the global stiffness matrix $\mathbf{K}$ is assembled and the equivalent displacement increment $\Delta\boldsymbol{u}_{eq}$ is calculated in response to the applied force increment $\Delta\mathbf{F}$. Consequently, the equivalent strain increment $\Delta\boldsymbol{\varepsilon}^{eq}$ is estimated at the stress integration points. At this point, the strain distribution matrices $\mathbf{S}^{c,s}$ are used to distribute the equivalent strain increment $\Delta\boldsymbol{\varepsilon}^{eq}$

into soil strain increment $\Delta\boldsymbol{\varepsilon}^s$ and column strain increment $\Delta\boldsymbol{\varepsilon}^c$ according to:

$$\Delta\boldsymbol{\varepsilon}^c = \mathbf{S}^c \ \Delta\boldsymbol{\varepsilon}^{eq} \ ; \ \Delta\boldsymbol{\varepsilon}^s = \mathbf{S}^s \ \Delta\boldsymbol{\varepsilon}^{eq} \tag{5}$$

Afterwards, any suitable stress-strain relationship can be used to calculate the corresponding increment of effective stresses in the soil $\Delta\boldsymbol{\sigma}^{c\prime}$ and the column $\Delta\boldsymbol{\sigma}^{s\prime}$ separately. In this study, the S-Clay1S model is used to model the natural clay behaviour, whereas the MNHard model [4] is employed to capture the behaviour of the mixed columns. Having estimated the effective stress increment in each component (i.e., soil and column), the corresponding final effective stresses (i.e., $\boldsymbol{\sigma}^{c\prime}$and $\boldsymbol{\sigma}^{s\prime}$) are subjected to a local balance check provided by Eq. (3). If the conditions are satisfied, the final effective stress in the equivalent material $\boldsymbol{\sigma}^{eq\prime}$ is estimated based on Eq. (1). Otherwise, a strain redistribution procedure is initiated, and iteratively repeated until the local balance is satisfied.

3. Validation against the measurements of the trial embankments in Paimio/Finland

2D calculations with VAT were carried out to simulate the behaviour of trial embankments in Paimio for three different cases of column spacings (i.e., case c/c = 1.0m, c/c=1.2m and c/c = 1.4m). The vertical settlements as predicted by VAT technique is compared to the measured. As an example, Figure 1 depicts the results for the case c/c = 1.0m. The results of the embankment on greenfield were also plotted as a reference to highlight the efficiency of the soil improvement.

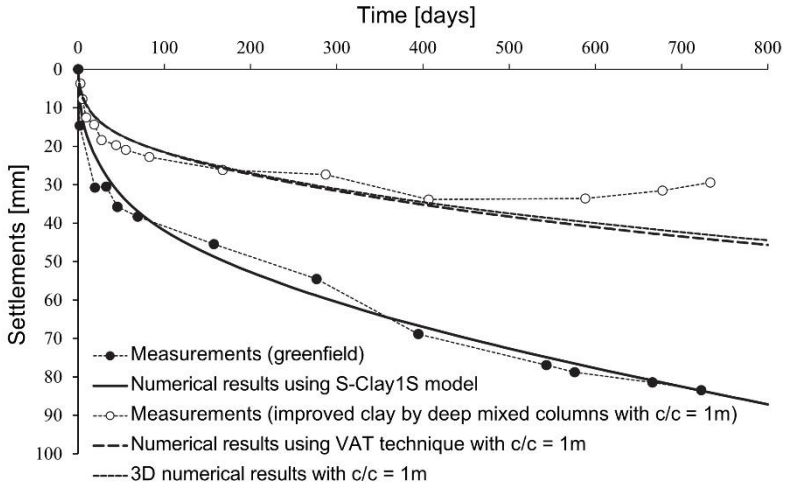

Figure 1. Calculated versus measured vertical displacement for Paimio test embankments.

4. Conclusion and main results

As can be seen in Figure 1, the developed volume averaging technique is validated by being able to replicate the measured settlement with a very good accuracy. The mapping of the actual 3D problem to an equivalent 2D problem reduces tremendously the required modelling and calculation time, allowing for more time to be spent on investigating the alternatives during the design phase.

5. References

[1] Vogler, U. (2009). *Numerical modelling of deep mixing with volume averaging technique*. PhD thesis, University of Strathclyde.

[2] Lee, J.S. & Pande, G.N. (1998). Analysis of stone-column reinforced foundations. *Int. J. Numer. Anal. Methods Geomech.* **22**, 1001–1020

[3] Schweiger, H.F. & Pande, G.N. (1989). Modelling Stone Column Reinforced Soil-A Modified Voigt Approach. *Numerical Models In Geomechanics*. Publ. Elsevier Appl. Sci. Publ. Ltd.

[4] Benz, T. (2007). *Small-strain stiffness of soils and its numerical consequences*. PhD thesis, Stuttgart University.

MODELING PILES/BARRETTES USING BEAM ELEMENTS AND NONLOCAL KINEMATIC CONSTRAINTS

A. Truty
Cracow University of Technology, Cracow, Poland

1. Introduction

A simplified treatment of piles/barrettes (called here as rigid inclusions (RI)) and their shaft/tip contact interfaces seems to be the only rational approach in the course of designing complex foundation systems, using FE geotechnical software. The main goal of the approach is to discretize RI members independently on the 3D background mesh but being able to represent strong displacement discontinuity between subsoil and the RI. Such a method is known as an embedded beam formulation [1]. Several initial approaches [2–5], that can be classified as local ones, exhibit pathological mesh dependency unless certain rules concerning the size of the background 3D continuum mesh are satisfied. In case of complex FE models controlling the element size may not be an easy task hence further improvements were proposed by including a certain form of nonlocality by means of so called virtual surface defined by the pile perimeter [6–8]. A more comprehensive analysis of different approaches concerning the embedded beam concept is given in paper [9]. In this approach a nonlocal concept of embedding beam elements within the 3D continuum is proposed by introducing the virtual surface, along the real RI perimeter, and the virtual volume coinciding with the real RI volume. The relative motion of beam element nodes with respect to the background 3D continuum mesh is computed using nonlocal form of kinematical constraints [9]. This method, contrary to all former approaches, exhibits a monotonic h-convergence property and ensures objective results when modeling structural beam-slab connections. In the current implementation circular and quadrilateral RI cross sections are considered.

2. General concept

The general idea is explained in Fig.1. Beam element nodes are donoted here by A_k while reference nodes, nonlocally connected to the background 3D mesh, are denoted by R_k. Pairs of nodes $A_k - R_k$ form a frictional node-to-node shaft interface while pair of nodes $A_3 - T_3$ a node-to-node tip interface. At each beam node a cross section is generated. This cross section is further split into $n \times m$ cells with centroids represented by black dots. In local approaches, the motion of a reference node R_k is based on the motion of continuum element nodes in which the R_k node is embedded. Hence the resulting stiffness matrix and internal force vector are dispatched on a very limited set of nodes of background mesh. In the current approach the motion of a reference point R_k depends on the motion of each cell centroid, therefore, beam nodal stiffness matrix and internal force vector are dispatched on a much larger set of nodes in the background mesh. Displacement vector of a given reference point (node) can be expressed by the following linear combination ($\sum w_k = 1$) of nodal displacement vectors which belong to the current set $\mathcal{S}$

$$\mathbf{u}_R = \sum_{i=1}^{\text{size}(\mathcal{S})} w_i^{\text{glo}} \mathbf{u}_i^{\mathcal{S}} \tag{1}$$

A detailed procedure to set up the set of nodes $\mathcal{S}$ and nodal weights w_i^{glo} is given in the author's paper [9]. A similar approach is used to connect beam (pile/column) node with the slab (shell) in a nonlocal form. Additional control points are put along the RI perimeter to trace contact stresses in the shaft interface.

h!

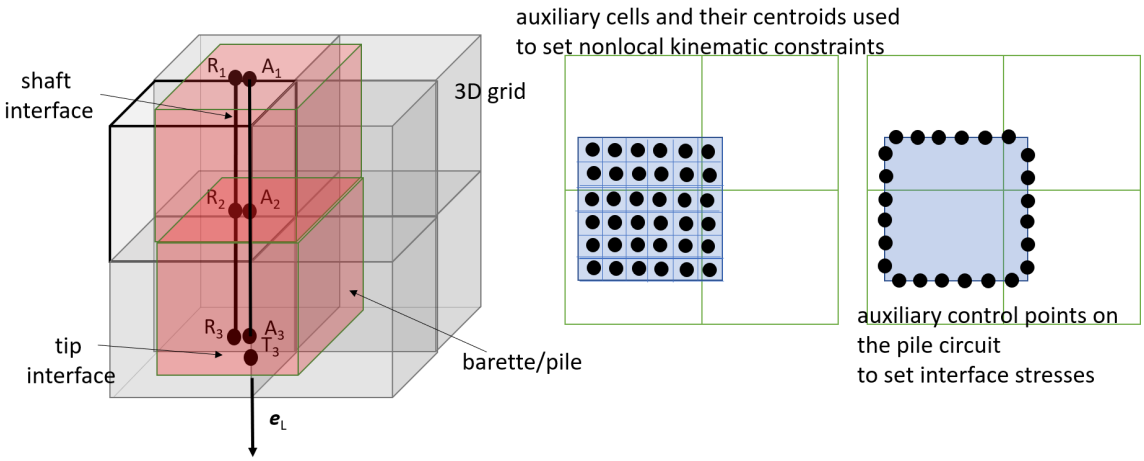

Figure 1. Beam elements with virtual volume and surface embedded in 3D continuum FE mesh

3. Results and conclusions

The proposed approach enables embedding RI as beam elements within the 3D FE mesh in an arbitrary manner and to connect RI heads with rafts/slabs also at an an arbitrary point. It exhibits a monotonic $h-$ convergence property and yields mesh independent cross sectional forces in piles at the pile-slab connection points.

References

[1] Sadek, M. and Shahrour, I. (2004). A three dimensional embedded beam element for reinforced geomaterials. *International Journal for Numerical and Analytical Methods in Geomechanics*, **28**, 931–946.

[2] Engin, H. K., Septanika, E. G., and Brinkgreve, R. B. J. (2007). Improved embedded beam elements for the modelling of piles. *Proceedings Numerical models in geomechanics (NUMOG X) (eds. Pande & Pietruszczak)*, Rhodos, Greece, p. 475–480, Taylor & Francis.

[3] Septanika, E., Bonnier, P. G., and Brinkgreve, R. B. J. (2007). An efficient 3d modeling of (multi) pile-soil interaction. *Proceedings International Geomechanics Conference, Nessebar, Bulgaria*, Sofia: University of mining and geology "St. Ivan Rilski", pp. 67–76.

[4] Tschuchnigg, F. (2012). *3D Finite Element Modelling of Deep Foundations Employing an Embedded Pile Formulation*. Ph.D. thesis, Graz University.

[5] Truty, A. (2009). Fem models of large piled rafts (in polish). *"Zeszyty Naukowe Politechniki Krakowskiej. Seria Inżynieria Środowiska. Zeszyt 14"*, **4-Ś**, 137–150.

[6] Turello, D. F., Pinto, F., and Sanchez, P. J. (2016). Embedded beam element with interaction surface for lateral loading of piles. *International Journal for Numerical and Analytical Methods in Geomechanics*, **40**, 568–582.

[7] Turello, D. F., Pinto, F., and Sanchez, P. J. (2016). Three dimensional elasto-plastic interface for embedded beam elements with interaction surface for the analysis of lateral loading of piles. *International Journal for Numerical and Analytical Methods in Geomechanics*, **41**, 859–879.

[8] Smulders, C., Hosseini, S., and Brinkgreve, R. B. J. (2019). Improved embedded beam with interaction surface. *Proceedings of the XVII European Conference on Soil Mechanics and Geotechnical Engineering*, Reykjavik, Iceland.

[9] Truty, A. (2023). Nonlocal fem modeling of piles as beam elements embedded within 3d continuum. *Engineering Structures*, **277**.

NUMERICAL STUDY OF THE THERMAL PERFORMANCE OF AN ENERGY MICROPILE

G. Ciardi and C. Tamagnini
University of Perugia, Perugia, Italy

1. Introduction

Energy geostructures are being developed throughout the world to reduce the energy consumption of buildings using a free, *unlimited*, green source of energy – geothermal energy at shallow depths – for heating and cooling of living spaces. The working principle of energy geostructures is to exchange heat with the soil, which acts as a heat source/sink: the heat is extracted from the soil in cold seasons, while it is stored in it in hot seasons [1]. This process is usually possible due to the presence of a heat–carrier fluid flowing through plastic/aluminum pipes embedded in the energy geostructure. Deep foundations, such as piles, can satisfactorily be designed to combine structural and thermal performance.

Previous research showed that also micropiles, a kind of cast–in–place deep foundation structure usually used for the retrofitting of existing buildings, can be used as energy geostructures. In previous studies, however, the heat transfer process occurring in energy micropiles has been studied by incorporating several simplifying assumptions. Among these, the most recurrent ones involve neglecting the real size of the fluid–circulating pipes and neglecting the possible interaction of the energy micropile with the surrounding structures, including other energy micropiles incorporated in the same foundation.

In this study, the heat transfer process occurring in a single energy micropile, part of a wide pile group with hexagonal disposition in plan, is analyzed by means of a three–dimensional numerical FE model. The FE simulations aim at investigating the role played by the thermal conductivity of the mortar constituting the pile on the thermal performance of the energy geostructure.

2. Problem statement and methodology

A pure heat transfer analysis was carried out on a single energy micropile embedded in a saturated clay layer, 15 m thick, assuming that i) the heat conduction dominates at the micropile/soil interface, in the soil, and in the materials constituting the pile, and that ii) the heat transfer occurs by forced convection and conduction in the heat–exchanger pipes.

A series of three–dimensional, time–dependent, parametric heat transfer simulations were performed on a single energy micropile with varying thermal conductivity values of the mortar used for the micropile construction. The FE platform Abaqus Standard was used in all simulations. The micropile has diameter d = 0.2 m and length L = 12 m, while the tubular steel reinforcement has external diameter d_{st} = 0.127 m and thickness of 10 mm. The mortar fills the annulus between the steel reinforcement and the soil, and it is also placed inside the tubular reinforcement, outside of the plastic pipes. The micropile is assumed equipped with a single U–shape HDPE tube for heat–carrier fluid flow, with internal diameter d_p = 0.02 m and thickness of 3 mm. The micropile was considered to be a part of an energy micropiles group arranged in a hexagonal pattern. The finite element model considers a single hexagonal periodic unit, with piles placed at a distance $D = 10d$. To further simplify the numerical model, the hexagonal cell has been replaced by a cylindrical domain with a single energy pile on its axis and a radial adiabatic boundary placed at distance $R = 5d$ from the pile axis, *i.e.*, midway between two adjacent piles. The bottom boundary of the domain is placed at a

distance z_b = 15 m from the ground surface. Due to the symmetry with respect to the vertical plane containing the HDPE tube, only half of the domain was modeled.

As the initial condition, a prescribed temperature T_0 = 15 °C was assigned to the whole model. For the boundary conditions, zero heat flux was prescribed at the lateral cylindrical boundary and on the symmetry plane. A prescribed temperature, T_i, was assigned on the convective surface at the inlet of the heat–exchanger pipe. The temperature T_i was assumed to be cyclically time–dependent over a period t_s = 1 year, starting from $T_i = T_0$ and varying in the range $T_i = \pm 0.8T_0$. The temperature increase/decrease ramps lasted for 12 hours. A prescribed mass flow rate of 0.05 kg/s was assigned to the fluid (water) circulating into the pipe. A fixed temperature, equal to T_0, was assigned at depth $z = z_b$ and kept constant throughout the simulation time. Similarly, a constant temperature equal to T_0, was assigned on the ground surface excluding the micropile surface.

The spatial discretization adopted consisted of 498705 linear tetrahedral and hexahedral elements for heat transfer. In order to use a single hexahedral element to model the fluid, the (circular) pipe section was schematized as an area–equivalent squared section. Different values of mortar thermal conductivity k (namely 1.17, 1.28 and 1.44 W/m/°C) were used in the simulations. These values, as well as the material density and specific heat, have been obtained in a parallel experimental investigation [2]. The soil thermal conductivity was assumed equal to 1.5 W/m/°C.

3. Results

The results of the analysis are discussed in terms of the heat flux transferred by the circulating fluid, Q_f, that can be used as a significant indicator of the system efficiency. Figure 1 shows the Q_f (left axis) and T_i (right axis) against time, t. The Q_f significantly varies over time, with maximum/minimum values (absolute and relative) associated with significant T_i rates. When T_i is constant, Q_f increases/decreases with time. The increase/decrease rate depends on how fast the system strives to reach thermal equilibrium which, in turn, depends on the thermal properties of the materials. It is worth observing that the Q_f peaks are associated with the maximum k value used (1.44 W/m/°C). However, the overall Q_f increase obtained with increasing k values was relatively limited.

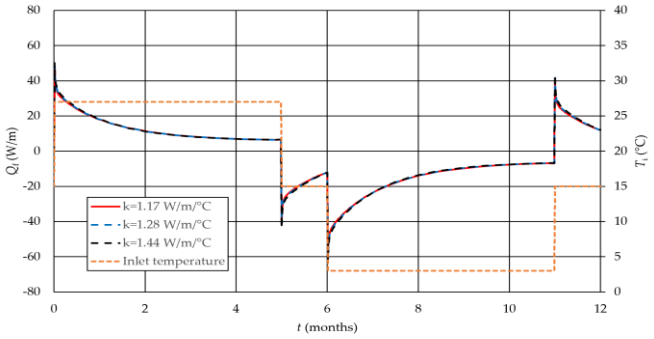

Figure 1. Heat flux transferred by the fluid (left axis) and inlet temperature (right axis) versus time.

5. References

[1] Brandl, H. (2006). Energy foundations and other thermo-active ground structures. *Géotechnique*, **56**, 81–122.

[2] Ciardi, G., Madiai, C. & Tamagnini, C. Experimental study on the thermal properties of cement–based grouts for energy micro-piles. *Submitted to Geomechanics for Energy and the Environment.*

SOIL INERTIA IN THE MACRO-RESPONSE OF GEOTECHNICAL SYSTEMS: A THERMODYNAMIC PERSPECTIVE

D. N. Gorini
Sapienza University of Rome, Rome, Italy

1. Motivation

Recent studies pointed out the significance of the soil mass participation in the seismic response of several foundation typologies. This can cause prominent inertial effects associated with the vibration modes of the soil-foundation system, that impact the displacement and ductility demand of critical components of the superstructure [1-4].

2. Analysis approach and inertial effects

In this work, the above effects are handled through a computationally efficient macroelement approach [5,6]. In the method, Thermodynamic Inertial Macroelements (TIMs) simulate the multiaxial response of geotechnical systems in the assessment of structures, according to the analysis procedure depicted in Figure 1. The foundation motion, computed by means of a free-field site response analysis, represents the seismic input for the TIMs, which are included in the global structural model to carry out low demanding nonlinear dynamic analyses. A TIM relates the rates of the generalised forces, dQ_i, exchanged between the geotechnical system and the superstructure to the corresponding rates of displacements and rotations, dq_j, through a second-order tangent stiffness matrix H_{ij}. TIMs are multi-surface plasticity laws with kinematic hardening derived within a thermodynamic approach, using hyperplasticity [7], and simulate salient features of the dynamic response of geotechnical systems at the scale of the whole structural model, such as frequency and amplitude dependence. The TIM's formulation is implemented in OpenSees [8] and can be assigned to a novel finite element (elements H_{ij} in Fig. 1) defining a coupled translational-rotational relationship between two overlapped nodes [5].

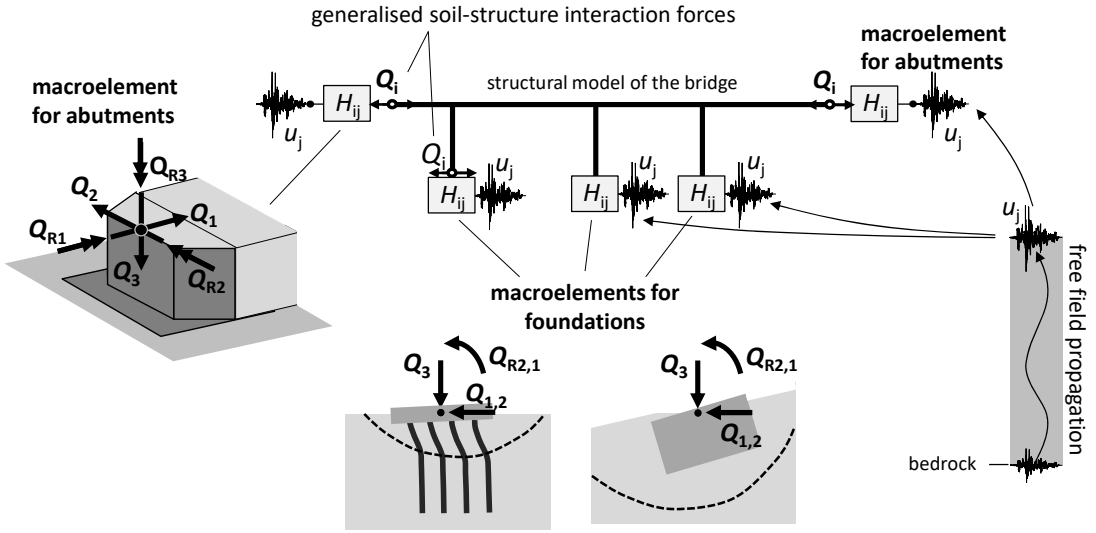

Figure 1. Application of TIMs in the seismic analysis of structures.

In the TIM approach, the following strategies are employed to account for the inertial effects developing in the soil-foundation system. The effects of the soil inertia can be directly incorporated in the hyperplastic formulation (*analytical solution* [9]) or can be reproduced by assigning the

modal masses of the geotechnical system to the soil-structure contact node of the element enclosing the TIM response in the global structural model (*numerical solution*). The former strategy leads to a more proper consideration of the mass participation variability beyond the reversible regime; the easily implemented *analytical solution* can approximate the frequency response of geotechnical systems for small- to medium-strain levels. The small-strain soil mass participation can be straightforwardly identified through analytical solutions or simplified numerical procedures [4-6,9], whilst preliminary indications on the increase of the mass participation with the level of mobilised strength are obtained through coupled soil-structure numerical analyses. A typical frequency-dependent cyclic response using the *analytical solution* is shown in Figure 2. The results were obtained by imposing a horizontal displacement time history varying in time with a sinusoidal law to the TIM for piled foundations, considering different normalised periods $T^{(ext)}/T^{(1)}$ ($T^{(ext)}$ being the period of the perturbation and $T^{(1)}$ the fundamental vibration period of the TIM).

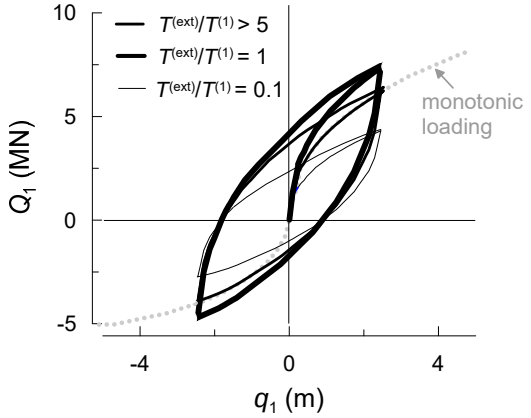

Figure 2. Response of the TIM for piled foundations to a horizontal sinusoidal motion.

3. References

[1] Elgamal, A., Yan, L., Yang, Z. & Conte, J.P. (2008): Three-Dimensional Seismic Response of Humboldt Bay Bridge-Foundation-Ground System, *Journal of Structural Engineering*, 134(7), 1165-1176 (2008).

[2] Stefanidou, S.P., Sextos, A.G., Kotsoglou, A.N., Lesgidis, N., & Kappos, A.J. (2017): Soil-structure interaction effects in analysis of seismic fragility of bridges using an intensity-based ground motion selection procedure, *Engineering Structures*, 151, 366-380.

[3] Gorini, D.N. & Callisto, L. (2020): A coupled study of soil-abutment-superstructure interaction, in: *Geotechnical research for land protection and development - proceedings of CNRIG 2019* (eds F. Calvetti, F. Cotecchia, A. Galli and C. Jommi), pp. 565-574. Cham, Switzerland: Springer.

[4] Gorini D.N., Callisto L. & Whittle A.J. (2022): An inertial macroelement for bridge abutments, *Géotechnique*, Vol. 72(3), pp. 247-259.

[5] Gorini, D.N. & Callisto, L. (2023): A multiaxial inertial macroelement for deep foundations, *Computers and Geotechnics*, Vol. 155, https://doi.org/10.1016/j.compgeo.2022.105222.

[6] Gorini, D.N., Callisto, L., Whittle, A.J. & Sessa, S. (2023): A multiaxial inertial macroelement for bridge abutments, *International Journal for Numerical and Analytical Methods in Geomechanics*, doi: 10.1002/nag.3493.

[7] Houlsby, G. T., and Puzrin, A. M. (2006): *Principles of hyperplasticity*, Springer, Berlin.

[8] McKenna, F., Fenves, G.L., Scott, M.H. & Jeremic, B. (2000): *Open system for earthquake engineering simulation*, http://opensees.berkeley.edu.

[9] Gorini, D.N. (2019): Soil-structure interaction for bridge abutments: two complementary macro-elements, *PhD thesis*, Sapienza University of Rome, Italy, https://iris.uniroma1.it/handle/11573/1260972.

NUMERICAL ANALYSIS OF ENERGY PILES SUBJECTED TO CYCLIC LOADS

C. Iodice[1], R. Di Laora[1], C. Tamagnini[2], G.M.B. Viggiani[3] and A. Mandolini[1]
[1] *Università della Campania 'Luigi Vanvitelli', Aversa, Italy*
[2] *University of Perugia, Perugia, Italy*
[3] *University of Cambridge, Cambridge, UK*

1. Introduction

Energy piles represent an environmentally friendly source for heating and cooling of buildings. Unlike traditional piles, they are equipped with closed-loop pipes allowing the circulation of a fluid to exchange heat with the ground. Due to the thermal interaction with the surrounding soil, energy piles are subjected to cyclic thermally induced axial forces (which add to the mechanical load transferred by the structure), as well as to additional permanent displacements caused by thermal cyclic loading. In addition to this, while heavily overconsolidated (OC) clays dilate with increasing temperature, soft normally consolidated (NC) or slightly OC clays experience volumetric contraction when heated in drained conditions. A small-scale experimental investigation on model piles showed that, while at the element scale the thermal collapse stabilizes within few cycles, the settlements accumulation of the energy pile continues cycle after cycle with no stabilization [1] and possible adverse effects on the serviceability of the supported structure. The main phenomena controlling the cyclic response of energy piles installed in soft clays can be studied by means of numerical analyses employing advanced constitutive models capable of capturing the main aspects of the soil behaviour under mechanical and cyclic thermal loadings. In the following, a selection of the results obtained from Finite Element analyses on a single ideal energy pile installed in a NC clay layer is presented.

2. Details of the FE model

A single energy pile 25 m long with a diameter of 0.5 m, embedded in NC clay is analysed via axisymmetric, non-linear, fully coupled thermo-hydro-mechanical simulations carried out by the FE code ABAQUS [2]. The soil is described using a hypoplastic model enhanced with the intergranular strain concept to reproduce the cyclic behaviour of clay (Hypo) [3]. To improve the description of thermo-mechanical coupling effects and allow the accumulation of irreversible contractive volumetric strains in NC conditions, an additional enhanced version of the model, implemented by the authors, is also employed (Hypo-T) [4]. The problem considered in the numerical simulations is analysed through the following steps: first, a mechanical loading stage is simulated at constant temperature in which the pile is subjected to two different values of the axial load, Q, namely $0.3R_t$ and $0.6R_t$, R_t being the bearing capacity of the pile evaluated using the β method; after that, 5 thermal cycles are applied. Each cycle consists of a 6-month phase in which the pile temperature is rapidly increased and then maintained constant for 5 months, followed by a thermal rest period of 1 month in which only the temperature at the pile head is rapidly reduced back to the ambient temperature and then kept constant. During the subsequent 6-month phase the cycle is simply reversed. The details of the numerical model as well as the constitutive parameters employed are reported in Iodice et al. [5].

3. Main results

Figure 1 depicts some relevant results. From the plots 1a and b it is evident that, while in isothermal conditions the response of the pile predicted by the two models is the same, during the cyclic thermal loading stage, the downward displacements predicted by the Hypo-T model are larger than those predicted by the Hypo model. This is a consequence of the permanent positive

volumetric deformations (thermal collapse) accumulated in the NC clay which do not show any significant reduction in the rate. It is worth mentioning that at the very beginning of the thermal loading phase the response predicted with the two models is almost identical. To understand this result, it is useful to clarify some aspects of the behaviour of a saturated soil subjected to a temperature increase under undrained conditions, which is the case of the performed analyses. In absence of volumetric collapse, the soil expands and, since the thermal expansion coefficient of the water is larger than that of the solid grains, the water would expand more than the voids volume for the same increase in temperature. Therefore, when the soil hydraulic conductivity is such that undrained conditions prevail, the pore water experiences an increase in pressure to guarantee the volumetric deformation compatibility between the two phases. In presence of thermally-induced volumetric collapse, a further excess pore pressure is generated due to the tendency of the soil skeleton to contract. This is evident in Figure 1c and d where the excess pore pressure, reported at different locations along pile-soil interface for the case $Q = 0.3R_t$, is larger for the Hypo-T model.

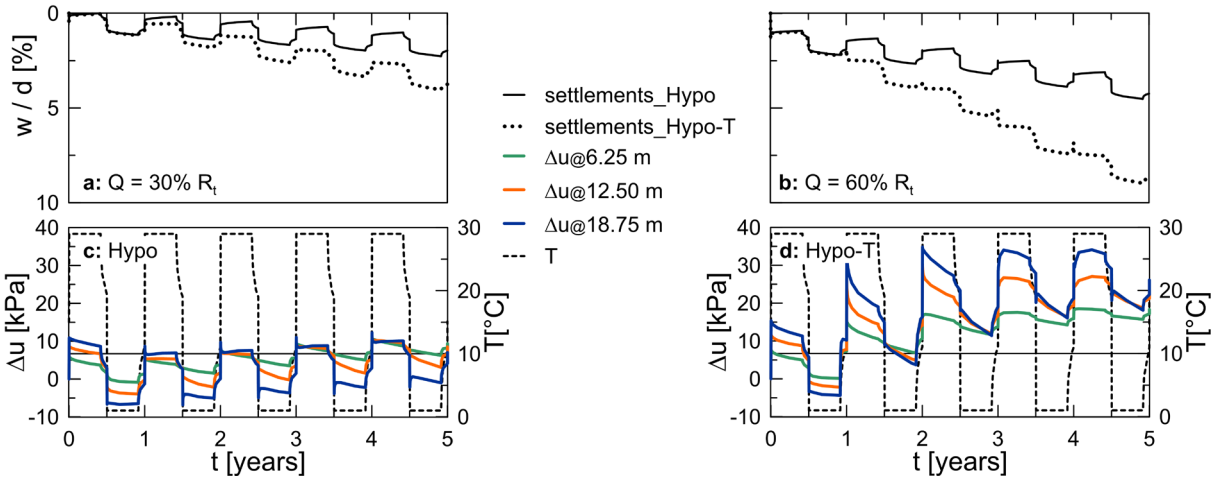

Figure 1. Settlements (a and b) and excess pore pressure (c and d).

Although the numerical simulations refer to a single free-head energy pile, they can be considered relevant for the behaviour of a pile group in which all the piles are thermally activated and sufficiently spaced to avoid thermal interference. The presence of inactive piles connected to the same cap may significantly reduce the magnitude of the irreversible pile head displacements. As a consequence of the above findings and previous literature studies, the latter configuration is the only design option when the settlements due to the cyclic temperature variations threaten the serviceability of the supported structure. In this case, a careful design of the foundation is necessary to satisfy both Ultimate Limit State and Serviceability Limit State requirements.

5. References

[1] Wu, D., Liu, H.L., Kong, G.Q., Ng, C.W.W., & Cheng, X.H. (2018). Displacement response of an energy pile in saturated clay. *Proc. Inst. Civ. Eng. Geotech*, **171**, No 4, 285-294.Dassault

[2] Systemes (2014). Abaqus Analysis User Guide v6.14. *Dassault Systèmes Simulia Corp.*, Providence, RI, USA.

[3] Mašín, D. (2019). *Modelling of Soil Behaviour with Hypoplasticity: Another Approach to Soil Constitutive Modelling*. Springer.

[4] Ma, Q.J., Ng, C.W.W., Mašín, D. & Zhou, C. (2017). An approach for modelling volume change of fine-grained soil subjected to thermal cycles. *Can. Geotech. J.*, **54**, No 6, 896–901.

[5] Iodice, C., Di Laora, R. & Mandolini A. (2023). A practical method to design thermally stressed piles. *Géotechnique*, **73**, No. 1, 30-43.

AN ELASTO-PLASTIC MACRO-ELEMENT FOR PILE GROUPS UNDER INCLINED AND ECCENTRIC LOADS

C. Iodice[1], M. Iovino[2], R. Di Laora[1], L. de Sanctis[2] and A. Mandolini[1]
[1]University of Campania 'Luigi Vanvitelli', Aversa (Caserta), Italy
[2]University of Napoli 'Parthenope', Napoli, Italy

1. Introduction

A new macro-element for pile groups under monotonic loading is presented herein, built on the classical theory of isotropic strain-hardening plasticity. The main assumption is that the yield surface in the generalized force space has a fixed shape and expands homothetically with respect to the axes origin util reaching the failure locus. Plastic displacements are developed according to a non-associated flow rule along with a hardening law derived by reproducing the behaviour of pile groups under monotonic loading observed in field tests. A few parameters are needed to calibrate the model, most of which are required in routine design. The performance of the macro-element is validated against data from centrifuge tests.

2. Mathematical model

The isotropic-hardening elastoplastic relationship between the generalized force, $d\boldsymbol{V}$, and the corresponding displacement, $d\boldsymbol{v}$, vectors, is formulated in rate-form as $d\boldsymbol{v} = \boldsymbol{K}^{-1}d\boldsymbol{V}$, where $\boldsymbol{V}^T = \{Q, H, M/R\}$, $\boldsymbol{v}^T = \{w, u, \theta \cdot R\}$, ($Q$, H, M) are the resultant forces (vertical, horizontal, moment) acting on the top of the rigid raft connecting the piles, (w, u, θ) are the work-conjugated displacements (horizontal, vertical, and rotation), R is a characteristic length of the foundation and $\boldsymbol{K}$ is the tangent stiffness matrix of the pile group. The total incremental displacement of the foundation can be decomposed into its elastic and plastic counterparts. In the model there is always a finite region in the force space which can be reached without incurring irreversible displacements. The boundary of the elastic region (yield surface, f) has the same shape as the failure locus but its size may vary according to an internal variable, ρ_c, accounting for the past load history of the foundation. While the elastic displacement increment occurs whenever there is a change in load ($d\boldsymbol{v}^e = \boldsymbol{K}_e^{-1}d\boldsymbol{V}$ where $\boldsymbol{K}_e$ is the elastic stiffness matrix), the plastic deformation increment occurs only when the actual load state, $\boldsymbol{V}$, lies on the yield surface and $d\boldsymbol{V}$ is directed outwards. Assuming a non-associated flow rule, it follows that $d\boldsymbol{v}^p = \Lambda \cdot \partial g / \partial \boldsymbol{V}$, where Λ is the plastic multiplier and g is the plastic potential. The equation of the failure locus is derived by combining a parabola approximating the exact solution in the (Q, M) plane based on theorems of limit analysis [1] and the Granville egg approximating the lower bound solution for failure loci in planes parallel to (Q, H) [2][3]. The yield function is scaled homothetically with reference to the axes origin through ρ_c:

$$f(\boldsymbol{V},\ \rho_c) = \frac{H^2}{\rho_c^2}\left[\sqrt{1-\frac{M}{\rho_c M_{\max}}} - (2\beta-1)\left(\frac{Q-\rho_c b}{\rho_c R}\right)\right]^2 + 4\beta(\beta-1)\left[\left(1-\frac{M}{\rho_c M_{\max}}\right) - \left(\frac{Q-\rho_c b}{\rho_c R}\right)^2\right]\left[H_{\max} + iR\left(1-\sqrt{1-\frac{M}{\rho_c M_{\max}}}\right)\right]^2 \quad (1)$$

where $b = 0.5\cdot(Q_c + Q_t)$, $H_{\max} = H_t + \beta\cdot(H_c - H_t)$, $i = (H_c - H_t)/(Q_c - Q_t)$, $R = 0.5\cdot(Q_c - Q_t)$, $\beta = [3 - 2\cdot(H_t / H_c)]/[4 - 2\cdot(H_t/H_c)]$, ($Q_c$, Q_t) are the axial capacities of the pile group in compression and in tension, (H_c, H_t) are the correspondent minimum and maximum lateral capacities, and $M_{\max}$ is the maximum value of the moment capacity. For $\rho_c = 1$, Eq. (1) returns the failure locus.

The equation of the plastic potential is:

$$g(\boldsymbol{V}) = \left[4\frac{\left(Q-\rho_g Q_c\right)\left(Q-\rho_g Q_t\right)}{\rho_g^2\left(Q_c-Q_t\right)^2}\right]^2 - \left(\frac{H}{\rho_g H_{\max}}\right)^2 - \left(\frac{M}{\rho_g M_{\max}}\right)^2 \quad (2)$$

where ρ_g is a scalar parameter allowing the surface $g = 0$ to pass through the current load state.

The evolution of ρ_c is governed by the following hardening law:

$$\frac{\partial \rho_c}{\partial w_p} = -\frac{1-\rho_c}{\rho_c\left[\ln(1-\rho_c)+\rho_c\right]}\cdot\left(\frac{\alpha_Q K_v}{Qc}\right)^2 \left|w^p\right|$$

$$\frac{\partial \rho_c}{\partial u_p} = -\frac{1-\rho_c}{\rho_c\left[\ln(1-\rho_c)+\rho_c\right]}\cdot\left(\frac{\alpha_H K_{hh}}{H_{\max}}\right)^2 \left|u^p\right| \qquad (3)$$

$$\frac{\partial \rho_c}{\partial \theta_p} = -\frac{1-\rho_c}{\rho_c\left[\ln(1-\rho_c)+\rho_c\right]}\cdot\left(\frac{\alpha_M K_{mm}}{M_{\max} R}\right)^2 \left|\theta^p R\right|$$

where α_Q, α_H and α_M are hardening parameters.

2. Validation against experimental benchmarks

The macro-element is validated using data from centrifuge tests on pile groups under centered (A1) and eccentric (A2) loads [4]. The failure locus of the model foundations is plotted in Figure 1a along with the load paths A1 and A2. The parameters in Table 1 adopted for the simulations are taken from [4]. Note that the maximum moment M_{max} has been evaluated as the vertex of the parabola passing through the points (Q_c, 0), (Q_t, 0), (Q_{A2}, M_{A2}), where Q_{A2} and M_{A2} are the axial load and moment capacities derived from test A2.

Table 1. Constitutive parameters of the elasto-plastic macro-element.

Centrifuge test	W_{piles} [kN]	W_{cap} [kN]	M_0 [kNm]	$Q_c + W_{piles}$ [kN]	$Q_t + W_{piles}$ [kN]	M_{max} [kNm]	K_v [MN/m]	K_θ [MNm]
A1 (A2)	834 (815)	379 (481)	0 (440)	3264	-2023	5648	129	1668

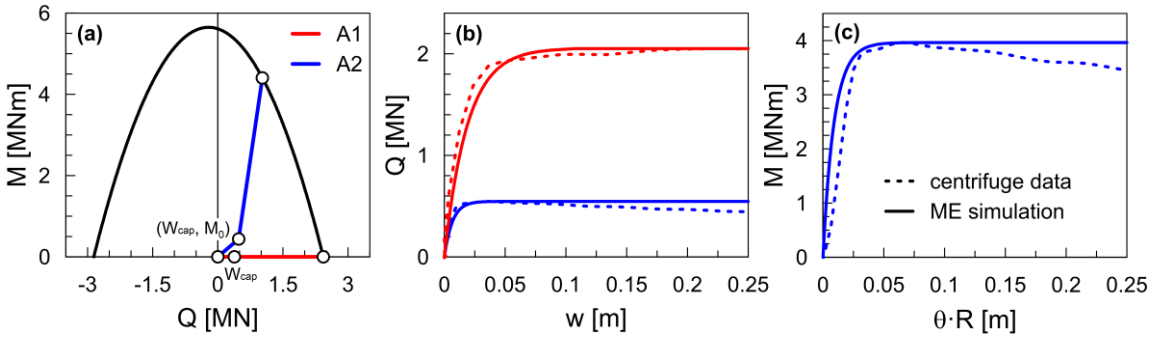

Figure 1. Comparison between ME and centrifuge data.

The response determined experimentally from test on pile groups A1 and A2 is compared to that evaluated through the macro-element in Figures 1b,c, respectively, under the assumption (α_Q, α_M) = (1, 1). The macro-element simulations match in a satisfactory way the experimental $Q - w$ and $M - \theta \cdot R$ curves, in which R is the radius of a circle passing through the piles.

3. References

[1] Di Laora, R., de Sanctis, L., & Aversa, S. (2019). Bearing capacity of pile groups under vertical eccentric load. *Acta Geotech.*, **14**, 193-205.

[2] Iovino, M., Maiorano, R.M.S., de Sanctis, L., & Aversa, S. (2021). Failure envelopes of pile groups under inclined and eccentric load. *Géotech. Lett*. **11(4)**, 247-253.

[3] Di Laora, R., Iodice, C., & Mandolini, A. (2022). A closed-form solution for the failure interaction diagrams of pile groups subjected to inclined eccentric load. *Acta Geotech.*, **17(8)**, 3633-3646.

[4] de Sanctis, L., Iovino, M., Di Laora, R. & Iodice, C. (2022). Simple approaches for piled foundations under combined axial-moment loading. *Proc. 20th Int. Conf. on Soil Mech. and Geotec. Eng., Sydney.*

NUMERICAL MODELLING OF THE CYCLIC RESPONSE OF BRIDGE PIERS SUBJECTED TO FOUNDATION SCOUR

A. Ciancimino[1] and A. Gajo[2]
[1] Politecnico di Torino, Torino, Italy
[2] Università di Trento, Trento, Italy

1. Introduction

The localized erosion of soil usually taking place around bridge piers strongly affects the lateral resistance of their foundation system. Local scour phenomena have been extensively studied from a hydraulic point of view. However, few studies have focused on the effects of scouring on the mechanical response of the foundation.

The study presented herein investigates numerically the effects of both local and general scour on the cyclic response of a bridge pier supported on a caisson foundation. In particular, numerical simulations are performed to reproduce the results of a series of centrifuge tests [1]. The purpose of this comparison is twofold: on the one side it serves as a validation of the numerical model, on the other, it provides interesting insights into the cyclic behaviour of scoured caisson foundations.

2. Methodology

The numerical simulations are developed considering the physical model employed in ref. [1] to study the horizontal behaviour of an idealized bridge pier. The latter consists of a SDOF system supported on a cylindrical foundation of diameter 2 m, embedded by 2 m in a layer of dense sand. The deck is represented by a concentrated mass chosen to achieve a vertical safety factor of 8. To focus on the foundation response under rocking motion, the pier is modelled as a rigid slender structure, with a height of 6.9 m. This study refers to the first group of cycles applied by [1], consisting of 10 quasi-static sinusoidal cycles with a displacement amplitude of 2.5 cm.

The nonlinear sand response is modelled employing the Severn-Trent model, as proposed in ref. [2]. The model is implemented as a user-defined material in the finite element code ABAQUS. The constitutive parameters adopted in this study are defined based on a thorough calibration procedure performed considering soil element tests either as representative of the actual material behaviour or as boundary value problems (see [3]). Consistently with the centrifuge tests, the analyses are performed under drained conditions. An isotropic linear elastic constitutive law is adopted for the foundation, whereas a purely frictional contact algorithm is used to model the soil-structure interface, allowing sliding and detachment.

3. Research outcomes

The results of the simulations are compared to the centrifuge tests in Figure 1 in terms of cyclic rocking stiffness $K_{r,c}$, hysteretic damping ratio $\xi_{r,h}$, and accumulated settlement per cycle w_c. Foundation scour strongly affects the foundation response, leading to a reduction of $K_{r,c,}$ especially in the case of a generalized erosion of the riverbed (Figure 1.a). It is interesting to notice that $K_{r,c}$ progressively increases from its monotonic value during the initial loading cycles. Under fully drained conditions, the application of multiple cycles of the same amplitude leads to progressive "sand densification" and, consequently, to an increase in soil stiffness. The downside is the progressive accumulation of settlements below the footing (Figure 1.c). Such an accumulation is more pronounced for the foundation subjected to general scour, while local scour seems to be less relevant. The soil response tends however to stabilize at some stage, and the foundation behaviour begins to level off.

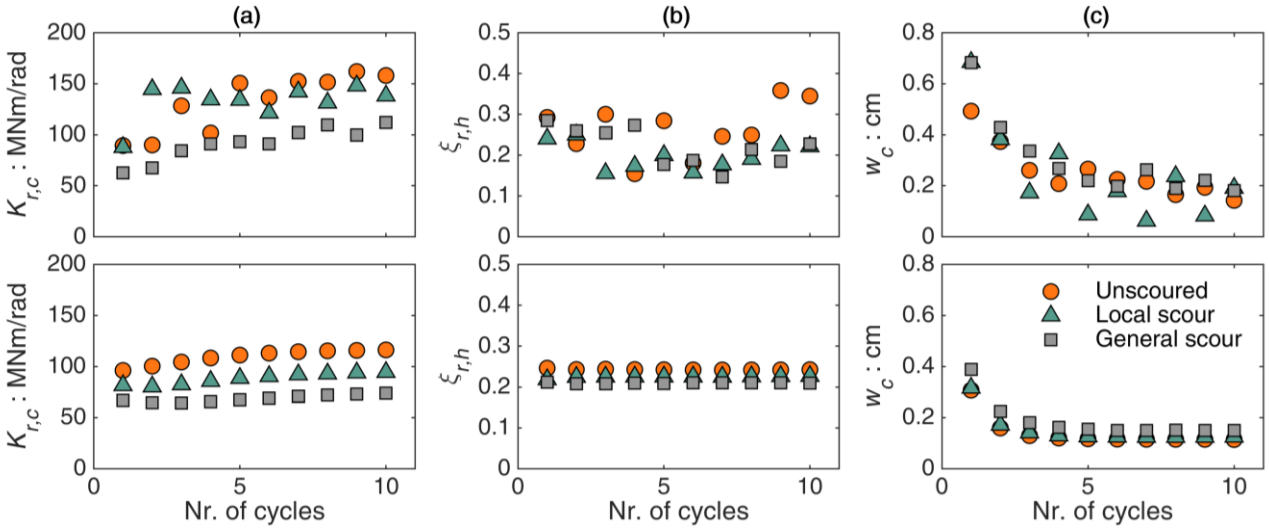

Figure 1. Centrifuge tests (top) vs numerical simulations (bottom): (a) $K_{r,c}$; (b) $\xi_{r,h}$; (c) w_c.

As regards $\xi_{r,h}$, the comparison is quite satisfying in terms of average measured values (Figure 1.b). $\xi_{r,h}$ seems not to vary significantly with the number of loading cycles, while it slightly decreases due to scouring.

The trends previously described can be identified in the results of both the numerical simulations and the centrifuge tests. However, some differences are observed, especially when comparing the evolution of $K_{r,c}$. The hardening rate of $K_{r,c}$ as predicted by the numerical model rapidly decreases after the firs fewt loading cycles, in contrast to the centrifuge tests. To better explain these differences further clarifications are required regard the nature of the "sand densification" effects. In general, two complementary phenomena contributing to the hardening of the foundation response can be identified. On the one hand, actual sand densification (in terms of reduction of the void ratio) takes place in the soil below the footing. On the other, the loading reversals lead to the rearrangement of the soil microstructure and, thus, to changes in the material fabric. The soil constitutive model, as in the version adopted here, is only able to partially capture the hardening of the foundation response (basically the part induced by the void ratio reduction), as it lacks sufficient "memory" to reproduce the the evolution of fabric effects over many cycles.

The abovementioned soil behaviour is relevant when a large number of loading cycles of almost constant amplitude is applied to the structure. However, when dealing with problems that mainly involve a small number of loading cycles of different amplitudes (for instance in the case of bridge foundations subjected to seismic loadings) the progressive hardening becomes less relevant. Overall, the comparison between the numerical simulations and the centrifuge tests has confirmed the ability of the soil constitutive model in predicting the main aspects of the foundation response for a wide range of loading conditions. More importantly, the numerical model is able to properly capture the effects of both general and local scour on the performance of the pier.

5. References

[1] Ciancimino, A., Jones, L., Sakellariadis, L., Anastasopoulos, I. & Foti, S. (2021). Experimental assessment of the performance of a bridge pier subjected to flood-induced foundation scour, *Géotechnique*, **72**(12), 998-1015.

[2] Gajo, A. (2010). Hyperelastic modelling of small-strain stiffness anisotropy of cyclically loaded sand. *Int. J. Numer. Anal. Methods Geomech.*, **34**(2), 111-134.

[3] Ciancimino, A., Anastasopoulos, I., Foti, S. & Gajo, A. (2022). Numerical modelling of the effects of foundation scour on the response of a bridge pier, *Acta Geotech.* **17**, 3697–3717.

USE OF THE MATERIAL POINT METHOD TO SOLVE THE BOUNDARY-VALUE PROBLEMS OF SOIL MECHANICS

R. Salgado[1], M. Prezzi[1]and V. Bisht[2]
[1] Purdue University, Ind., United States
[2]Align Technology Morrisville, NC, United States

1. Introduction

The boundary-value problems (BVPs) of soil mechanics have been notoriously challenging to solve rigorously. The mechanical response of soil is highly nonlinear, shear localization is common, and the resulting mesh distortion is problematic to handle using approaches such as the finite element method when paired with complex constitutive models. The material point method (MPM) has proven to be a useful option in such cases.

This extended abstract covers the main features of the MPM approach that we have used to solve the BVPs of soil mechanics.

2. General aspects of the MPM formulation

Our MPM formulation (coded in our in-house program, GeoNAP) is based on the uniform generalized interpolation material point method ("GIMP") variant of MPM discussed in detail in [1-4]. In GIMP, material points, from a discretization perspective, are not truly points, but finite size particles, usually squares in two dimensions. The greatest advantage of GIMP when compared to classical MPM, which relies on actual points, is natural avoidance of the instability that appears when material points cross from one element to the next. In MPM, space and matter are discretized separately. Space is discretized using a computational grid, and the soil and any other body in contact with it is discretized using material points. The grid can be a rectangular grid with elements sufficiently small where shear strain localization is expected. Material point discretization is achieved derivatively: the initial number of material points per element is fixed across the grid (e.g., four material points per element), and finer discretization is therefore achieved where the grid is itself made finer.

There are two other aspects of discretization that should be highlighted. First, the grid can be set up so that part of it moves (useful when simulating penetration problems [3], for example, when part of the mesh is set up to move with the penetrometer, keeping the same level of discretization around the penetrometer for the duration of the simulation), while another part may compress to accommodate that motion. Second, when material points flow from one grid element into another element for which they are too large, they are split in a way that conserves energy, momentum and mass [1].

Displacement or velocity boundary conditions are applied to the background grid nodes, whereas tractions are applied to the edges of material points that are at the boundaries of the material domain, from which they are mapped to the element nodes [2].

The fundamental governing equation is the momentum balance equation, which is solved using an explicit integration formulation [3]. Additional complications are handled when 2-phase simulations are required, such as problems involved saturated clay when effective-stress based constitutive models are used or when partial drainage is of interest [5,6].

Lastly, there are some challenges that are particular to MPM, having been well handled in FEM for considerable time. One is traction application, referred to earlier. The other is volumetric locking, which appears when a soil is at critical state, in problems involving incompressibility

because of the particular constitutive model used, or when collapse loads are to be calculated. In FEM, two popular ways to resolve the mismatch between the number of degrees of freedom and the number of constraints resulting from incompressibility are the use of higher-order elements or the use of reduced integration. These do not work in MPM because unphysical results may occur when higher-order elements are used (such as negative mass at a node) and because the number of material points within an element cannot be constrained, which is required for reduced integration. Both of these results follow from the freedom that material points have to move within and across elements. We have addressed volumetric locking by calculating volumetric strains at the center of elements instead of at material points using an MPM adaptation of the B-Bar method [4].

3. Application to BVPs

The present MPM formulation has been tested extensively against benchmark problems. Figures 1(a) and 1(b) show the results obtained for the classic Prandtl punch problem and cone penetration in clay performed using an advanced constitutive model [7]. The results of these tests have been reassuring, and comparisons against results of calibration chamber tests have started [6].

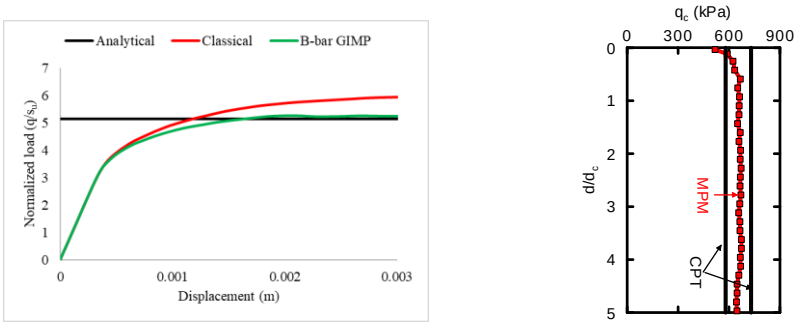

Figure 1. Validation of MPM formulation: (a) solution of the Prandtl punch problem using MPM ("Classical" means no volumetric locking scheme implemented); (b) comparison of cone resistance q_c during a penetration path $5d_c$-long with the values measured in two CPT soundings in a clay deposit.

4. References

[1] Woo, S.I. and Salgado, R. (2018). Simulation of penetration of a foundation element in Tresca soil using the generalized interpolation material point method (GIMP). Computers and Geotechnics, 94, 106-117.

[2] Bisht, V. and Salgado, R. (2018). Local transmitting boundaries for the material point method. *International Journal for Numerical Methods in Engineering*, 114(11), 1228-1244.

[3] Salgado, R., and Bisht, V. (2021). Advances in the solution of geotechnical boundary-value problems. Computers and Geotechnics, 138, 104183.

[4] Bisht, V., Salgado, R., and Prezzi, M. (2021). Simulating penetration problems in incompressible materials using the material point method. Computers and Geotechnics, 133, 103593.

[5] Bisht, V., Salgado, R., and Prezzi, M. (2021). Material Point Method for Cone Penetration in Clays. Journal of Geotechnical and Geoenvironmental Engineering, 147(12), 04021158.

[6] Salgado, R., Bisht, V., and Prezzi, M. (2022). Material Point Method simulations of cone penetration and CPT interpretation. Cone Penetration Testing 2022, 16-27.

[7] Chakraborty, T., Salgado, R. and Loukidis, D. (2013). A two-surface plasticity model for clay. Computers and Geotechnics, 49, 170–190.

NUMERICAL MODELING OF EXCAVATION PROCESSES IN SOFT SOILS USING THE PARTICLE FINITE ELEMENT METHOD

A. Leon Bal and G. Meschke
Ruhr University Bochum, Bochum, Germany

1. Introduction

This contribution presents a numerical model for the simulation of mechanized excavations in dry and water-saturated soft soils. The model combines single- and two-phase Finite Element formulations with a hypoplastic model within the framework of the Particle Finite Element Method (PFEM). The proposed hypoplastic PFEM model is validated by means of representative geotechnical examples and utilized for the computational analysis of cutting tool-soil interactions and mechanized excavations via Tunnel Boring Machines (TBMs).

2. Numerical model

Single-phase velocity-based [1] and coupled two-phase velocity-pressure stabilized [2] Finite Element formulations written in Updated Lagrangian (UL) description are presented for the solution of mechanical and hydromechanical problems, respectively. The two-phase formulation is based on the Theory of Porous Media (TPM) [3]. It is reduced from the three-field (displacement-water pressure-air pressure) FEM formulation proposed by Nagel and Meschke [4] using a "passive air-phase" approach and neglecting the development of excess air pore pressures in the system.

The proposed numerical formulations are implemented into the Particle Finite Element Method (PFEM) [5], suitable for the modeling of very large deformations. The PFEM is an UL FEM-based methodology which incorporates a global remeshing strategy and the α-shape technique [6] for boundaries identification. The PFEM is enhanced with an adaptive mesh refinement procedure proposed by the authors in [2] for the treatment of strain localization patterns in dense soils.

The mechanical behavior of the solid skeleton is characterized by means of a rate-independent hypoplastic model for sands [7], which relates the rate of deformation tensor $\boldsymbol{d}$ to the the effective Jaumann stress rate $\mathring{\boldsymbol{\sigma}}'$ via $\mathring{\boldsymbol{\sigma}}' = \boldsymbol{H}(\boldsymbol{\sigma}', \boldsymbol{d}, e)$, where $\boldsymbol{H}$ is a non-linear tensorial function and e is the void ratio. For hydromechanical problems involving partially saturated soils, the Soil Water Characteristic Curve (SWCC) is defined according to the van Genuchten's model, while the saturated hydraulic conductivity k_w^{sat} is computed using the Kozeni-Carman model [8], which incorporates the influence of the porosity and granulometry of the material into the estimation of k_w^{sat}.

3. Computational simulations of mechanized excavations in soft soils

Figure 1 (left) presents measured (left-top) and computed (left-bottom) ground deformations resulting from the interaction between a rigid mobile tool and partially saturated dense sand, at a tool horizontal displacement of $S_x = 450$ mm. The excavation experiments reveal the sequential activation of shear deformation bands emerging from the base of the tool. These shear bands are qualitatively captured by the PFEM model using the proposed adaptive mesh refinement scheme. The computed topology of the excavation profile at tool displacements of $S_x = 250$ mm and 450 mm (Fig. 1 (center-top)), and the computed tool reaction forces assuming dry and partially saturated soil conditions (Fig. 1 (center-bottom)), are also evaluated and compared against experiments. For the considered displacement range of the tool, model predictions and experimental results are in good agreement. Finally, Fig. 1 (right) displays simulation results of mechanized excavations performed in dry weathered granite using a submodel of an Earth Pressure Balance (EPB) TBM. The submodel considers only a

section of the tunnel and one spoke of the cutterhead. The spatial distribution of out-of-plane displacements (Fig. 1 (right-top)) show how the spoke penetrates the soil and excavates the tunnel face. The predicted total cutterhead torque is also analyzed in (Fig. 1 (right-bottom)). Good agreement with respect to the reference numerical solution adopted for this application [9] is obtained.

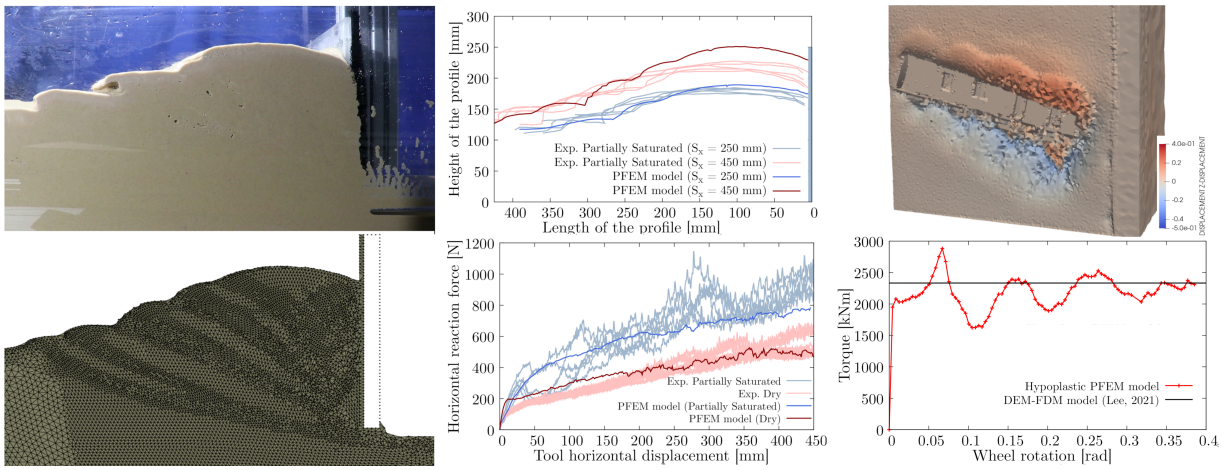

Figure 1. Mechanized excavations in soft soils: Tool-soil interactions in soft soil; Experiments (left-top), simulations (left-bottom), topology of the ground surface at two excavation stages (center-top) and tool reaction forces (center-bottom). Simulations of dry excavations using an EPB TBM; out-of-plane tunnel face deformations (right-top) and total cutterhead torque (right-bottom).

References

[1] Franci, A., Oñate, E., and Carbonell, J. M. (2016). Velocity-based formulations for standard and quasi-incompressible hypoelastic-plastic solids. *International Journal for Numerical Methods in Engineering*, **107**, 970–990, nme.5205.

[2] Leon, A. R. and Meschke, G. (2022). Two-phase particle finite element model for the coupled analysis of cutting tool-soil interaction in partially saturated soft soils. *International Journal for Numerical and Analytical Methods in Geomechanics*, **1**, 1–42, under review.

[3] de Boer, R. and Ehlers, W. (1986). *Theorie der Mehrkomponentenkontinua mit Anwendung auf bodenmechanische Probleme*. Univ.-Gesamthochschule.

[4] Nagel, F. and Meschke, G. (2010). An elasto-plastic three phase model for partially saturated soil for the finite element simulation of compressed air support in tunnelling. *International Journal for Numerical and Analytical Methods in Geomechanics*, **34**, 605–625.

[5] Oñate, E., Idelsohn, S. R., Del Pin, F., and Aubry, R. (2004). The particle finite element method—an overview. *International Journal of Computational Methods*, **1**, 267–307.

[6] Edelsbrunner, H. and Mücke, E. P. (1994). Three-dimensional alpha shapes. *ACM Trans. Graph.*, **13**, 43–72.

[7] von Wolffersdorff, P.-A. (1996). A hypoplastic relation for granular materials with a predefined limit state surface. *Mechanics of Cohesive-frictional Materials*, **1**, 251–271.

[8] Chapuis, R. P. and Aubertin, M. (2003). Predicting the coefficient of permeability of soils using the kozeny-carman equation. Tech. rep., Polytechnique Montréal, 2500 Chemin de Polytechnique, Montreal, QC H3T 1J4 Canada.

[9] Lee, H., Choi, H., Choi, S.-W., Chang, S.-H., Kang, T.-H., and Lee, C. (2021). Numerical simulation of epb shield tunnelling with tbm operational condition control using coupled dem–fdm. *Applied Sciences*, **11**, 2551.

NUMERICAL ANALYSIS OF CPT IN STRUCTURED SOIL - PARAMETER CALIBRATION AND COMPARISON WITH IN-SITU DATA

H.F. Schweiger[1] and L. Hauser[2]
[1] Graz University of Technology, Graz, Austria
[2] Universitat Politècnica de Catalunya, Barcelona, Spain

1. Abstract

The simulation of cone penetration tests (CPT) is a challenge for numerical modelling because large deformations and large displacements have to be considered. In this work the Particle Finite Element Method code G-PFEM, which employs an updated Lagrangian description, is utilized. The well-known Clay and Sand Model (CASM), which is a model based on critical state soil mechanics principles, has been implemented in G-PFEM and extended to account for effects of bonding and destructuration. In this contribution it is shown that CPT results in structured soils can be reproduced with the employed constitutive model after calibration of parameters using oedometer tests of high-quality samples.

2. Numerical and constitutive model

The Particle Finite Element Method (PFEM, [1]) forms the basis for the application G-PFEM which is used in this work [2],[3],[4]. It has been developed within the Kratos framework at the Polytechnic University of Catalonia (UPC) and the Center for Numerical Methods in Engineering (CIMNE). It adopts an updated Lagrangian description, i.e. frequent remeshing of critical regions is performed. In order to overcome the issue of locking associated with low order elements a mixed, stabilized formulation of the problem is used. An example of a typical finite element model at the end of an analysis is shown in Figure 1. The cone is modelled as rigid material and has a radius R of 1.78 cm with a tip angle of 60° corresponding to the standard geometry (base area of 10 cm^2). The constitutive model adopted is the well-known Clay and Sand Model (CASM) proposed in [4], which is a state parameter based, elastic-plastic critical state (CS) model. It has been enhanced to account for structure and destructuration based on the concepts proposed in [5] as depicted in Figure 1.

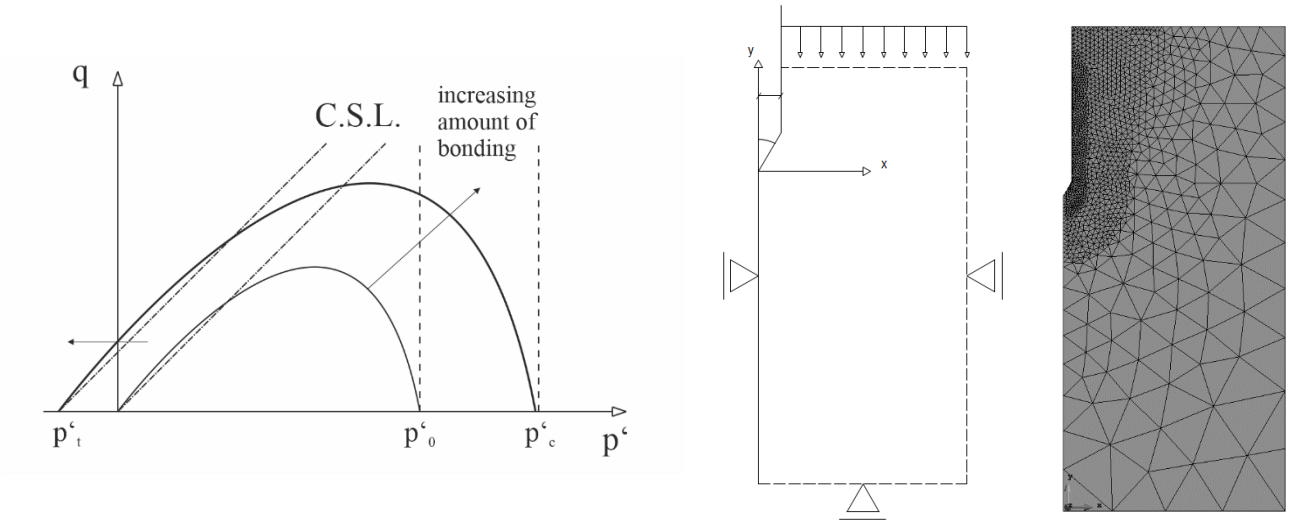

Figure 1. Yield surface of CASM with structure and axisymmetric finite element model

3. Test Site "Seekirchen"

The test site Seekirchen is located in the municipality of Seekirchen northeast of Salzburg, Austria. The soil layer considered in this study is a clayey silt, locally known as "Seeton". High-quality block samples could be taken, and these clearly showed the existence of structure when tested in an oedometer device (Figure 2). In order to calibrate the parameters for the CASM a series of analyses has been performed varying stiffness parameters, but in particular the degree of bonding (denoted by the parameter b_0) and the rate of destructuration (denoted by parameters h_v and h_d for volumetric and deviatoric contributions respectively). As show in Figure 2 a good agreement between oedometer results and numerical analysis could be obtained. The intrinsic curves are represented by setting $b_0 = 0$ whereas h_v and $h_d = 0$ represent calculations assuming that there is no destructuration. This set of parameters was then adopted for comparing in-situ CPT measurements with numerically simulated CPT. It is obvious that results assuming no structure ($b_0 = 0$) yield far too low tip resistance and results assuming no destructuration (h_v and $h_d = 0$) yield too high tip resistances, confirming that realistic results can only be obtained employing a constitutive model which can take into account structure and destructuration.

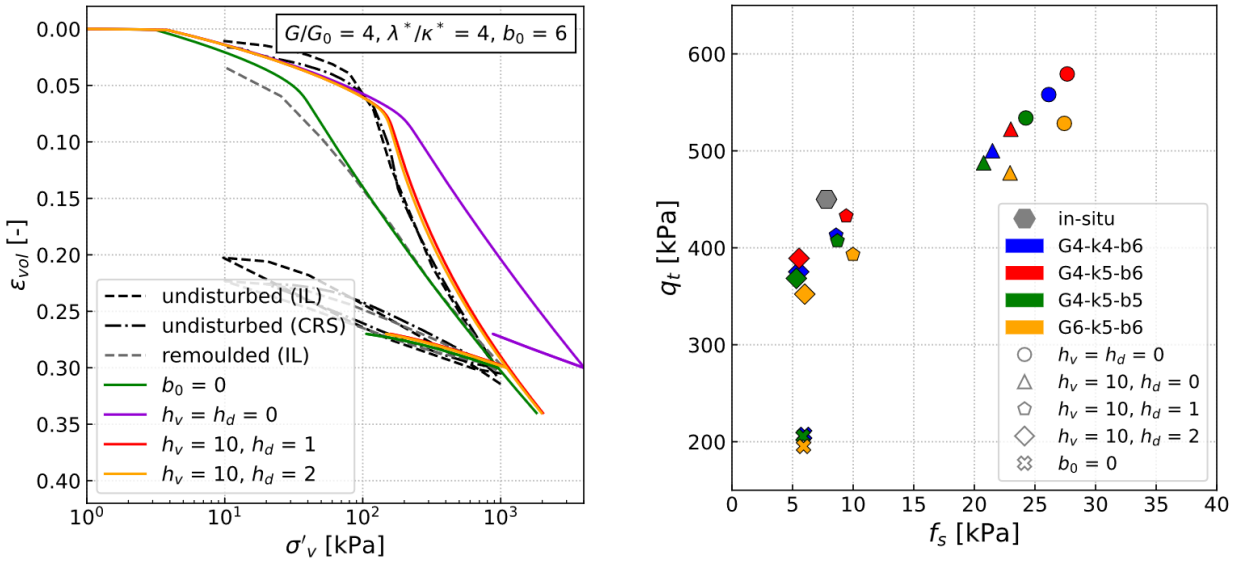

Figure 2. Comparison of oedometer test and CPT with numerical analysis

4. References

[1] Oñate, E., Idelsohn, S.R., Celigueta, M.A., Rossi, R., Marti, J., Carbonell, J.M., Ryzakov, P., Suárez, B. (2011). Advances in the particle finite element method (PFEM) for solving coupled problems in engineering. *Particle-Based Methods* **25**, 1-49.

[2] Monforte, L., Carbonell, J.M., Arroyo, M., Gens, A. (2017b). Performance of mixed formulations for the particle finite element method in soil mechanics problems. *Computational Particle Mechanics* **4**, 269–284.

[3] Monforte, L., Arroyo, M., Carbonell, J.M., Gens, A. (2018). Coupled effective stress analysis of insertion problems in geotechnics with the Particle Finite Element Method. *Computers and Geotechnics* **101**, 114-129.

[4] Yu, H.S. (1998). CASM: a unified state parameter model for clay and sand. *Numerical and Analytical Methods in Geomechanics* **22**, 621-653.

[5] Gens, A. Nova, R. (1993). Conceptual base for a constitutive model for bonded soils and weak rocks. *Proceeding of the International Symposium on Geotechnical Engineering of Hard Soils-Soft Rocks*, Athens Vol. 1, 485-494.

FINITE STRAIN G-PFEM SIMULATION OF PILE INSTALLATION IN CHALK

M. O. Ciantia and M. Previtali
School of Science and Engineering, University of Dundee, Dundee, UK

1. Introduction

Chalk is a highly porous rock formed by cemented calcite grains. It covers large areas of the UK and is widespread under the North Sea where offshore wind turbines (OWT) are currently being installed and where future offshore expansion will be sited (Fig. 1a) [1]. Large piles are often driven in chalk to support OWT. The installation process causes the intact rock below the pile tip to crush into a putty characterised by a mechanical behaviour very different from the intact chalk. The difficulty to predict the final state of the putty and the stress around the pile after installation is the underlying reason for inadequate current design guidance for piles in chalk. Considering that, for OWT, foundations account for 20-25% of the total development cost, pile design improvements in chalk would be extremely beneficial from an economical and environmental perspective.

Current guidelines for the design of piles in chalk (CIRIA C574) originate from the analysis of a limited number of pile tests [2]. These guidelines suggest average unit shaft resistance (τ_{sf}) design values ranging between 20 and 120 kPa for low-medium density and high/very-high density chalk, respectively. These estimates of τ_{sf} are typically very conservative, hence introducing significant increases in cost and carbon footprint (Fig. 1b). Reducing the level of conservatism (e.g. enabling more confident use of higher τ_{sf} values) would reflect in significant savings of steel and consequent reduction of the cost and embodied carbon. Such design considerations are possible but require a better understanding of the long-term mechanical effects of the damage processes that intact chalk experiences during dynamic pile installation, involving coupled hydro-mechanical (HM) conditions.

In this work the coupled HM effects developing during pile installation in chalk are investigated numerically using a robust and mesh-independent implementation of an elasto-plastic constitutive model at large strains. The model, implemented into an open-source Geotechnical Particle Finite Element (G-PFEM) code [3], is shown to be able to capture the damage of the rock until the formation of a chalk putty layer around the shaft of a model piles jacked in chalk.

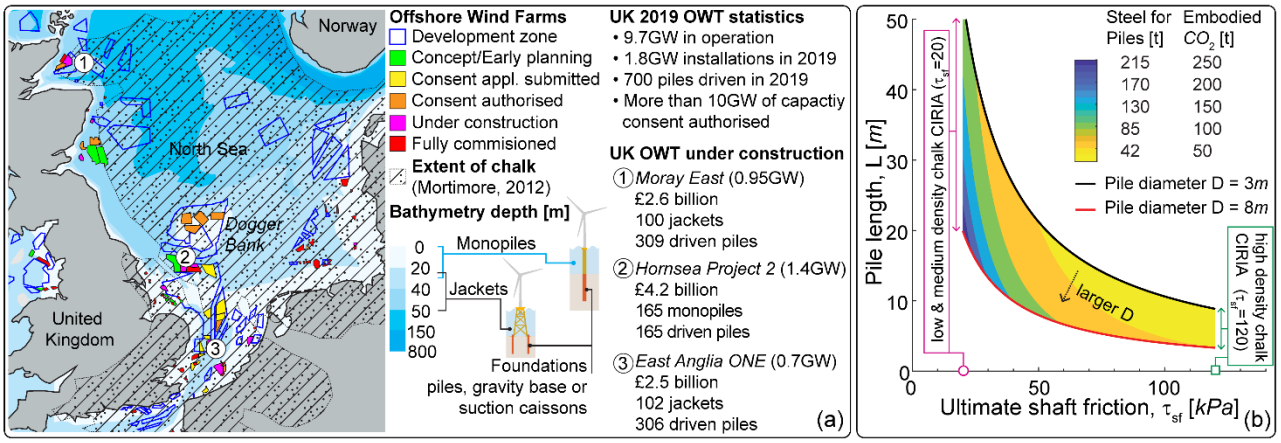

Figure 1 North Sea OWT development (www.4coffshore.com) along with sea water bathymetry, extent of chalk [4]. (b) Embodied CO_2 and steel tonnages as a function of design interface chalk-steel strength, pile length *L* and diameter *D*. Diagram developed for a pile design axial capacity of 10MN after [1].

2. G-PFEM coupled jacking installation of closed and open-ended piles

The complex flow and deformation processes occurring in the soil around both open and closed ended piles of variable shape jacked into saturated chalk are investigated numerically. A fully coupled HM formulation, based on regularized, mixed low-order linear strain triangles is used [5]. To capture the relevant features of the mechanical response of chalk, a finite deformation, non-associative structured modified Cam Clay model is used. The model formulation is based on a multiplicative decomposition of the deformation gradient and on the adoption of an hyperelastic response, assuming the existence of a suitable free energy function. Bonding-related internal variables, quantifying the effects of structure on the yield locus size and position, are used to provide a macroscopic description of mechanical destructuration effects. To deal with strain localization phenomena, the model is equipped with a non-local version of the hardening laws. The G-PFEM model is shown to be capable of capturing: the destructuration associated with plastic deformations below and around the pile shoulder; the space and time evolution of pore water pressure as the pile advances; the effect of soil permeability on predicted excess pore water pressures, and the effect of chalk putty formation on predicted values of the load displacement curve. Installation effects are highlighted by comparing the axial performance between wished in place piles and piles for which the full installation process is simulated. Fig. 2a shows this effect for cone-ended piles jacked in chalk, while in Fig. 2b snapshots are provided showing the deformed mesh of open-ended piles jacked at different rates.

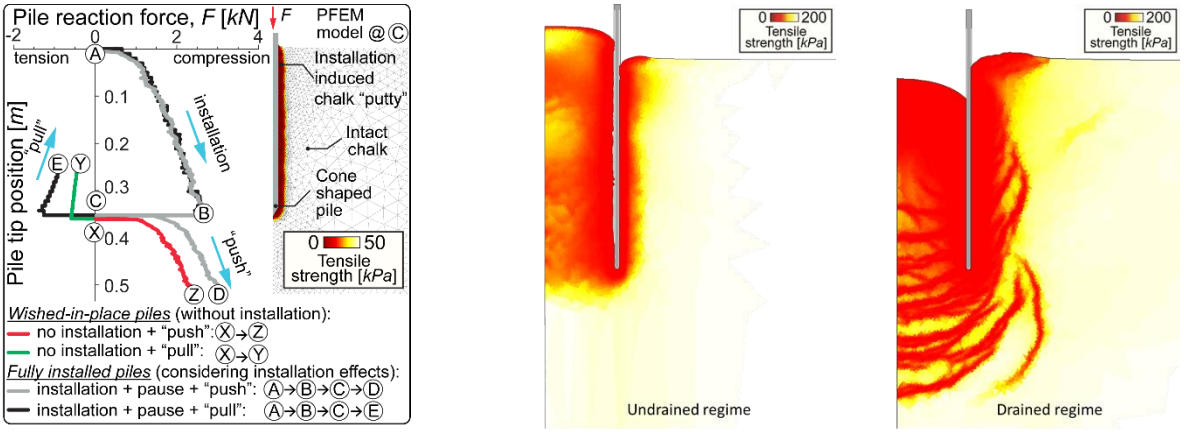

Figure 2 (left) Installation effects on axial performance of model pile in chalk and (right) different plugging mechanisms developed depending on pile jacking rate.

Acknowledgments

This work is funded by the EPSRC New Investigator Award ICE-PICK project (EP/W00013X/1)

References

[1] Ciantia, M. O. (2022). Installation Effects on Axial Performance of Monopiles in Chalk for Offshore Renewables. In Proc. of the 2nd VSOE (pp. 424-432). Springer Singapore.

[2] Lord, J.A., Clayton, C.R.I., Mortimore, R.N. (2002). *Construction Industry Research and Information Association*. Engineering in chalk. CIRIA

[3] Carbonell, J. M., Monforte, L., Ciantia, M. O., Arroyo, M., & Gens, A. (2022). Geotechnical particle finite element method for modeling of soil-structure interaction under large deformation conditions. *JRMGE*, **14**(3), 967-983.

[4] Mortimore, R.N. (2012). *Making sense of Chalk: a total-rock approach to its Engineering Geology*. Q. J. Eng. Geol. Hydrogeol. **45**(3), 252–334

[5] Monforte, L., Arroyo, M., Carbonell, J.M., Gens, A. (2018). Coupled effective stress analysis of insertion problems in geotechnics with the Particle Finite Element Method. *Comput Geotech*, **101**, 114–129

NUMERICAL MODELLING OF GROUND FREEZING-THAWING CYCLE IN TUNNELING

R. J. Williams M. and G. Meschke
Institute for Structural Mechanics, Ruhr University Bochum, Germany

1. Introduction

This contribution presents a computational model for soil freezing to investigate the effects of a freezing-thawing cycle on the hygro-thermal analysis of ground freezing in tunnelling. The model is formulated based on the theory of poromechanics of freezing materials and discretized using the multi-field thermo-hygro-mechanical finite element method. A numerical study of artificial ground freezing in tunnelling is presented considering active freezing, tunnel excavation, and natural thawing phases.

2. Numerical Modelling of Freezing of Fully Saturated Soils

2.1. Governing balance equations

The main governing equations for the freezing of fully saturated soil are the overall momentum balance, the mass balance of liquid water and crystal ice, and the overall entropy balance, Eq. (1), Eq. (2) and Eq. (3) respectively, see [1].

$$\nabla \cdot \boldsymbol{\sigma} + \rho \boldsymbol{g} = \mathbf{0} \tag{1}$$

$$\frac{dm_L}{dt} + \frac{dm_C}{dt} + \nabla \cdot \boldsymbol{w}_{\mathrm{L}} = 0 \tag{2}$$

$$T(\frac{dS}{dt} + \nabla \cdot (s_L \boldsymbol{w}_{\mathrm{L}})) + \nabla \cdot \boldsymbol{q} - \Phi_M = 0 \tag{3}$$

2.2. Constitutive relations

Liquid-crystal equilibrium relation: The liquid-crystal equilibrium condition is given by Eq. (4) where p_C is the ice crystal pressure, p_L is the liquid pressure, S_f denotes the freezing entropy per unit of volume, T_f is the bulk freezing temperature and T is the current temperature.

$$p_C - p_L = S_f \left(T_f - T\right) , \tag{4}$$

Liquid saturation curves for freezing-thawing cycles: The hysteresis behavior of the liquid saturation χ_L in the process of freezing-thawing cycles is incorporated by the hysteresis model for unfrozen liquid content developed in ref. [2].

Viscoelastic logarithmic creep model for frozen soil: The macroscopic creep model takes into account the microstructure of the frozen soil, which is composed by ice, soil, water material phases, by the homogenization of the elastic and viscoelastic properties of the phases, see [3], [4].

2.3. Thermo-hygro-mechanical Finite Element formulation

Mixed finite element method is used for spatial discretazion where the primary variables are the displacement **u**, liquid pressure p_L and temperature T. The temporal discretization of the equations system is formulated using the generalized-α time integration scheme. The complete details of the finite element formulation are provided in ref. [5].

3. Numerical example

In this section a model test of the horizontal ground freezing of twin tunnels is re-analyzed numerically [6], see Fig.1 (a). The physical modelling considers the sequential freezing mode of the uplink and downlink twin tunnels. In the numerical analysis, the temperature distribution and the closure time of the frozen wall are computed, see Fig.1 (d) and (c). Fig. 1 (b) shows good qualitative agreement between the computed temperatures and temperatures measured at monitoring points located around the uplink tunnel.

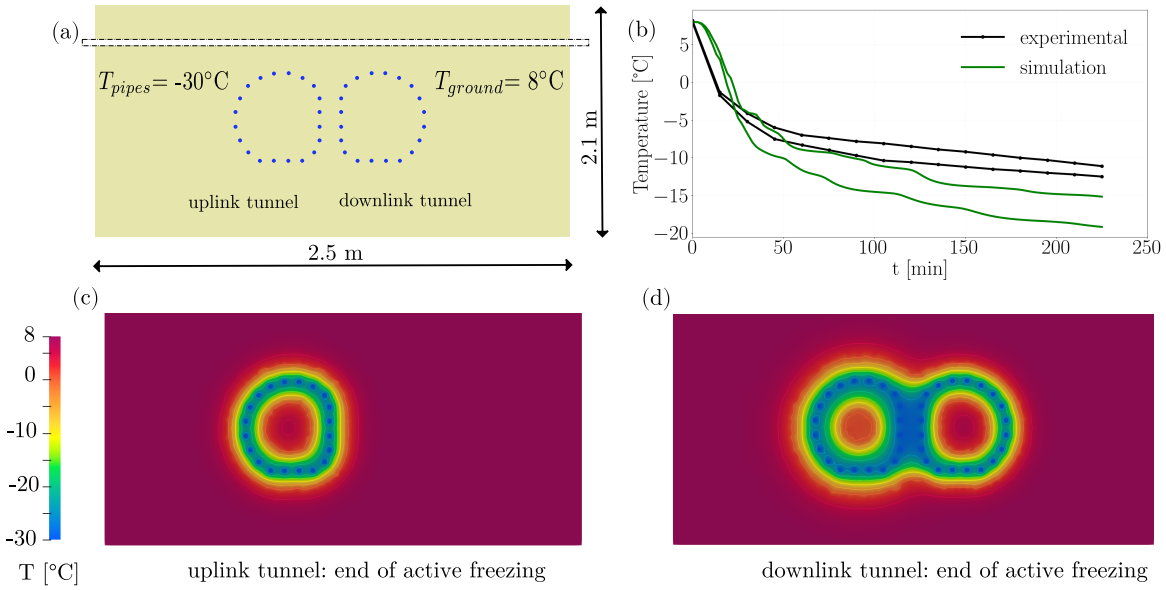

Figure 1. Model test for horizontal ground freezing of twin tunnels. (a) Model set-up and initial conditions. (b) Comparison of temperature evolution at the monitoring points located at the uplink tunnel. Temperature distribution: end of the active freezing phase of the uplink tunnel and of the downlink tunnel, (c) and (d) respectively.

4. Citing references

References

[1] Coussy, O. (2005). Poromechanics of freezing materials. *J. Mech. Phys. Solids*, **53**, 1389–1718.

[2] Saberi, P., Koenig, C., and Meschke, G. (2021). A hysteresis model for the unfrozen liquid content in freezing porous media. *Computers and Geotechnics*, **134**, 104048.

[3] Lackner, R., Pichler, C., and Kloiber, A. (2008). Artificial Ground Freezing of Fully Saturated Soil: Viscoelastic Behavior. *Journal of Engineering Mechanics*, **134**, 1–11.

[4] Williams M., R. J. and Meschke, G. (2019). Computational modelling of creep and rate dependent strength of freezing soils. *8th GACM Colloquium on Computational Mechanics For Young Scientists From Academia and Industry*, August, pp. 97–100, kassel university press.

[5] Zhou, M.-M. and Meschke, G. (2013). A three-phase THM coupled FE model for freezing soils. *International Journal for Numerical and Analytical Methods in Geomechanics*, **37**, 3173–3193.

[6] Cai, H., Li, S., Liang, Y., Yao, Z., and Cheng, H. (2019). Model test and numerical simulation of frost heave during twin-tunnel construction using artificial ground-freezing technique. *Computers and Geotechnics*, **115**.

NUMERICAL ANALYSIS OF TUNNEL FACE STABILITY IN NON-COHESIVE MATERIALS WITH AN INNOVATIVE CONSTITUTIVE MODEL

***L.P. Argani*[1,2], *L. Chino*[1] *and A. Gajo*[1]**

[1] *Department of Civil, Environmental and Mechanical Engineering, University of Trento, Italy*

[2] *Department of Mathematical Sciences, University of Liverpool, UK*

1. Introduction

Tunnel face stability is generally of great concern in tunnel excavation with both traditional methods and with modern tunnel boring machines (TBMs). Several methods have been proposed in the literature for the analysis of face stability [1, 2], which are generally based on the limit equilibrium method and on different assumptions of the failure mechanisms. The major uncertainties typically concern the purely frictional materials. The aim of this work is to analyse the tunnel face stability in non-cohesive soil by employing the finite element method (FEM) with the constitutive model recently proposed by Argani & Gajo [3], and to compare the computed failure mechanisms and support forces with the results proposed in literature [1, 2].

2. Methods

FEM is employed to model the tunnel for a prescribed value of tunnel diameter $D = 6.5\,\mathrm{m}$ (circular cross-section) and overburden levels ($0.5D$, $1.2D$, and $2D$). For the sake of simplicity, the soil is assumed homogeneous and non-cohesive, for which a perfectly plastic Mohr-Coulomb yield surface with rounded corners and edges [4] is assumed as the failure criterion. In particular, to enhance the numerical convergence of such constitutive model for low mean stress states, the recent hyper-elastic formulation proposed by [3] is employed together with special line-search solution procedures. This constitutive model is implemented in a user defined subroutine for Abaqus Unified FEA [3].

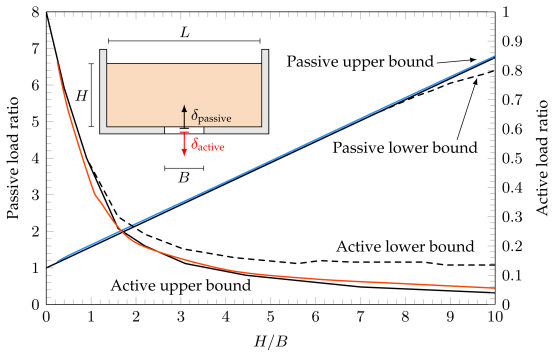

Figure 1. Reference scheme for the trapdoor problem and comparison of the limit load obtained with the Argani & Gajo [3] constitutive model with upper and lower bound solutions [5].

The performance of this numerical tool has been preliminarily validated by analysing the problem of an active and a passive trapdoor (figure 1), which involve low stress states at soil failure conditions, in an analogous manner with respect to the tunnel face stability problem. Figure 1 shows that, assuming an associative framework, the agreement of model simulations with lower and upper bound solutions of the limit analysis method is excellent.

For the tunnel face stability problem, both plane strain and full 3D frameworks are considered; a friction angle of $35°$ was employed for the 3D simulations, whereas different values of the friction

angle (ranging from $5°$ to $50°$) have been investigated for the plane strain framework. The length of the tunnel excavation is assumed equal to 8 m and is supported by lining elements. The domain size is taken sufficiently large to avoid any boundary effect on the development of the failure mechanism. The analysis is performed in a static regime in two ways: i) controlling the displacement of the rigid wall (representative of the cutters) supporting the tunnel face, ii) controlling the pressure distribution of the conditioned soil mixture (e.g. bentonite slurry) supporting the tunnel face.

3. Results

The failure mechanisms obtained for the tunnel face are reported in figure 2. It can be noted (figure 2 left) that a well defined plateau in the displacement vs. support pressure/support force diagram is obtained thus ensuring the formation of a well defined failure mechanism. The continuous lines in figure 2 separate the zones affected by large displacements with respect to the surroundings and thus identify the collapse mechanism. It can be noted that the computed failure mechanism compares well with the failure lines postulated in some limit equilibrium methods proposed in the literature.

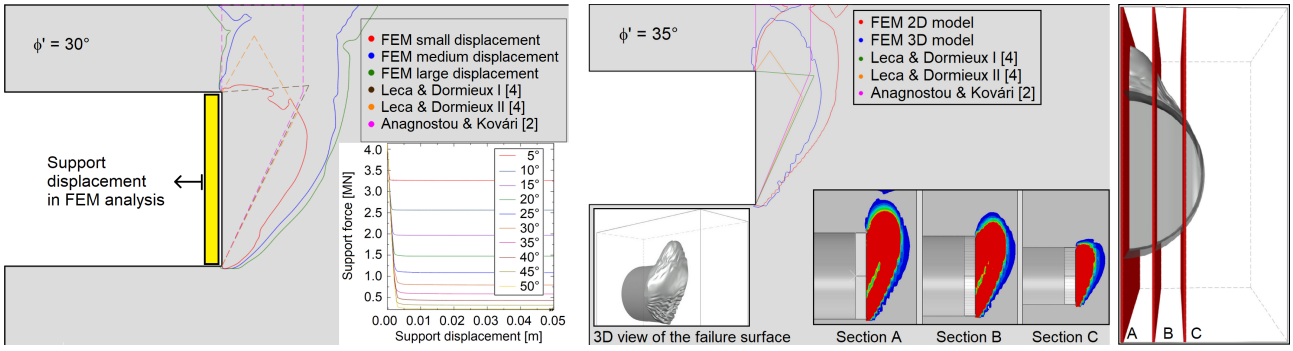

Figure 2. Results for the 2D (left) and 3D (right) modelling of the tunnel face in terms of failure mechanism and displacement-support force curves and comparison with literature results [1, 2].

Chimney formations are observed in the numerical simulations depending on the overburden level, as obtained with the limit equilibrium methods, thus leading to large subsidence at ground surface. It can be concluded that the FEM based modelling technique proposed in this study presents interesting preliminary results for the evaluation of the tunnel face stability and paves the way for more detailed analyses and a better understanding of this kind of failures.

References

[1] Anagnostou, G. and Kovári, K. (1996). Face stability conditions with earth-pressure-balanced shields. *Tunn. Undergr. Space Technol.*, **11**, 165–173.

[2] Leca, E. and Dormieux, L. (1991). Upper and lower bound solutions for the face stability of shallow circular tunnels in frictional materials: Leca, e; dormieux, l geotechniquev40, n4, dec 1990, p581–606. *Int. J. Rock Mech. Min. Sci. Geomech. Abstr.*, **28**, A255.

[3] Argani, L. and Gajo, A. (2021). A new isotropic hyper-elasticity model for enhancing the rate of convergence of mohr-coulomb-like constitutive models and application to shallow foundations and trapdoors. *Comput. Geotech.*, **132**, 103957.

[4] Abbo, A., Lyamin, A., Sloan, S., and Hambleton, J. (2011). A c2 continuous approximation to the mohr–coulomb yield surface. *Int. J. Solids Struct.*, **48**, 3001–3010.

[5] Smith, C. (1998). Limit loads for an anchor/trapdoor embedded in an associative coulomb soil. *Int. J. Numer. Anal. Meth. Geomech.*, **22**, 855–865.

SLIP LINE APPROACH TO ASSESS THE PLASTIC ZONE AROUND CIRCULAR OPENING EXCAVATED IN A HOEK-BROWN ROCK MASS

Y.-K. Lee
Kunsan National University, Gunsan, Jeonbuk, South Korea

1. Introduction

The Hoek-Brown (H-B) failure criterion is an empirical condition defining the maximum principal stress (σ_1) at failure as a non-linear function of confining pressure (σ_3). Its latest version, known as the generalized Hoek-Brown (GHB) criterion [1], incorporates the strength parameters m_b, s and a, which can be linked empirically to the field conditions of rock mass. This criterion has been widely used in rock engineering applications as it can predict conditions at failure more accurately than the linear Mohr-Coulomb (M-C) representation. In view of this, both the H-B and GHB criteria are attracting a lot of attention and have been applied to various practical engineering problems, including rock slope stability analysis [2] and the assessment of bearing capacity of foundations [3]. However, it is also true that the non-linear nature of the GHB criterion poses more mathematical difficulties than the M-C criterion and more research on its numerical and/or analytical implementation in a diverse range of rock engineering applications is needed.

This work presents a new slip line approach to assess the development of plastic zone around a circular tunnel subjected to a hydrostatic in-situ stress (σ_0). In the past, the M-C equation was commonly employed as the yield function for slip line analysis [4], whereas in this study, the GHB criterion is selected for the yield function. According to the slip line theory, at every point in the yielding zone, there exist two families of characteristic curves, called α- and β- lines, along which their respective invariants can be defined. For the GHB medium, the invariants can be expressed in terms of the direction of the major principal stress and the instantaneous friction angle (ϕ_i) of the GHB criterion [3]. It is shown that the construction of a network of characteristic curves around a circular tunnel in GHB rock mass can be done in a simple manner by invoking the fact that there exists a unique invariant for each characteristic curve, whereby the 2-D distributions of stress and strain as well as the radius of the yielding zone can be calculated. In the formulation, perfectly plastic behavior is assumed, and the effect of gravity is neglected.

2. Formulation for the construction of slip lines

Fig. 1 shows the circular tunnel model with radius b, where p_i is the supporting pressure and R_p is the radius of the yielding zone. This figure also shows the α- and β-lines starting at point A on the tunnel wall and ending at point B on the elastic-plastic boundary. σ_R and σ_θ are the radial and hoop stresses acting on the elastic-plastic boundary, respectively. For this model, the aforementioned invariants for the slip lines can be expressed as

$$\frac{a}{2(1-a)}\left[\cot\phi_i + \ln\left(\cot\frac{\phi_i}{2}\right)\right] \pm \omega = const. \tag{1}$$

where ω is the angle between the direction of major principal stress and the horizontal axis, while a is the GHB strength parameter. Then, it can be shown that the radial distance r to a point on the α-line can be related to θ as follows:

$$\frac{r}{b} = \exp\left[\frac{a}{2(1-a)}(\csc\phi_{i\theta} - \csc\phi_{iA})\right] \tag{2}$$

$$\theta = \frac{a}{2(1-a)}\left(\cot\phi_{i\theta} - \cot\phi_{iA} + \ln\left[\frac{\cot(\phi_{i\theta}/2)}{\cot(\phi_{iA}/2)} \right] \right), \quad \theta \in [0,\ \theta_{\max}] \tag{3}$$

where ϕ_{iA} and $\phi_{i\theta}$ are the tangential friction angles corresponding to the stress conditions at point A and the point of radial distance r, respectively. It should be noted here that $\theta_{\max}$ can be obtained by setting $\phi_{i\theta} = \phi_{iB}$ in Eq. (3).

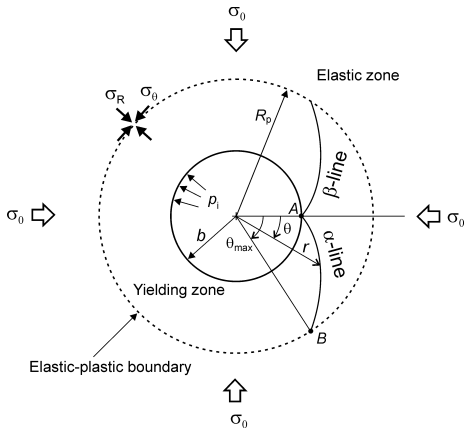

Fig. 1. Assumed tunnel model for slip line analysis

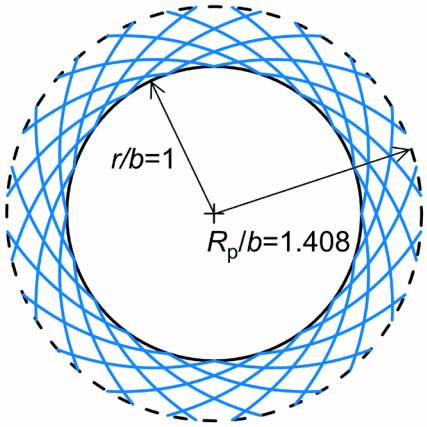

Fig. 2. Slip line network formed around a circular tunnel

3. Illustrative construction of slip line network and conclusions

Fig. 2 shows the slip line network constructed based on Eqns. (2) and (3) for $\sigma_0 = 10\text{MPa}$, $m_i = 15$, $D = 0$, $\sigma_{ci} = 20\text{MPa}$, GSI=60, and $p_i = 0$. The result clearly shows that the proposed formulation represents an accurate visualization of the geometry of slip lines formed around a circular tunnel. Once the slip line network is established, the calculations for the associated stress and strain distributions are straightforward. Although the presented formulation is restricted to the idealized axisymmetric 2-D circular tunnel, it could be conveniently employed for the stability analysis of a tunnel excavated in a joined rock mass in the earlier design stage.

4. Acknowledgement

This research was funded by the National Research Foundation of Korea (NRF) (No. 2021R1F1A1048311).

5. References

[1] Hoek, E., Carranza-Torres, C.T. & Corkum, B. (2002). Hoek-Brown failure criterion – 2002 edition, *Proc. 5th North American Rock Mech. Sympo*. Toronto.

[2] Park, D. & Michalowski, R.L. (2021). Three-dimensional stability assessment of slopes in intact rock governed by the Hoek-Brown failure criterion, *Int. J. Rock. Mech. Min. Sci.*, **137**, 104522.

[3] Serrano, A. & Olalla, C. (1994). Ultimate bearing capacity of rock masses, *Int. J. Rock. Mech. Min. Sci.*, **31**, 93–106.

[4] Davis, R.O. & Selvadurai, A.P.S (2005). *Plasticity and Geomechanics*, Cambridge University Press

NUMERICAL SIMULATION OF A CENTRIFUGE TEST ON SHALLOW TUNNEL CLOSE TO A SURFACE STRUCTURE

J. Zhang[1] and E. Bilotta[2]
[1] Xi'an Jiaotong University, Xi'an, China
[2] University of Naples Federico II, Naples, Italy

1. Introduction

Earthquake-induced liquefaction is a major concern for the seismic safety of all engineering structures. In this paper, the OpenSees platform is employed to construct a two-dimensional numerical model consisting of a rectangular tunnel and an adjacent surface structure in liquefiable Hostun sand [1]. The numerical model is validated against the centrifuge test data gathered by Miranda [2].

2. The centrifuge test

The test was conducted under a centrifugal acceleration of 60*g*. Thus, the physical model imitated a prototype 60 times larger, and all the specifications elaborated herein will be in the prototype scale unless stated otherwise. As illustrated in Figure 1(a), a rectangular tunnel was buried in saturated Hostun sand. The cross-section of the tunnel was 4.6 m in height and 9.2 m in width. The tunnel was supported by an aluminum lining with a uniform thickness of 360 mm. The total mass of the tunnel was 4.1×10^5 kg. A one-storey frame building with the mass of 2.1×10^5 kg, also made of aluminum, was placed adjacent to the tunnel. For the centrifuge test, a rigid container was adopted, with two absorbent layers of Duxseal material attached to the lateral sides to reduce the boundary effect. An aqueous solution of hydroxypropyl methylcellulose, with a viscosity 60 times that of water, was used to saturate the Hostun sand, therefore ensuring compatibility between the diffusion and the dynamic time.

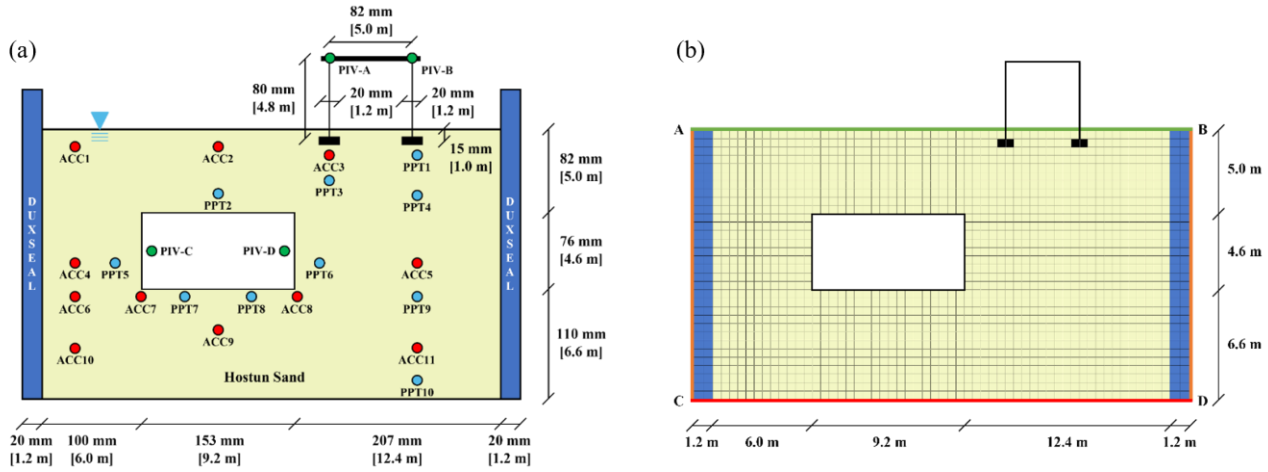

Figure 1. (a) Layout of the centrifuge model with prototype dimensions in brackets. (b) Mesh of the finite element model.

3. The numerical model

The plasticity model PM4Sand (Version 3.1) [3] is adopted to simulate the responses of the liquefiable Hostun sand. The constitutive parameters are calibrated to match a curve of cyclic resistance ratio, which is obtained through the cyclic deviator stress normalized by the effective confining stress in dynamic triaxial tests. The relative density of the Hostun sand is set to 66%. The permeability coefficient is assumed equal to 8×10^{-5} m/s. The finite element mesh of the numerical model is shown in Figure 1(b). The soil is modelled using quadrilateral displacement-pressure coupled elements termed as SSPquadUP elements [4]. The Hostun sand has been assigned the PM4Sand material model, while the Duxseal layers are assumed to be elastic and isotropic, with Young's modulus of 800 kPa, mass density of 1.65 Mg/m^3, and Poisson's ratio of 0.46. A minimum element size of 0.5 m is adopted, resulting in a total of 1722 continuum elements.

Four continuum elements constitute the foundations of the building, as shown in Figure 1(b). They are assigned the stiffness and mass properties of aluminium. The two columns and the roof of the building are modelled by beam elements. A total of 54 beam elements are also used for modelling the lining of the tunnel. At the soil-lining interface, the nodal displacements of the beam elements are assumed to be equal to those of the corresponding sand elements.

The entire model is subjected to vertical constraints on the bottom edge CD, and free drainage is defined on the upper edge AB. The accelerogram recorded at the base of the rigid container in the test is provided as input at the three encasing boundaries of the numerical model, namely AC, BD, and CD.

A partial comparison between the numerical results and the centrifuge test data is presented in Figure 2. It can be seen that they are in excellent agreement. Thus, the numerical model is validated against the centrifuge test data and could be used to further investigate the essential features of the seismic structure-soil-structure interaction in liquefiable ground.

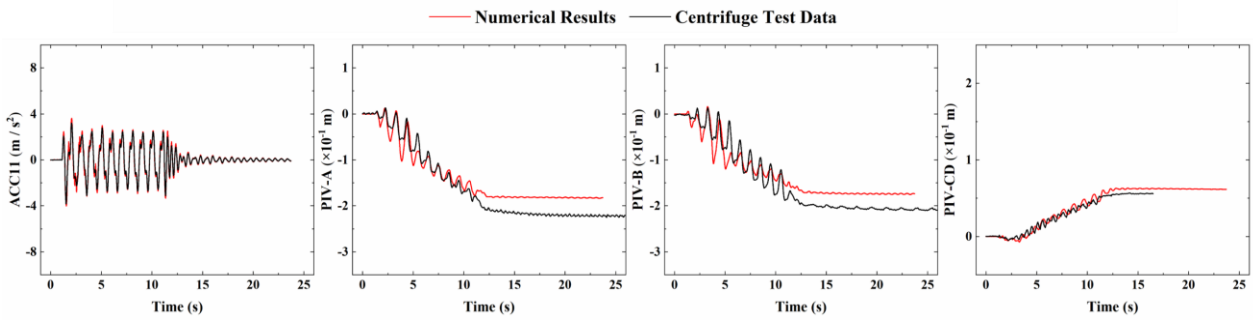

Figure 2. Comparison between the numerical results and the centrifuge test data.

4. References

[1] Pacific Earthquake Engineering Research Center (2021) *User Documentation*. https://opensees.berkeley.edu/

[2] Miranda, G. (2019) *Soil-tunnel-building interaction in a soil susceptible to liquefaction*. University of Naples Federico II, Italy. (in Italian)

[3] Boulanger, R. W. & Ziotopoulou, K. (2017) *PM4Sand (Version 3.1): A sand plasticity model for earthquake engineering applications*, University of California, California.

[4] McGann, C. R., Arduino, P. and Mackenzie-Helnwein, P. (2012) *Stabilized single-point 4-node quadrilateral element for dynamic analysis of fluid saturated porous media*, Acta Geotechnica 7, 297-311.

AUTOMATIC DISCONTINUITY EXTRACTION BASED ON 3D MODEL OF TUNNEL FACE

H.S. Shin[1,2] and C. Pham[1,2]
[1] University of Science and Technology, South Korea
[2] Korea Institute of Civil Engineering and Building Technology, South Korea

1. Introduction

Tunnel face mapping involves the determination of rock discontinuities or weak rock conditions where extra support might be required. In this study, we propose a new technique to automatically quantify the discontinuities of the rock mass based on the 3D tunnel face reconstructed by Lidar scanning and photogrammetry. The general idea is to identify the discontinuities in the 3D model of the tunnel face through the segmentation of its projected 2D images. The segmentation results are then re-projected back to the 3D model based on the depth map and projection matrices resulting in the model accurately reflecting the location and extent of the discontinuities in 3D space. This approach has the potential to solve the problem of traditional methods, which rely solely on normal vector and unsupervised machine learning algorithms to cluster the points in the 3D model into different discontinuity sets.

2. Methodology

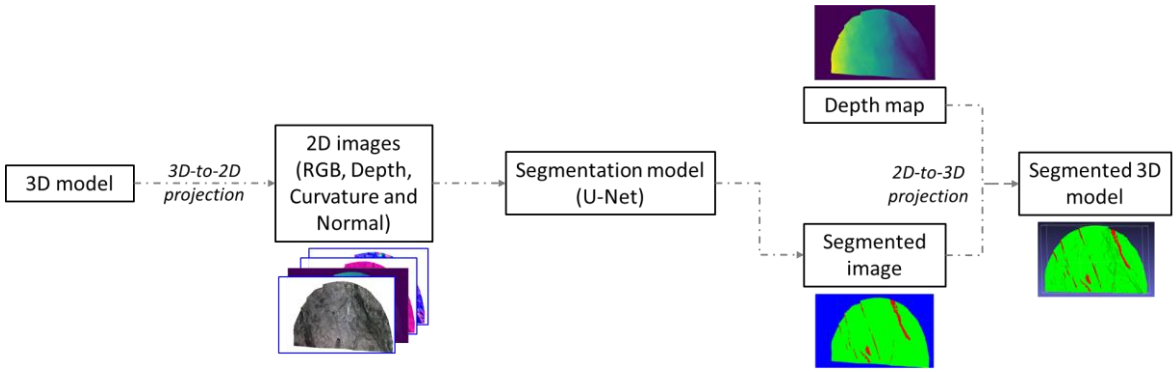

Fig 1. The general process for discontinuity extraction.

The proposed method entails creating a detailed model of the tunnel face using 3D modeling techniques such as Lidar scanning or photogrammetry. This model is then projected onto 2D images, which are segmented to identify areas of discontinuity (Fig. 1). In general, there are three major steps. Firstly, we generate 4 different types of images based on the 3D model: texture color (RGB) image, depth map image, and geometric features color-coded images i.e., local curvatures and normal vectors, since the curvatures and normal vectors are two common parameters used to define a discontinuity plane. To cover the entire tunnel face, we chose to project the 3D model onto three image planes in three different directions with respect to the 3D tunnel face [1]. Secondly, we perform pixel-wise segmentation on each directional group of 2D images using a fully convolutional network called U-Net [2]. The four images of each group are concatenated before being fed to the network. The output of the network is a segmentation mask image of the same size as the input image with discontinuity colored in red (Fig. 2). Finally, the segmented image is re-projected onto the 3D space based on the depth map and projection matrix of each group. The process of re-projecting the 2D segmented image back onto the 3D model is to update the 3D model of the tunnel face accurately reflecting the three-dimensional nature of the rock discontinuities that were identified during the segmentation process.

3. Result and discussion

We tested the automated discontinuity extraction method on a 3D tunnel face that was not used to train the convolutional network. The results show that our proposed method can effectively identify the discontinuity with an average intersection-over-union (IoU) rate of segmentation result of 80%. After re-projecting the segmented result into 3D space, the result shows that there are three density maxima on the stereonet representing three different discontinuity sets, which is comparable to the result of manual mapping (Fig. 3). When compared to the original stereonet, the stereonet obtained using our method shows a clear separation of different discontinuity sets. Despite the segmentation accuracy (i.e., IoU) still being limited due to a lack of training data, it is possible to improve the segmentation model performance to more accurately and completely identify the locations and extents of the rock discontinuities in the tunnel face as the training data grows. Also, our method, as a supervised machine learning approach, has the potential to outperform traditional methods by providing a more reliable and efficient way to identify rock discontinuities. Besides, this study also shows that the 3D models of tunnel faces generated by photogrammetry and Lidar enable accurate and automatic discontinuity measurement, overcoming the limitations of manual mapping while also ensuring time constraints and operator safety for tunnel face mapping tasks [3].

(a) (b)

Fig. 2. An example of segmentation result (b) in comparison with its corresponding ground truth (a)

(a) (b)

Fig. 3. Comparison between original stereonet (a) and stereonet obtained from our approach (b).

3. References

[1] Boulch, A., Guerry, J., Le Saux, B. and Audebert, N. (2018). SnapNet: 3D point cloud semantic labeling with 2D deep segmentation networks. *Comput. Graph.* 71 (Apr): 189–198. https://doi.org/10.1016/j.cag.2017.11.010.

[2] Ronneberger, O., Fischer, P. & Brox, T. (2015). U-Net: Convolutional Networks for Biomedical Image Segmentation. *MICCAI, Springer, LNCS*. 9351:234-241.

[3] Pham, C., Shin, H. S. (2022). 3D Tunnel Face Modelling for Discontinuities Characterization: A Comparison of Lidar and Photogrammetry Methods. *Tunnel and Underground Space*, 32(6), 549-557. doi:10.7474/TUS.2022.32.6.549.

LIMIT ANALYSIS MODELING OF MASONRY ARCH BRIDGE WITH POLYGON DISCRETIZATION FOR BACKFILL

Y. Hua and G. Milani
Politecnico di Milano, Piazza Leonardo da Vinci 32, 20133 Milan, Italy

1. Introduction

In recent numerical works, backfill was usually ignored when analyzing the collapse of masonry arch bridges. However, it has been experimentally proven that its presence has a positive effect on the collapse load [1]. This paper presents a limit analysis modeling of masonry arch bridges with full consideration of the backfill. Here, bricks are regarded as rigid blocks and the backfill region is discretized into deformable Voronoi cells. The formulation is established based on Upper Bound (UB) theorem. The question of how to employ the deformable polygon elements in limit analysis still remains open because a careful design of the velocity shape function is required. In this paper, we first propose a constant-strain polygon element for limit analysis, which could be an alternative.

2. Methodology

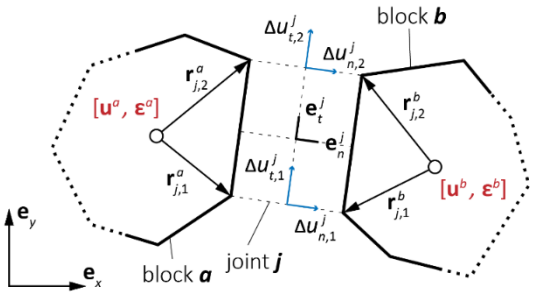

Figure 1. joint *j* with two adjacent blocks *a* and *b*: calculation of velocity discontinuities.

Let us consider a joint *j* with two adjacent blocks *a* and *b* (Figure 1). Incorporating the constant-strain assumption, the velocity field in the polygon can be explicitly derived from velocity and strain components at the centroid of the element (Eq. (1)). Then, we can calculate the velocity discontinuities $\mathbf{q}_j$ based on these centroid variables ($\mathbf{u}^i$ and $\dot{\boldsymbol{\varepsilon}}^i$, $i = a, b$). The matrix form of this relation is given in Eq. (2), where $\mathbf{A}^i_{j,u}$ and $\mathbf{A}^i_{j,\varepsilon}$ completely depend on the geometry of the blocks.

$$\mathbf{u}^i(x,y) = \left[\dot{\varepsilon}^i_x x + \left(\dot{\gamma}^i_{xy} - \omega^i\right) y + u^i_x \quad \dot{\varepsilon}^i_y y + \left(\dot{\gamma}^i_{xy} + \omega^i\right) x + u^i_y\right] \tag{1}$$

$$\mathbf{q}_j = \begin{bmatrix} -\left(\mathbf{A}^a_{j,u}\right)^T & \left(\mathbf{A}^b_{j,u}\right)^T \end{bmatrix} \begin{bmatrix} \mathbf{u}^a \\ \mathbf{u}^b \end{bmatrix} + \begin{bmatrix} -\left(\mathbf{A}^a_{j,\varepsilon}\right)^T & \left(\mathbf{A}^b_{j,\varepsilon}\right)^T \end{bmatrix} \begin{bmatrix} \boldsymbol{\varepsilon}^a \\ \boldsymbol{\varepsilon}^b \end{bmatrix} \tag{2}$$

Based on the UB approach, an optimization problem can be written in the form of Eq. (3). Compared with the formulation of rigid block limit analysis (see [2]), a term $\mathbf{A}^T_\varepsilon \dot{\boldsymbol{\varepsilon}}$, which accounts for the deformability of the elements, is added to the compatibility condition. Besides the flow rule for $\mathbf{q}$, an extra condition for $\dot{\boldsymbol{\varepsilon}}$ (the third constraint in Eq. (3)) is added based on the Mohr-Coulomb criterion [3]. The dissipation power in the element $\mathbf{c}^T_1 \dot{\boldsymbol{\lambda}}$ is also accounted for in the objective function.

$$\begin{aligned} &\text{minimize} \quad -\mathbf{f}^T_D \mathbf{u} + \mathbf{c}^T_0 \mathbf{p} + \mathbf{c}^T_1 \dot{\boldsymbol{\lambda}} \\ &\text{subject to} \quad \mathbf{f}^T_L \mathbf{u} = 1,\ \mathbf{A}^T_u \mathbf{u} + \mathbf{A}^T_\varepsilon \dot{\boldsymbol{\varepsilon}} = \mathbf{q}, \mathbf{M}^T \dot{\boldsymbol{\lambda}} = \dot{\boldsymbol{\varepsilon}}, \dot{\boldsymbol{\lambda}} \geq 0,\ \mathbf{N}^T \mathbf{p} = \mathbf{q}, \mathbf{p} \geq 0 \end{aligned} \tag{3}$$

3. Results

As an implementation of the proposed theory, we present here a 2D collapse analysis of "Prestwood Bridge". More information on the geometry of the bridge can be found in ref. [4]. The load is a 0.3m-width pressure applied at ¼ span (Figure 2). The frictional angle for all the joints and elements is 37°; the density of both the backfill and brick is 20 kN/m^3; the cohesion for the backfill is 0.01MPa. All these parameters are in line with the collapse analysis presented in the literature [4].

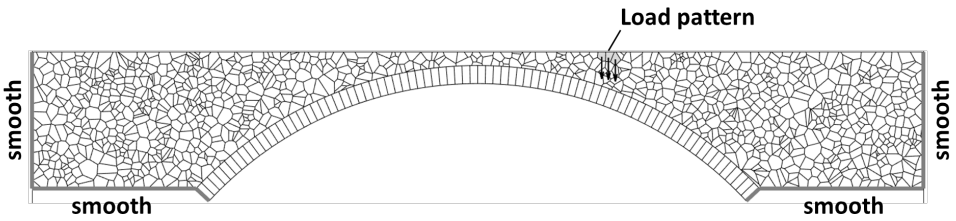

Figure 2. geometry, loading case, and boundary condition

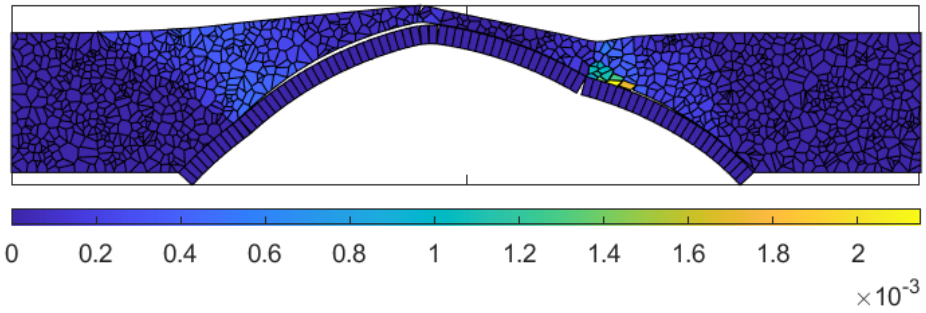

Figure 3. collapse mechanism and distribution of plastic strain, P_u = 341.33 kN

As shown in Figure 3, the predicted collapse mechanism for the arch ring is very close to a standard 4-hinge mechanism. The backfill region is separated into parts. The left part moves upward along with the arch ring and the elements near the loading point are compressed and move downwards. The backfill elements that contact the arch ring below the external pressure experience a large deformation. Here, we also note a dispersion of the load within the backfill region. The width of the pressure transferred onto the arch is larger than the original load at the surface. A region of large strain is located on the left side of the backfill as well. This should be attributed to the passive extrusion due to the movement of the arch ring. Finally, although the collapse mechanism and strain distribution are similar to the results reported in [4], the predicted collapse load is still higher than the experimental results [5]. Calibration of the material parameters and more parametric studies will be carried out in our future work.

4. References

[1] Royles R, Hendry AW (1991). Model tests on masonry arches. *Proc - Inst Civ Eng Part 2 Res theory*, **91**, 299–321

[2] Ferris MC, Tin-Loi F (2001). Limit analysis of frictional block assemblies as a mathematical program with complementarity constraints. *Int J Mech Sci*, **43**, 209–224.

[3] Bottero A, Negre R, Pastor J, Turgeman S (1980). Finite element method and limit analysis theory for soil mechanics problems. *Comput Methods Appl Mech Eng*, **22**, 131–149.

[4] Cavicchi A, Gambarotta L (2005). Collapse analysis of masonry bridges taking into account arch-fill interaction. *Eng Struct*, **27**, 605–615.

[5] Page J (1987). Load Tests To Collapse on Two Arch Bridges At Preston, Shropshire and Prestwood, Staffordshire. Res Rep - Transp Road Res Lab.